University of Venda
Creating Future Leaders

UNDERSTANDING THE PROPERTIES OF THE INTERFACE BETWEEN GRAPHENE AND TRANSITION METAL OXIDE THIN FILMS USING FIRST PRINCIPLE APPROACHES

Lutendo Phuthu
11593291
Department of Physics
University of the Venda

A thesis submitted in partial fulfillment for the degree of

Doctor of Philosophy

2024

Declaration

I declare that "Understanding the properties of the interface between graphene and transition metal oxides thin films using first principle approaches"is my work, that it has not been submitted for any degree or examination in any other university, and that all sources I have used or quoted have been indicated and acknowledged by complete references.

Lutendo Phuthu February 2024

Signature: 

Dedicated to my loving sisters Marcia, Neani and Ronewa

To my late parents, may their souls rest in peace.

Acknowledgements

My graduate experience was greatly enhanced by the expertise, understanding, and patience of my supervisor, Eric Maluta. I would like to take this opportunity to express my sincere appreciation and thanks to him. I respect the breadth and depth of his expertise across a variety of fields. I highly doubt that I will ever be able to adequately express how grateful I am to him, but I owe him my undying gratitude.

My co-supervisor Rapela Maphanga from the Council for Scientific and Industrial Research (CSIR) deserves an extra-special thank you for all of her hard work. She guided me in the right direction and offered me assistance with the technical aspects. The result of her unwavering dedication to assisting was the successful completion of the work.

I would like to express my appreciation to the University of Venda's Department of Physics for all the assistance they have given me in times of need.

During the course of my doctoral studies, I was assisted by a number of people at the University of Venda, including the material science modeling group, Thokozani Mlotswha, Tshifhiwa Ranwaha, Nditsheni Nekhwevha, Ronel Randela, Vusi Mabaso, and especially Ratshilumela Dima, who provided me with insightful suggestions and words of advice. In conclusion, I would like to express my gratitude to AMSCOR and NITheCS for their provision of financial support throughout this period.

Abstract

Recently, carbonaceous nanomaterials such as carbon nanotubes and two-dimensional graphene have attracted the attention of the scientific community in probes to improve energy conversion and storage technologies. The graphene sheet is preferred due to its large specific area, flexible structure, high transparency, excellent mobility of charge carriers and is expected to be able to slow the charge recombination. Graphene/transition metal oxides nanocomposite study has become much of a wide interest recently with metal oxides like TiO_2, ZnO, SnO_2, etc. These metal oxides are used as thin films in photovoltaic technology to harness energy. The final composite embodies both the transport properties of the former and the semiconducting properties of the latter species. This work describes an analysis of the electronic and optical properties of the final composite studied using the Density Functional Theory (DFT) in application to dye-sensitized solar cells (DSSCs). The study aims to slow charge recombination in DSSCs and improve the efficiency of the cell. The geometry optimizations for the electronic and optical properties were performed by the first principle calculations based on density functional theory. Various supercells of graphene were modelled and, optimized and their properties were calculated. The results show that different graphene supercells have different electronic and optical properties. When graphene is incorporated into a brookite TiO_2, the composite results show a reduced energy band gap compared to that of a brookite TiO_2 without a graphene on it. The optical properties showed graphene/TiO_2 increases absorption in the infrared region.

Abbreviation

LEDS	Light emitting diodes
DSSC	Dye-sensitized solar cell
CO_2	Carbon dioxide
TiO_2	Titanium dioxide
ZnO	Zinc oxide
SnO_2	Tin oxide
0D	Zero-dimensional
1D	One-dimensional
2D	Two-dimensional
3D	Three-dimensional
CNTs	Carbon nanotubes
TCO	Transparent conducting oxide
I^-	Iodide
I_3^-	Tri-iodide
FF	Cell's efficiency
I_{max}	Current
V_{max}	Voltage
J_{sc}	Short-circuit current density
V_{oc}	Open-circuit voltage
P_{in}	Incident light power
eV	Electron Volt
UV	ultraviolet
SCR	Selective catalytic reduction
CB	Conduction band
VB	Valence band
BZ	Brillouin zone
LiS	Lithium sulfer
EEDs	electron emission displays
GO	graphene oxide
FTO	Fluorine-doped tin oxide
wt	weight

NSs	Nanosheets
HF	Hartree-Fork
HK	Hohenburg-Kohn
KS	Kohn-Sham
LDA	Local density approximation
GGA	Generalized gradient approximation
PBE	Perbew-Burke-Ernzerhof
CASTEP	Cambridge Serial Total Energy Package
IR	Infrared
LCD	Liquid crystal display
OLEDs	Organic light emitting diodes
N	Nitrogen
B	Boron
Be	Beryllium

Contents

List of Figures

List of Tables

Chapter 1

Introduction

1.1 Background

The energy provided by the sun is essential for the survival of all living things. We put this energy to use in the form of electricity and liquid fuels, and its contribution to human socialism, human welfare, and health, as well as sustainability and economic growth, are all made possible by these forms of energy. Since the dawn of human history, people have been making use of energy in various forms; one such form is illustrated by the energy derived from firewood. In order for humans to fulfill their daily requirements, they require energy [1]. The energy that originates from fossil fuels, which are essentially a stored form of solar energy, is by far the most common and widely used source of energy worldwide. In addition to these, we also have access to another category of energy that is referred to as renewable energy (wind, biomass, solar, tidal, geothermal, hydroelectric, hydrogen and fuel cells). Figure 1.1 depicts the total energy resources by South Africa as of the year 2018. It is anticipated that by the year 2050, the global demand for energy will have increased by a factor of two as a consequence of the growth in the population of the world economic development as a whole as well as the improvement in the standard of living of people in developing nations [2]. In recent years, the unwavering reliance on fossil fuels has emerged as a major cause for concern due to the proliferation of problems such as climate change and the emission of carbon dioxide (CO_2). Because we continue to rely on

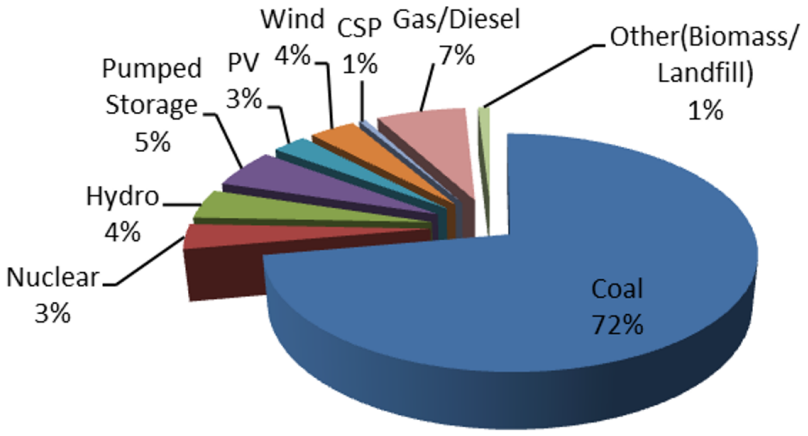

Figure 1.1: South African total energy resources in 2018 [3].

fossil fuels, experts believe that we will only have access to these resources for the next hundred years at the very most [4]. As a result of these concerns, researchers have begun investigating or searching for alternative sources of energy that are less harmful to the environment and can be used in place of fossil fuels. It is anticipated that this particular source of energy should be able to keep the human race alive for the next billion years. As a result of the fact that it does not cause any CO_2 to be released into the air, nuclear energy is considered to be one of the solutions to the problem of finding clean energy sources. However, due to the fact that the elements used in nuclear energy are themselves radioactive, there are concerns about the radioactive waste and the security of the nuclear power plants [5]. Dependence on nuclear energy is associated with a number of other concerns, one of which is the worry that accidents will occur at nuclear power plants, which can be catastrophic.

Recently, a significant number of researchers have been focusing their efforts on developing methods to extract energy from the sun and transform it into forms that are applicable to human needs [6]. These include solar fuels, solar thermal energy, and photovoltaic and thermal forms of solar electricity. To collect the sun's rays and convert them into usable energy, scientists have

developed a number of different technologies (opto-electronic devices). The relationship between light and matter serves as the conceptual foundation for the technology that underpins opto-electronic devices. Semiconductor material is traditionally used in the construction of opto-electronic devices. In these types of devices, either light is changed into electrical signals (as is the case with solar cells) or electrical signals are changed into light (as is the case with light-emitting diodes, or LEDs). Electrons are released from a metal when light strikes it in a certain way, and this causes the light to cause the material to change. If one thinks about this process as taking place inside of a circuit, the electrons that are ejected will be the source of current inside of the circuit. As an example, a photovoltaic device is illustrated by the use of a solar cell as an example (where photons are converted into electricity).

There have been four distinct generations of solar cells that were developed over the years. Crystalline silicon solar cells and semiconductor thin-film solar cells are the conventional first and second generations of solar cells, and they currently hold the majority of the market share, with conversion efficiencies of up to 30% and 20%, respectively [7]. The organic class is considered the third generation, while the hybrid category is considered the fourth generation. The four generations as well as their respective classifications are shown in Figure 1.2. Within the third generation class of solar cells, the dye-sensitized solar cells (DSSCs) are one of the most promising solar cells due to the low cost of materials and manufacturing as well as their high photon-to-energy transfer efficiency [8]. Despite the benefits of DSSCs that were discussed above, their efficiency is still quite low, hovering somewhere around 15% [9, 10].

Thin films of transition metal oxides, such as TiO_2, ZnO, and SnO_2, are typically utilised as semiconductors in DSSCs due to the fact that they are non-toxic and have a lower propensity for corroding when exposed to illumination. Experimental and computational studies have shown that these semiconductors are good materials for the application of solar cells and photocatalytics [11]. On the other hand, because of the wide band gap, these

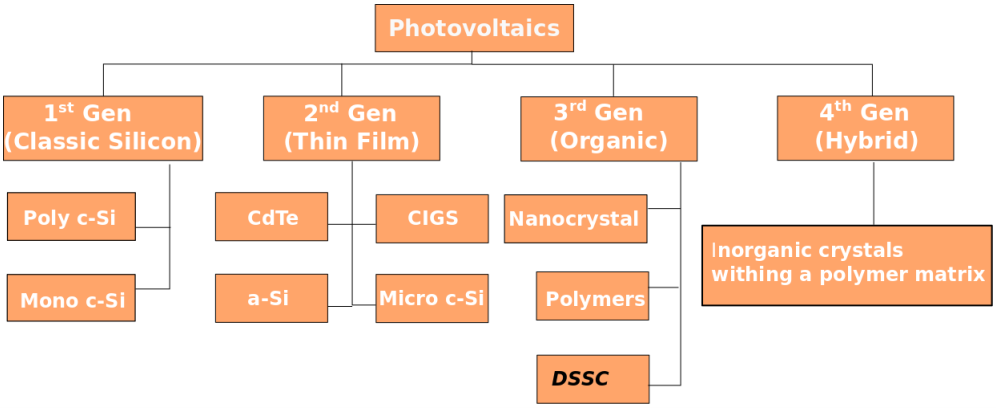

Figure 1.2: Classification of solar cells.

semiconductors only have a limited amount of absorption edges in the visible region. The rutile, anatase, and brookite polymorphs of titanium dioxide are the ones that are most frequently encountered [12–15]. The crystal structure of ZnO is known as Wurzite [16], whereas the structure of SnO_2 is known as rutile tetragonal [17]. In applications involving photocatalysis, charge recombination is caused by the wide band gaps of the metal oxides that have been mentioned. The charge recombination is a primary detriment that inhibits the performance of DSSCs. More specifically, the back-electron transfer that occurs in the semiconductor photoanode-electrolyte interface just before it reaches the collective electrode is considered to be the primary recombination pathway, which lowers the efficiency of DSSCs [18]. It is hypothesized that enhancing the conduction from the location of the photo-generated carriers to the collecting electrode would result in a significant increase in the DSSC's overall efficiency [19]. There are a few different approaches that are taken in order to both reduce the likelihood of recombination and increase the efficiency of transport [19] namely;

1. Insertion of foreign elements in the semiconductor photoanode
2. Hybridisation of a semiconductor photoanode with another materials of different bandgaps
3. Inducing charge carriers to direct the photogenerated electron.

Doping with transition metals (like chromium and silver) and non-metals (like nitrogen and sulphur) facilitated charge transfer and led to an increase in the DSSCs' overall efficiency [20–24]. Recent research has focused on loading one-dimensional (1D) and two-dimensional (2D) nanomaterials, such as carbon nanotubes (CNT) and graphene sheet, onto metal oxides in an effort to improve the DSSCs photoelectric conversion efficiency. Despite this, the CNT has only brought about a marginal improvement in DSSCs efficiency [25].

In this study, the interface of graphene with transition metal oxides is investigated using a method that involves computer simulation. It is intended to investigate the properties of the interface between graphene and TiO_2. Both the interaction of graphene with the metal oxide and the structure of the final composite will be the subject of this research. According to a number of studies, the photocatalytic efficiency of nanoparticles is significantly higher when compared to that of the bulk structure of particles. The surface of TiO_2 is utilized in this study rather than its bulk counterpart.

1.2 Problem statement

Thin films of transition metals such as TiO_2, ZnO, and SnO_2 are typically used as semiconductors in DSSCs due to their lower susceptibility to corrosion when exposed to illumination and also due to the fact that they are non-toxic. The primary limitation of these metal oxides, however, is that they have wide band gaps (ranging from 3.0 to 3.7 eV), which causes them to absorb only the ultraviolet portion of the solar spectrum. The effectiveness of the DSSCs is dependent on the minimization of the possible recombination pathways that occur at the interfaces between the semiconductor, the oxidized state of the dye, and the electrolyte. This is because the effect of charge recombination between electrons and the oxidized state of the dye impedes the transportation of electrons and reduces the efficiency of the photoelectric conversion. The hybridization of the metal oxide with other materials whose

band gaps are different is one strategy for reducing the number of recombination pathways. This work sought to gain a deeper comprehension of the interactions that take place in the hybridized semiconductor in order to limit the charge recombination and enhance the electron transport capabilities of DSSCs.

Aim

To investigate the interaction of graphene with TiO_2 brookite surface to enhance the photoelectric efficiency in the dye-sensitized solar cells using computational model based on DFT.

Outline of the thesis

There are six chapters that make up this thesis.

1. The first chapter is an introduction that includes some background information, problem statement and the purpose of the study.

2. The literature review is presented in Chapter 2, and it is broken up into three main sections. The description of DSSCs is the first topic covered in the first section. It provides additional insights regarding the various phase structures of TiO_2. In the second section, information is presented regarding graphene, and in the third section, the graphene/TiO_2 composite is discussed.

3. The computational methods are discussed in chapter three, with the density functional theory serving as the primary point of emphasis. Also, the computational software: Biovia Material Studio and Cambridge Sequential Total Energy Package (CASTEP), are discussed in chapter three.

4. Both chapter four and chapter five go into detail regarding the theoretical calculations and the results that correspond to them.

5. The last chapter, chapter 6, gives a conclusion of the entire study.

Bibliography

[1] O. Edenhofer, R. Madruga, Y. Sokona, K. Seyboth, P. Matschoss, S. Kadner, T. Zwickel, P. Eickemeier, G. Hansen, S. Schlmer and C. Von Stechow, Summary for Policymakers: In IPCC Special Report on Renewable Energy Sources and Climate Change Mitigation, Cambridge University Press,2011.

[2] OECD, Energy and Climate Policies and Innovation OECD Publishing (forthcoming), 2012.

[3] http://www.energy.gov.za/IRP/irp-update-draft-report2018/IRP-Update-2018-Draft-for-Comments.pdf

[4] A. J. Friedemann, Life after fossil fuels: A reality check on alternative energy, Springer International Publishing,London, UK, 2021.

[5] T. V. Beken, N. Dorn and S. V. Daele, Security risks in nuclear waste management: Exceptionalism, opaqueness and vulnerability, Journal of Environmental Management, 91, 940, 2010.

[6] T. J. Abodunrin, O. Obafemi, A. O. Boyo, T. Adebayo and R. Jimoh, The effect of electrolyte on dye sensitized solar cells using natural dye from Mango (M. indica L.) leaf as sensitizer, Advances in Materials Physics and Chemistry, 5, 205, 2015.

[7] Q. Zhang and G. Cao. Nanostructured photoelectrodes for dye-sensitized solar cells, Nano Today, 6(1), 91-109, 2011

[8] G. Hashmi, K. Miettunen, T. Peltola, J. Halme, I. Asghar, K. Aitola, M. Toivola and P. Lund, Review of materials and manufacturing options for large area flexible dye solar cells, Renewable and Sustainable Energy Reviews, 15, 3717, 2011.

[9] A. Yella, H. Lee, H.N. Tsao, C. Yi, A.K. Chandiran, M.K. Nazeeruddin, E.W. Diau, C. Yeh, S.M. Zakeeruddin and M. Grtzel, Porphyrin-Sensitized solar cells with cobalt (II/III)-based redox electrolyte exceed 12 percent efficiency, Science, 334, 629, 2011.

[10] D. ORegan and M. Gratzel, A low-cost, high-efficiency solar cell based on dye-sensitized colloidal TiO_2 films, Nature, 353, 737, 1991.

[11] C. Cavallo, D. Di Pascasio, A. Latini, M. Bonomo and D. Dini, Nanostructured semiconductor materials for dye-sensitized solar cells, Journal of Nanomaterials, 2017, 1, 2017.

[12] R. Asahi, Y. Taga, W. Mannstadt and A. J. Freeman, Electronics and optical properties of anatase TiO_2, Physical Review B, 61, 7459, 2000.

[13] J. Zhang, P. Zhou, J. Liu and J. Yu, New understanding of the difference of photocatalytic activity among anatase, rutile and brookite TiO_2, Physical Chemistry Chemical Physics, 16, 20382, 2014.

[14] K. Li, J. Xu, W. Shi, Y. Wang and T.Peng, Synthesis of size controllable and thermally stable rice-like brookite titania and its application as a scattering layer for nano-sized titania film-based dye-sensitized solar cells, Journal of Materials Chemistry A, 2, 1886, 2014.

[15] A. Mattsson and L sterlund, Adsorption and photoinduced decomposition of acetone and acetic acid on anatase, brookite, and rutile TiO_2 nanoparticles, Journal of Physical Chemistry C. 114, 14121, 2010.

[16] D. C. Look, Recent advances in ZnO materials and devices, Materials Sciences Engineering: B, 80(1), 383, 2001.

[17] J.C. Manifacier, M. De Murcia, J.P. Fillard and E. Vicario, Optical and electrical properties of SnO_2 thin films in relation to their stoichiometric deviation and their crystalline structure, Thin Solid Films, 41, 127, 1977.

[18] A. Subramanian, C. Y. Ho and H. Wang, Investigation of various photoanode structures on dye-sensitized solar cell performance using mixed-phase TiO_2, Journal of Alloys and Compounds, 572, 11, 2013.

[19] A. Eshaghi and A. A. Aghaei, Effect of TiO_2-graphene nanocomposite photoanode on dye-sensitized solar cell performance, Bulletin of Materials Science, 38 (5), 1177, 2015.

[20] Y. H. Peng, G. F. Huang and W. Q. Huang, Visible-light absorption and photocatalytic activity of Cr-doped TiO_2 nanocrystal films, Advanced Powder Technology, 23, 8, 2012.

[21] Y. Liu, C. Liu, Q. Rong and Z. Zhang, Characteristics of the silver-doped TiO_2 nanoparticles, Applied Surface Science, 220, 7, 2003.

[22] R. Asahi, T. Morikawa, T. Ohwaki, K. Aoki and Y. Taga, Visible-light photocatalysis in nitrogen-doped titanium oxides, Science, 293, 269, 2001.

[23] T. Umebayashi, T. Yamaki, H. Itoh and K. Asai, Band gap narrowing of titanium dioxide by sulfur doping, Applied Physics Letters, 81, 458, 2002.

[24] T. Umebayashi, T. Yamaki, S. Tanaka and K. Asai, Sulfur-doping of rutile-titanium dioxide by ion implantation: Photocurrent spectroscopy and first-principles band calculation studies, Journal of Applied Physics, 93, 5156, 2003.

[25] C. P. Lee, C. T. Li and K. C. Ho, Use of organic materials in dye-sensitized solar cells, Materials Today, 20 (5), 267, 2017.

Chapter 2

Graphene and metal oxides

2.1 Dye-sensitized solar cells

In earlier research on semiconductors used in DSSCs, the emphasis was placed on the flat electrodes [1, 2]. In those studies, only the first monolayer of absorbed dye led to effective electron injection in the semiconductor. However, the amount of light that could be harvested from a single monolayer of dye was extremely low; this was one of the most significant challenges. By using a mesoporous TiO_2 with a high surface area, ORegan and Gratzel were able to increase the efficiency of DSSCs by an order of magnitude in the year 1991 [3]. Since then, the amount of research conducted across the continuum of DSSCs has grown at a rapid pace (see Figure 2.1).

The DSSCs are made up of five primary parts. Figure 2.2 illustrates the fundamental parts of the DSSCs in (a) and the working mechanism of the DSSCs in (b), which are as follows:

1. A transparent conducting oxide (TCO) coated on a glass.
2. A mesoporous oxide layer (typically TiO_2) deposited on the anode to activate electronic conduction.
3. A monolayer of dye bonded on the surface of mesoporous oxide layer to enhance light absorption.
4. Redox-active liquid electrolyte usually the iodide/tri-iodide couple (I^-/I_3^-)

5. Platinum counter electrode.

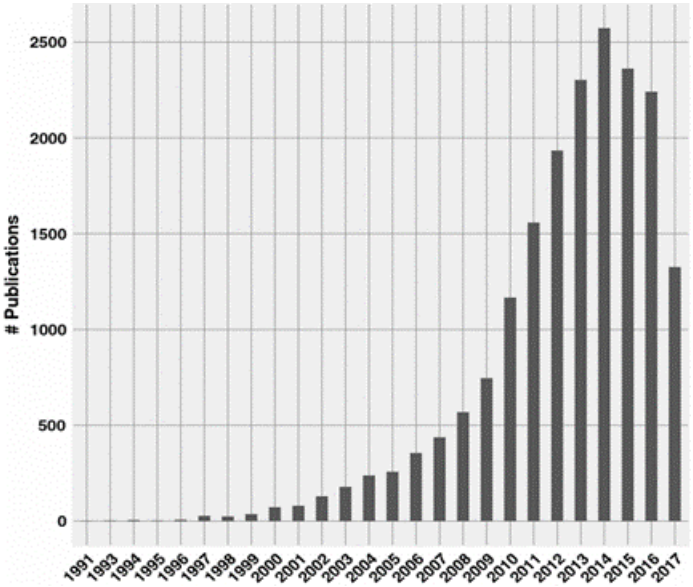

Figure 2.1: Literature growth of dye sensitized solar cells research.

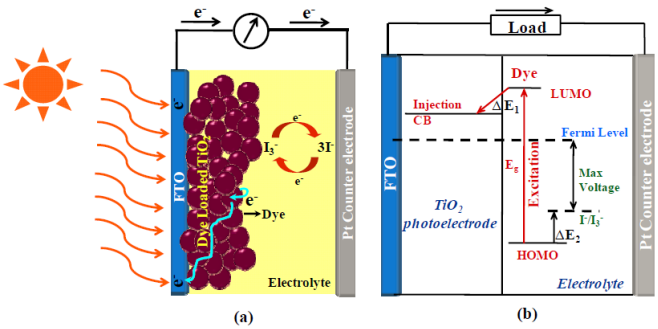

Figure 2.2: Schematic view of DSSCs and its working mechanism.

When the DSSC is exposed to light, the dye sensitizer will take in a photon from the sun, which will then cause it to become excited. In response to

the photoexcitation of the dye, an ejected electron will enter the conduction band of the semiconductor. After the electron has been injected into the semiconductor, it has the opportunity to recombine either with the oxidized dye or with the I_3^- in the electrolyte. This mechanism of electron transfer results in a loss of efficiency, and recombination at the interfaces between the semiconductor and the dye as well as between the semiconductor and the electrolyte must be reduced as much as possible. The electrons, having passed through the nanostructure and arrived at the anode, then proceed to the external load, where they produce some work before being collected at the cathode. The oxidized dye is returned to its ground state by the electrolyte, and I_3^- is reduced to I^- by the electrons at the cathode. The overall performance of a solar cell can be measured in terms of the cell's efficiency (represented by the symbol η) and its fill factor (represented by the symbol FF) [4],

$$FF = \frac{I_{max}V_{max}}{J_{sc}V_{oc}} \tag{2.1}$$

and

$$\eta = \frac{J_{sc}V_{oc}}{P_{in}} \ , \tag{2.2}$$

where I_{max} and V_{max} correspond to current and voltage, respectively, at which the maximum power output is derivable. J_{sc} is the short-circuit current density in mA/cm^2, V_{oc} is the open-circuit voltage (V) and P_{in} is the incident light power.

The semiconductor, one of the five primary components that make up DSSCs, is an essential component in the process of optimising DSSCs since it affects dye molecules' anchoring, charge carrier transfer, and separation [5]. This makes it to have a crucial role in optimising the DSSCs. TiO_2, ZnO, and SnO_2 are the three types of semiconductors that are most frequently used in DSSCs. These semiconductors have been shown to be effective materials for use in solar cells and photocatalytic applications by both experimental and computational research [6]. However, due to the wide band gaps that exist in these semiconductors, the visible absorption edges that they possess are quite limited.

2.1.1 Titanium dioxide

Titanium dioxide can be represented as the chemical formula TiO_2. Although TiO_2 exists in a number of different polymorphs, the most common ones are rutile, anatase, and brookite. Each of these polymorphs has a distinct crystal structure and a unique set of physical properties [7]. The three different crystal structures of rutile, anatase, and brookite are compared in Figures 2.3 to 2.5. Rutile and brookite display corner- and edge-sharing of TiO_6 units, whereas anatase is constructed by sharing the edges of TiO_6 units in all three directions [7]. Table 2.1 contains a listing of the crystallographic data and important physical properties of rutile, anatase, and brookite.

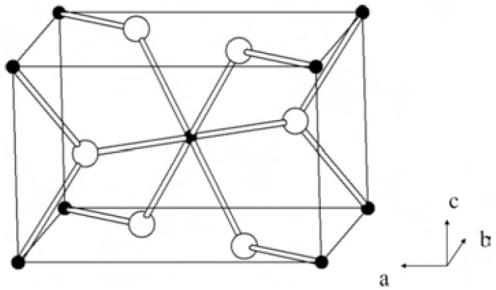

Figure 2.3: Elementary cell of rutile. Atoms represented according to circle symbol: Ti in black circle and O in white circle.

Unlike the anatase and rutile that have good symmetry, brookite is in low symmetry. Due to oxygen vacancies in TiO_2 lattice and large band gap (E_g>3 eV), TiO_2 is considered as an n-type semiconductor. The band gaps of rutile, anatase and brookite are 3.0 eV, 3.2 eV and 3.4 eV, respectively [8–11]. For particles having a size of above 35 nm, rutile is thermodynamically the most stable phase, while for nanoparticles of size below 10-20 nm, anatase is considered to be the most stable phase thermodynamically.

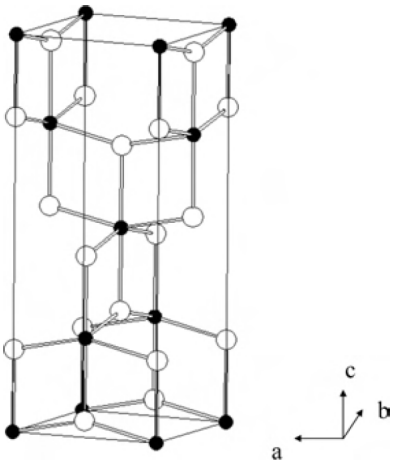

Figure 2.4: Elementary cell of anatase. Atoms represented according to circle symbol: Ti in black circle and O in white circle.

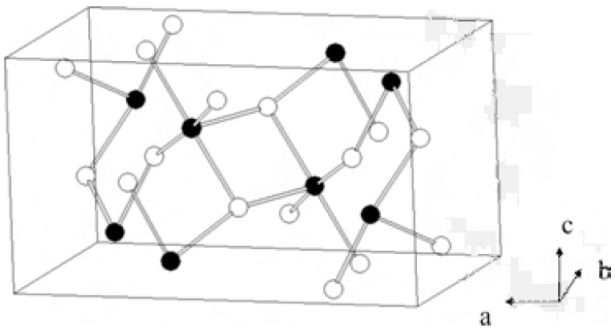

Figure 2.5: Elementary cell of brookite. Atoms represented according to circle symbol: Ti in black circle and O in white circle.

Table 2.1: Crystallographic and physical properties of rutile, anatase and brookite TiO_2 [7].

	Rutile	Anatase	Brookite
Chemical formula	TiO_2	TiO_2	TiO_2
Crystal system	tetragonal	tetragonal	orthorhombic
Point group according to Schonflies	D_{4h}	D_{4h}	D_{4h}
Point group according to Herman-Mauguin	4 mmm	4 mmm	4 mmm
a [nm]	0.4594	0.3785	0.9184
b [nm]	0.4594	0.3785	0.5447
c [nm]	0.2958	0.9514	0.5245
Volume of the elementary cell [nm^3]	62.07	136.25	257.38
Molar volume [cm^3/mol]	18.693	20.156	19.377
Mohs' hardness	6.7-7	5.5-6	5.5-6
Density [g/cm^3]	4.2-4.3	3.8-3.9	3.9-4.1
Melting point [°C]	1830-1850	transformation to rutile	transformation to rutile

The anatase and brookite forms of titanium dioxide have a propensity to transform into the rutile form when subjected to heating in conjunction with coarsening [12–14]. The two phases of TiO_2 known as anatase and rutile are the ones that have garnered the most attention for their potential use in photocatalytic applications [15]. The fact that brookite is typically photocatalytically inert [16, 17] and frequently difficult to synthesize in a reliable manner [18] is a significant drawback for the use of brookite in applications involving photocatalysis. Studies have shown that while rutile has a small band gap, its photocatalyst performance is inferior to that of anatase and brookite [19,20]. The below par light absorption of rutile near the UV region is responsible for the decreased photocatalytic activity of TiO_2 when it is in the rutile phase [15]. In addition to this, the conduction and valence band edges in rutile are not positioned as favourably as they are in anatase [15]. On the other hand, Anatase is the most preferred phase for use in photocatalytic applications [17, 21, 22]. This is because anatase possesses superior

electron mobility, a lower dielectric constant, a lower density, a lower capacity to adsorbed oxygen, and a higher degree of hydroxylation than rutile and brookite [20, 23].

Application of titanium dioxide

Pigment

Titanium dioxide absorbs little visible light, making it a popular white pigment (380-700 nm). Rutile and anatase have high refractive indeces of 2.7 and 2.6, respectively. TiO_2 is a better pigment because its rutile and anatase pigments have better concealing power in coatings and polymers due to their high refractive index values [24]. Titanium dioxide pigment is used to make plastics less clear in applications that involve plastics. TiO_2 needs to mix well with polymers and be stable at elevated temperatures for it to be used in plastics. Even though there are other white pigments in the paper industry, only titanium dioxide can be used to make high-quality papers. High-quality papers get their brightness and opacity from titanium dioxide. The type of TiO_2 can also change how the ink flows, how rough it is, how shiny it is, and how easily it can be mixed back together. TiO_2 is also commonly used as a coloring agent in the pharmaceutical and cosmetics industries [24].

Energy generation and storage

With its unique properties (physical and chemical), nano-structured titanium dioxide has demonstrated a variety of interesting applications in energy generation and storage [25–27]. DSSCs have utilised nanostructured TiO_2 as their primary semiconducting material. In DSSCs, a visible-absorbing electron sensitizer is utilised to inject charge carriers across the semiconductor-electrolyte junction into TiO_2 in order to improve the solar energy conversion efficiency [28–30]. TiO_2 is also utilised in the production of hydrogen in water splitting as a semiconducting material. Due to the smaller particle sizes of TiO_2 nanoparticles, significantly more surface area per mass is accessible

for the absorption of water in the process of water splitting [25]. As an alternative to carbonaceous anodes, titanium dioxide is another viable anode material for use in lithium-ion batteries [31, 32].

Environment protection

The use of nanostructured TiO_2 as a material for antibacterial applications is one use that has been commercially successful [33, 34]. Tiles that contain nano-structured TiO_2 have been utilised to produce a photocatalytic surface. This surface decomposes bacteria and viruses that are already present on the surface, as well as bacteria that are floating in the air when they come into contact with the surface. Utilizing the photocatalytic characteristics of nano structured TiO_2, an additional significant application of this material is found in the water treatment industry. TiO_2 has been employed in the photocatalytic degradation of organic dyes in wastewater, as well as the photocatalytic decomposition of organic pollutants in other contaminated waters, such as pesticides, dyes, and pharmaceuticals.

Catalyst

Composite materials based on TiO_2 have seen significant use in the field of catalysis [35, 36]. In commercial V_2O_5-WO_3/TiO_2 catalysts for the selective catalytic reduction (SCR) of NOx, titanium dioxide is employed as a support material. By utilising SCR technology, extremely harmful NOx acid gas emissions produced by a variety of industrial sources can be converted into non-hazardous N_2 and H_2O. Because of their superior thermal stability and lower oxidation activity, the V_2O_5-WO_3/TiO_2 catalysts find widespread use in commercial applications [37, 38]. This is mostly due to the fact that they catalyze the conversion of SO_2 to SO_3. Since the beginning of the 1970s, when this technology was first introduced, the V_2O_5-WO_3/TiO_2 catalysts have established themselves as the most popular choice among industrial users for use in SCR applications [39].

Health and Biomedicine

TiO_2 is a semiconducting material that possesses an exceedingly high refractive index. Because of the material's high refractive index, it is able to scatter visible light. Sunscreen is a thick emulsion that contains a chemical that either absorbs or scatters ultraviolet radiation and is used as a preventative treatment against damaging ultraviolet radiation, which is the current way of treatment used. TiO_2 is a component that is commonly found in sunscreens, where its loading ranges from 2-15%.

Several distinct types of functionalised TiO_2 nanoparticles have been developed for use in nanomedicine as drug transporters, agents for photosensitization and sonosensitization, and photosensitization of sound. TiO_2 has been thought of as a suitable material for drug carriers because the shape and size of TiO_2 nanoparticles can be engineered to control their electronic and chemical properties, and the surface of TiO_2 nanoparticles can be functionalised with a variety of drug molecules [40, 41]. For these reasons, TiO_2 has been considered to be an excellent material for the design of drug carriers.

2.1.2 TiO_2 as a photocatalyst

TiO_2 is regarded as a photocatalytic benchmark semiconductor since it is the most efficient and photocatalytically active photocatalyst when compared to other semiconductors. Its hydroxyl radicals, a powerful oxidizing agent, are capable of degrading organic contaminants (such as dyes, polymers, insecticides, and so on) present at or near the surface of TiO_2, resulting in their total mineralisation into H_2O and CO_2 when exposed to UV light [20, 42–44]. TiO_2 has a quantum mechanical forbidden energy region known as the band gap (EBG), which extends from the top of the valence band (VB) to the bottom of the conduction band (CB). When TiO_2 is exposed to UV light, it produces an excited electronhole pair, which is responsible for its photocatalytic activity. UV light promotes charge separation through excitation of electrons (e^-) from the VB towards the TiO_2 CB, resulting in the formation of holes (h^+) in the VB.

Among many other semiconductors, previous studies have found that TiO_2 outperforms them all. Okaomoto *et al.* discovered that TiO_2 has higher photocatalytic activity than CdS for the breakdown of phenol as a target organic species [45, 46]. According to Sakthivel *et al.*, TiO_2 showed higher photocatalytic efficiency than Fe_2O_3, ZrO_2, CdS, WO_3, and SnO_2 under identical research circumstances [47]. However, Augugliaro *et al.* show that, while ZnO has a lower surface area than TiO_2, it has a higher activity. The same study also found that TiO_2 was photochemically more stable in aqueous conditions than ZnO [48]. In addition, Wu observed that TiO_2 has greater photocatalytic activity than ZnO and SnO_2 [49].

Although TiO_2 has several benefits that make it an outstanding photocatalyst, it also has disadvantages that limit its performance as a photocatalyst. Firstly, due to its broad band gap (3.2 eV), its absorption is a small fraction (5-7%) of the solar spectrum in the UV region, resulting in a low degradation rate and quantum efficiency [44, 50, 51]. Secondly, photoexcitation promotes the formation of a region of positive charge density (hole) caused by the loss of an electron from a site, which might result in a decrease in TiO_2 photocatalytic activity. In photocatalysis, the recombination process to fill this hole is not desirable. Charge recombination in bulk and surface defects can significantly restrict the photocatalytic activity of the material [50, 52–54]. These disadvantages limit TiO_2's large-scale usage. As a result, TiO_2 must be modified to increase its photocatalytic performance. Extensive study has been conducted in recent years to solve the aforementioned issues. Using different approaches, there has been a lot of interest in altering TiO_2 to narrow the band gap and shift the absorption activity toward the visible light range and/or to inhibit the recombination of photogenerated electronhole pairs [54–56].

2.2 Brookite

Because of its complicated structure and the fact that it is extremely difficult to synthesize in its pure form, brookite has been used and studied very infrequently in the field of TiO_2. This is because rutile and anatase have been the subjects of the majority of previous research. In comparison to rutile and anatase, Brookite has a greater number of atoms, which makes DFT calculations more difficult and computationally expensive. Another reason is due to the fact that Brookite is an ore. The properties of brookite have only been reported on by a select few groups up thus far. As a consequence of this, there are not as many data available for brookite in either experimental or theoretical studies in comparison to rutile and anatase. In recent years, there has been a rise in interest in brookite, and recent studies have shown that pure brookite could be a promising candidate for use in photocatalytic applications [57]. Brookite possesses an orthorhombic crystalline structure, as was mentioned earlier, and its unit cell is characterised by the space group Pbca [57, 58]. The structure is made up of octahedra, and each of those octahedra has an atom of titanium at the center of it, and atoms of oxygen at the corners. The octahedra share edges and corners with one another to such a degree that the crystal has the appropriate chemical make-up because of it. The octahedra have been warped, which results in the oxygen atoms being displayed in a pair of distinct orientations [59]. There is a wide variety in the bond lengths that exist between the atoms of titanium and oxygen.

It is helpful to understand the electronic band structure of the TiO_2 polymorphs in order to comprehend the photocatalytic behavior of the pure phases as well as the mixtures of those phases. The band gap values for brookite has been reported to be both smaller and larger than those of anatase in both theoretical and experimental works. By using extended H*ü*ckel molecular orbital calculations, Gratzel and Rotzinger [60] were the first people to estimate the band gap value, also known as Eg, of brookite to be 3.14 eV in the year 1985. The Eg was somewhere in the middle of the band gap energies possessed by anatase (3.23 eV) and rutile (3.02 eV).

Mo and Ching used a technique known as the self-consistent orthogonalized linear combination of atomic orbitals method to investigate the anatase, brookite, and rutile minerals' electronic structures as well as their optical properties [61]. According to the results of their research, brookite has a direct band gap that is 2.20 eV, which is greater than the theoretical calculated gap found in anatase and rutile (1.78 eV for rutile and 2.04 eV for anatase, respectively). According to the findings that were reported by the same authors, this analysis provided an underestimate of the actual band gap values. Using the Kohn-Sham method, Park *et al.* [62] calculated an Eg value of 2.1 eV for brookite. This method routinely and consistently underestimates the band gap by more than 50% most of the time. Recent calculations using the standard density functional theory demonstrated that brookite and rutile each possessed a direct band gap of 1.86 eV, whereas anatase was found to have an indirect band gap of 1.94 eV [63]. The underestimation of the band gap was corrected by employing a more contemporary approximation, and the Eg values of brookite, rutile, and anatase were raised to 3.30 eV, 3.39 eV, and 3.60 eV, respectively.

Since the band gaps of anatase, brookite, and rutile only permit the absorption of the ultraviolet portion of the solar irradiation, many studies have been conducted in recent years to obtain materials that have been doped with either anions or cations, or co-doped with several ions, in order to shift the absorption edge to longer wavelengths. It was discovered that N-doping was particularly effective in increasing the photocatalytic efficiencies of TiO_2 in the visible-light range [64].

2.3 Graphene

The world we live in is rich in materials, and these provide the support structure for our contemporary society. In this group of materials, those based on carbon are popular and play an important part in the development of human civilisation. It is not an overstatement to argue that human life on earth is impossible in the absence of carbon-based materials given the current

state of affairs; in fact, this assertion is not even arguable. For the last 60 years, scientists have speculated on the existence of a two-dimensional (2D) graphene. The term "graphene" was often used to characterise the characteristics of carbon allotropes [65–67]. However, it has been discovered after four decades that graphene also offers a good "condensed matter analogue of (2 + 1)-dimensional quantum electrodynamics", unveiling graphene to a flourishing theoretical "toy" model [68–71]. Because of the development of curved structures such as soot, fullerenes, and nanotubes, graphene was predicted to be unstable. Furthermore, graphene was thought to be non-existent in its free state. Unexpectedly, Geim and Novoselov found freestanding graphene in 2004, confirming the conjecture of graphene [72, 73]. Furthermore, follow-up studies revealed that its charge carriers were, in fact, massless Dirac fermions [74, 75]. As a consequence of this phenomena, graphene has become the material of interest for many Scientific research. Geim and Novoselov were awarded the Nobel Prize in Physics in 2010 for discovering graphene [76–78].

Graphene is defined as a flat single sheet of carbon atoms firmly packed into a honeycomb-like crystalline structure in 2D [72–75]. Furthermore, it is often referred to as the fundamental building block of all other carbon allotropes. Graphene, for example, may be "wrapped to form a zero-dimensional (0D) fullerene, rolled to form one-dimensional (1D) carbon nanotubes, or stacked to form three-dimensional (3D) graphite" (see Figure 2.5) [72–75].

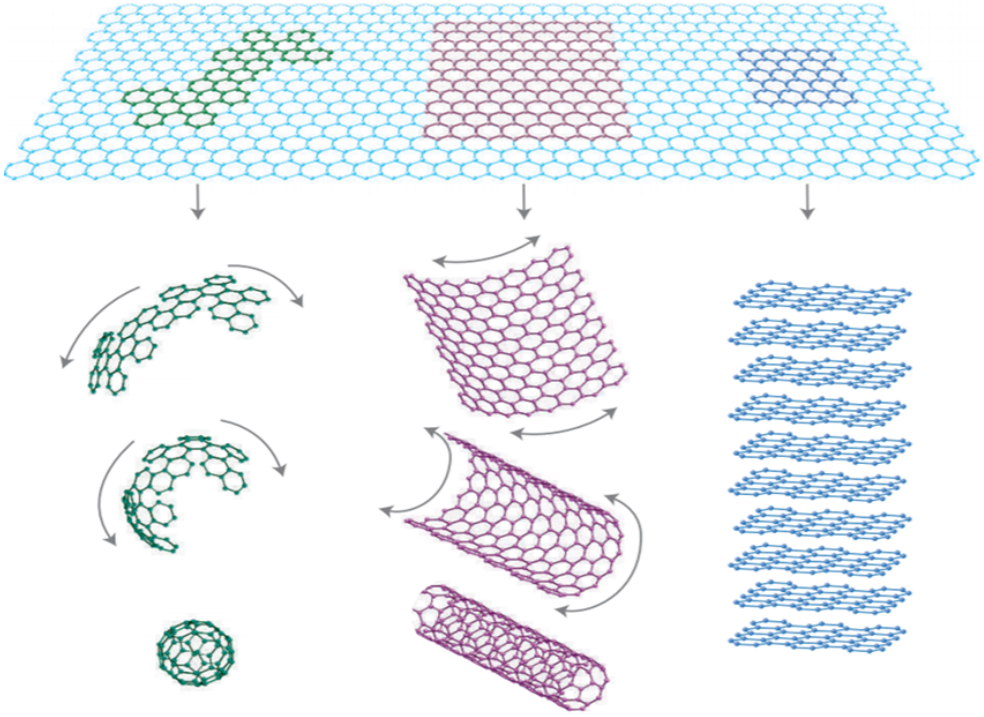

Figure 2.6: Illustration of graphene as a 2D structure and its building block of other carbon dimensionalities including 0D buckyball, 1D nanotube and 3D graphite [71].

A single atomic plane of graphene is termed a 2D crystal, but graphene with more than 100 layers is often regarded as a 3D thin film. However, there is always the issue of how many layers will be required to create this 3D structure. The electrical structur e of graphene has been observed to develop fast with the number of layers, approaching the 3D limit of graphite at precisely 10 layers [79].

Graphene is made up of carbon atoms that are hybridized using the sp^2 configuration of the hexagonal honeycomb structure. The separation between the individual carbon atoms that make up graphene is 1.42 Angstroms (see Figure 2.6). It is a zero-band gap material with a single molecular layered structure [80]. Several intriguing features of pristine graphene have been discovered since 2006. Long range -conjugation in graphene yields extraordinary

physical properties such as high charge-carrier mobility of 250 000 cm^2 v^{-1} s^{-1} at room temperature [81]. It has a large theoretical specific surface area of 2630 m^2 g^{-1} [82, 83], high thermal conductivity of 5000 Wm^{-1} K^{-1} [84], an electrical conductivity of 6000 S cm^{-1} [85] and a Young's modulus of 1.0 TPa [86]. Moreover, a single-layer graphene absorbs only 2.3 of incident light and therefore, it has a transparency of 97.7 [87].

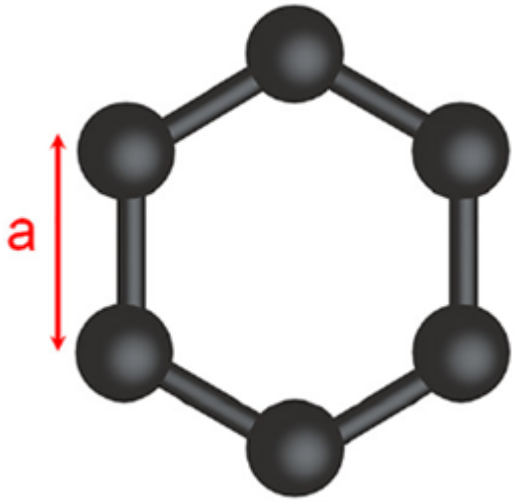

Figure 2.7: Honeycomb lattice of graphene [88].

As can be seen in Figure 2.7, graphene is made up of individual atoms of carbon arranged in a hexagonal pattern. The structure can be visualized as a triangular lattice, and there are two atoms in each unit cell as its fundamental building block. In mathematical terms, the lattice vectors can be expressed as:

$$a_1 = \frac{a}{2}(3, \sqrt{3}), \qquad a_2 = \frac{a}{2}(3, -\sqrt{3}), \tag{2.3}$$

where a $\approx$ 1.42Å is the distance between the carbon atoms [88, 89]. The reciprocal-lattice vectors are represented as follows:

$$b_1 = \frac{2\pi}{3a}(1, \sqrt{3}), \qquad b_2 = \frac{2\pi}{3a}(1, -\sqrt{3}). \tag{2.4}$$

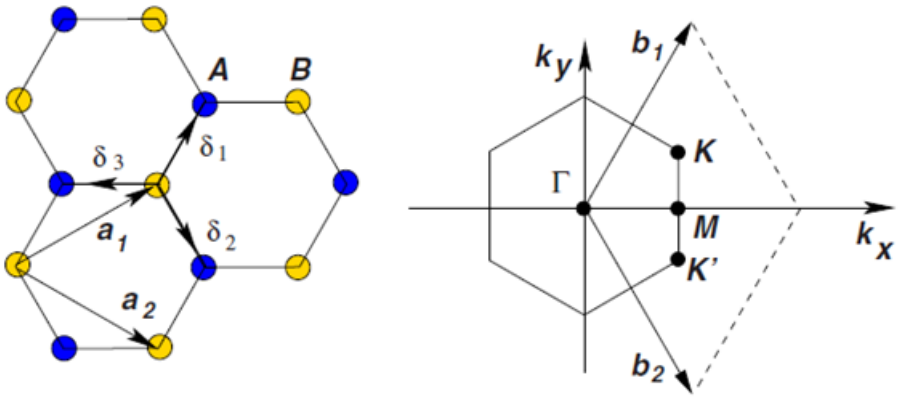

Figure 2.8: A honeycomb lattice of graphene, sub-lattices A and B are shown as black and grey. (b) Reciprocal lattice vectors and some special points in the Brillouin zone [89].

The two points K and K' that are located at the corners of the graphene Brillouin zone BZ are of utmost significance for the study of the physics of graphene. These are referred to as Dirac points and the following equations give their positions in the momentum space [88, 89]:

$$\mathbf{K} = (\frac{2\pi}{3a}, \frac{2\pi}{3\sqrt{3}a}), \qquad \mathbf{K'} = (\frac{2\pi}{3a}, -\frac{2\pi}{3\sqrt{3}a}). \tag{2.5}$$

The three nearest-neighbor vectors in real space are given by:

$$\delta_1 = \frac{a}{2}(1, \sqrt{3}), \qquad \delta_2 = .\frac{a}{2}(1, -\sqrt{3}), \qquad \delta_3 = -a(1, 0) \tag{2.6}$$

The energy band derived from the tight-binding Hamiltonian for electrons in graphene have the following form:

$$E(\mathbf{K}) = t\sqrt{3 + f(\mathbf{K})} - t' f(\mathbf{K}), \tag{2.7}$$

where

$$f(\mathbf{K}) = 2\cos(\sqrt{3}k_y a) + 4\cos\left(\frac{\sqrt{3}}{2}k_y a\right)\cos(\frac{3}{2}k_x a). \tag{2.8}$$

and t and t' are the nearest neighbor hoping for energies. The plus sign applies to the upper and minus sign the lower band. For If $t' = 0$, the energy

band structure is symmetric around zero energy [88,89]. The density of states can be driven from the energy dispersion in Eq. (2.7). In particular, near the Dirac point, the density of states in graphene is given by [88]:

$$\rho(E) = (2A_c/\pi)(|E|/v_F), \tag{2.9}$$

where $A_c = 3\sqrt{3}a^2/2$ and $v_F = 3at/2$. It shows that the density of states is linear to energy, and at the Dirac point, it is zero (Figure 2.9).

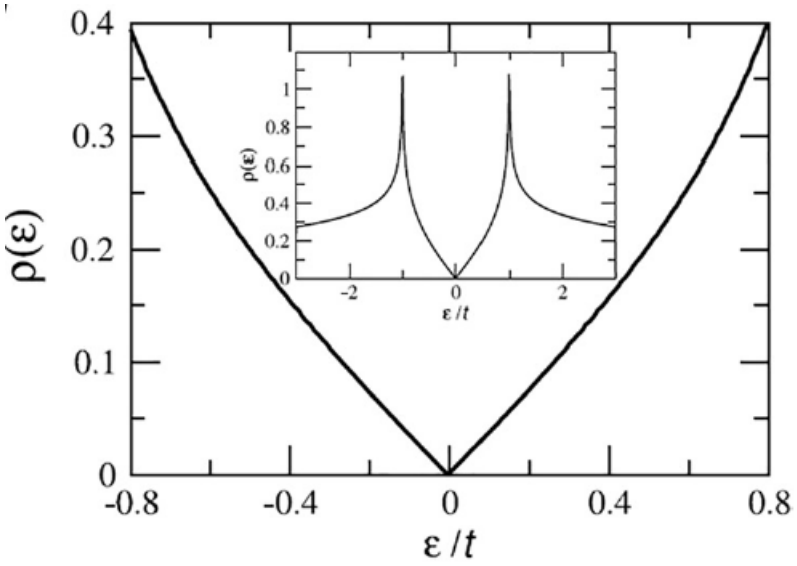

Figure 2.9: The density of states of graphene close to the Dirac point [88].

When one considers that a graphene sheet is only one atom thick, it has a remarkable ability: it can absorb 2.3%. This is because it has the electronic properties that were mentioned above; the electrons behave as massless charge carriers that have exceedingly high mobility. It was not too long ago when it was demonstrated that the amount of white light absorbed is determined by the fine structure constant as opposed to being predetermined by the characteristics of the material. The amount of white light that can be absorbed increases by approximately the same percentage when another layer of graphene is added on top of it. Over the range of visible frequencies, the

opacity of graphene, which is between 2% and 3%, corresponds to a universal dynamic conductivity value of $G = 2e^2/4\hbar$ $(\pm 2 - 3\%)$ [90].

Application of graphene

It is commonly acknowledged that graphene is a ground-breaking material. Graphene has an almost unimaginably wide range of potential applications, many of which have not even been thought of yet [91]. This subsection discusses a few of the most important applications of graphene, presented in a brief format.

Flexible graphene transistors

The transistor based on graphene is a single electron nanoscale device, which means that only one electron at a time can travel through it [92]. Since its inception, this type of transistor has garnered a great deal of attention, and there are now many of them available on the market for use in day-to-day applications [92]. The fact that graphene-based transistors can operate at room temperature and at low voltage while maintaining high sensitivity [92] is the primary benefit of using these transistors. Because of these characteristics, transistors based on graphene are superior to transistors based on silicon, and they also contribute to the advancement of microchip technology. In addition, because of the inherent properties of graphene, transistors of this type can be folded up very easily and are extremely flexible. When compared to silicon, the speed at which electrons can move through graphene is anywhere from 1,000 to 10,000 times faster. Since this is the case, its electron mobility is significantly higher than that of silicon. However, because of problems with its bandgap, pure graphene cannot serve as a substitute for silicon in electronic devices. For graphene, electrons behave similarly to phonons, which is in contrast to their mobility [91].

Graphene sensors

One description of a sensor describes it as "a device that perceives actions that occur in the surroundings (such as heat, motion, light, pressure, mois-

ture, etc.) and retorts with an output, typically in the form of an optical, mechanical, or electrical signal." A simple example is the mercury thermometer used in the home. Because graphene has a large surface-to-volume ratio, exceptional optical properties, excellent electrical conductivity, high carrier mobility and density, high thermal conductivity, etc. [93], graphene and sensors are natural combinations. Graphene also has a high carrier mobility and density. Because graphene has such a large surface area, it is possible to load more desired biomolecules onto its surface. Because of its high conductivity and narrow bandgap, it has the potential to be useful for facilitating the transfer of electrons between biomolecules and electrode surfaces. Because of the two-dimensional, planar, and compatible arrangement of particles in a graphene sheet, a perfect sensor is able to identify even the most minute changes in the condition of its surrounding environment. It is essential to keep in mind that every particle contained within the sheet is subjected to the environment that it is surrounded by [94, 95]. Because of this, graphene is able to accurately recognise changes in its surroundings at the micrometer scale, giving it a high level of affectability. Graphene, like other two-dimensional materials, is capable of distinguishing between individual atomic-scale perturbations [94]. In the field of sensor applications, graphene's characteristics have proven to be useful in significant numbers. Graphene, in its entirety, possesses the potential to be utilised as a component of sensors in a variety of contexts, including but not limited to biosensors, diagnostics, field-effect transistors, DNA sensors, and gas sensors [94, 95].

Graphene for lithium-sulfur battery

Since 1940, numerous types of batteries, including the lithium-sulfur battery, have been manufactured. The Li-S battery, along with others of its kind, suffers from the drawbacks of having a high price tag and a an extremely limited lifespan. In a lithium-sulphur battery, sulphur usually plays the role of the cathode, while lithium takes on the role of the anode. During the discharge process of a lithium-sulfur battery, the lithium at the anode undergoes oxidation and is converted into a lithium-ion, while the sulfur at the cathode undergoes reduction and is converted into a sulfur ion [96]. The lithium ion

will then move toward the cathode, where it will react with the reduced sulfur to produce the lithium sulfide (Li_2S) compound. Due to its amphoteric property, graphene can be incorporated into various battery frameworks as both the anode and the cathode in order to improve the efficiency of the battery and increase the charge/discharge cycle rate by many folds [96]. This will allow for the resolution of all of these problems. Graphene's superlative electrical conductivity, high aspect ratio, and dispersibility make it vastly superior to the conventional inorganic-based cathode while simultaneously mitigating the terminals' constraints [96]. As a two-dimensional material made of carbon atoms, graphene is malleable naturally, which concedes applications on a variety of batteries, including lithium-ion (Li^+) and lithium-sulfur (Li-S) batteries, supercapacitors, and energy saving devices. Such Li-S batteries can deliver energies of up to 500 Wh/kg, and even more when put to use in a real-world setting [96].

Graphene displays

Graphene is an excellent material for use in electron emission displays (EED) due to the fact that it has a high aspect ratio and the dangling bonds at either end of the sheet exhibit proficient electron tunnelling [97]. It is significant that massless Dirac fermions can be produced at the graphene interface. The field outflow will release electrons when it is subjected to an electric field, but it will prevent any back dissipation from occurring because the speed at which it escapes is not dependent on the energy it possesses [98]. Graphene has the ability to activate an electric field at 0.1 V/mm^2 and has a field improvement factor that can reach 3700. Graphene displays are now commercially available and are used in a variety of contexts and applications. In the context of George *et al.*, the investigations were of mechanical behavior of a model touch panel display comprising two layers of CVD grown pure graphene entrenched into PET films in tension and under contact-stress dynamic loading [98]. This model touch panel display was subjected to both static and dynamic loading conditions. Several properties of prototype panel displays based on graphene were investigated for a possible application on real time mobile phone settings. [98] A recent study by Han *et al.* suggests that graphene

might be the best material to use for the development of the next generation of flexible touch panel displays [99].

Structural composites

Graphene is fused into a variety of composites for use in applications in which quality and weight are limiting factors, such as in the aerospace industry [100]. Such a nanosheet has been incorporated into a variety of different materials in order to improve their overall strength, value, and portability. Because a composite material that is significantly lighter than steel while still providing the essential quality will save money on fuel utilisation for the aviation industry, graphene has started to be fused into such materials [100, 101]. Graphene-based basic composites have a massive opportunity to expand their use as innovative replacements for a wide variety of materials currently in use [101].

Catalyst supports

For the purpose of the industrial revolution as well as research and development, catalysis is a fundamentally significant field of study. Graphene and its derivatives have been shown to be very effective as catalytic materials [102]. This is due to their rich surface properties, flake morphology, elevated surface area, and high electron mobility. In the past, many catalytic reactions would make use of a noble metal, which would act as a mechanical support and also as a moderator to increase the rate of reaction and the amount of product produced [102]. Similarly, graphene act as a chemically inert constituent, because in its purest formation, all valence electrons are shared through single bonds among adjacent carbon atoms [102]. The introduction of functional groups, on the other hand, modifies the properties of graphene and makes it appropriate for use in the role of a catalytic support. In addition to this, it has been discovered that the planar and uniform surface of graphene boosts the interfacial interactions that occur between the substrate and the catalyst [102, 103]. Metal catalysts can be positioned accurately on the surface of graphene thanks to the existence of 2D surface morphologies, which also

enables graphene to deliver the highest possible level of performance. In a similar manner, the efficient mechanical background and phenomenal charge bearer capacity of graphene help the charge exchange occur during the reactions by maximising the participation of the catalyst and the substrate [102]. In addition, graphene is inactive and does not take part in the catalytic cycle; as a result, it is ideally suited for use as a support for the catalyst [102, 103]. In a similar vein, graphene promotes the dispersion of catalyst particles, which in turn maximises the amount of contact between the catalyst and its substrate, which, in turn, contributes to the best possible performance of the catalyst [102, 103]. In general, graphene is the material that is best suited for use as a catalytic support, in particular for the developing technology of non-covalently bonded support, which offers low-cost technologies such as fuel cells.

Polymer masterbatches

The incorporation of graphene sheets into polymeric systems is yet another method that might be used to couple these properties for the development of innovative applications. Polymer composites might benefit from this in terms of their improved electrical, thermal, and mechanical properties [104]. In order to engineer such polymeric materials, a homogeneous dispersion of graphene materials, including graphene oxide (GO) and other graphene derivatives, must be incorporated into the polymer matrices. It has been discovered that incorporating graphene and its derivatives into the manufacturing process of polymers leads to a significant increase in the tensile strength of the polymers (4 to 5 fold), as well as an increase in the lifetime of polymeric composites used for commercial purposes [104].

Functional inks

Graphene has also been put to use in the production of functional inks that can withstand heat and corrosion, as well as be used in the electronics industry. The conductivity properties of graphene have an influence on the ink, causing it to become conductive and workable when it is formulated with

graphene. This can be accomplished by incorporating graphene into ink formulations. Graphene ink is nontoxic, environmentally friendly, cheaper, and quite recyclable [105, 106]. In comparison, other conducting inks, including some newly developed nano inks, graphene ink has a number of advantages over them. Because graphene has such a high thermal stability, it is an excellent candidate for the coating of heat-resistant inks that are used in electronic applications that generate a great deal of heat. As a result of the fact that graphene is resistant to decomposition during the production process, this ink is also a good option to go with when processing temperatures need to be elevated. In addition to this, graphene possesses excellent chemical stability, and it is an extremely inert material. Because of these additional benefits, graphene is an excellent candidate for applications involving functional ink [105, 106]. As a result, graphene inks can serve as a reliable barrier that prevents materials from being harmed by chemicals and corrosion in settings where environmental considerations play a significant role in the decision-making process.

2.4 Graphene/metal oxides composite

The incorporation of graphene on the metal oxides can improve the DSSCs performance due to two major factors: the first is that the incorporation increases the electron lifespan [107]. In the metal oxide photoanode, the photogenerated electrons must move through the thick metal oxide film before arriving at the fluorine doped tin oxide (FTO) substrate and have a greater chance of recombining with the photo-generated hole. In the graphene/metal oxide hybrid based DSSCs, the work function of graphene lies between the conduction band of the metal oxide and the conduction band of FTO [108, 109]. When the DSSC is exposed to light, the conduction band of the metal oxide captures the photogenerated electrons from the dye molecules. Since the graphene is incorporated into a metal oxide photoanode, the excited electrons are received by the graphene [107]. Due to its excellent electrical conduction, graphene in this case acts as an electron transfer path

and facilitates the efficient charge transfer from the metal oxide semiconductor to the FTO without any energy barrier [109]. Hence, the graphene incorporation into the metal oxide photoanode behaves as an electron acceptor and transfer for efficient charge separation and fast photogenerated electron transport to prevent charge recombination [110]. The second is that the incorporation of graphene increases the dye absorption: the incorporation creates more sites for the dye molecule adsorption; it causes more light to be gathered and more electrons to be injected from the excited state of the dye into the metal oxide conduction band [108].

Various graphene/metal oxide hybrid based DSSCs were developed in recent years to overcome charge recombination. In a paper by Kim *et al.*, it was reported that graphene oxide/TiO_2 nanocomposites can be applied as interfacial layer between an FTO layer and a nanocrystalline TiO_2 film. The results revealed that the introduction of graphene/TiO_2 increased the photoelectric conversion efficiency from 4.89% to 5.26% [111].

Fang *et al.* [112] studied the influence of different amounts of graphene on the structures and properties of the DSSCs. Their results suggested that the graphene/TiO_2 composite can effectively enhance the open circuit voltage, short circuit current density, and photoelectric conversion efficiency η of the DSSCs with the increase of graphene content [112]. Similarly, Eshaghi and Aghaei deposited graphene-TiO_2 photoanodes with various graphene weight percentages (wt%) from 0 wt% to 2 wt% with an interval of 0.5 wt% on FTO glass substrates as working electrodes for DSSCs [107]. Their results indicated that the graphene incorporation in the TiO_2 photoanode first increased the DSSC efficiency and then decreased it, as the graphene concentration was increased. The maximum DSSC efficiency was obtained with the TiO_2-1.5wt% graphene photoanode and the minimum DSSC efficiency was obtained with the TiO_2-2wt% graphene photoanode [107]. Fan *et al.* [113] further reported TiO_2 nanosheets (TiO_2-NSs) and graphene nanocomposite films based DSSCs fabricated by a direct mechanical mixing and doctor blade method. The results showed that the TiO_2-NSs/graphene

nanocomposite films with moderate loadings (<0.75 wt%) show enhanced photoelectric conversion efficiency compared to their pristine TiO_2-NSs and the loadings (>75 wt%) resulted in an efficiency decrease. Ultimately, the results recorded an efficiency increase of 25% from the studies [113]. Satapathi *et al.* [114] investigated the dependence of the size of graphene sheets on the cell performance whereby their results indicated that as the sheet size decreases, the short circuit current increases. They speculated that the smaller graphene could have helped in enhancement of the surface area and dye loading for better light-harvesting, leading to higher power conversion efficiency [114].

Masuda *et al.* investigated the structural, electronic, and optical properties of several graphene/TiO_2-NS and graphene oxide/TiO_2-NS hybrids focusing on the impact that the presence of a chemical bond between the two layers plays in the final properties of these organic/inorganic composites [115]. Their results indicated that the charge transfer between graphene and TiO_2-NS is observed regardless of the presence of chemical bond, but the chemical bond between the graphene and TiO_2-NS clearly increased the electronic coupling between the two layered components. The physisorbed system did not enhance the photoresponsivity at visible region, while the chemisorbed system was characterised by a higher photoresponsivity in the visible region which is ascribed to the rise of the new valence band maximum state that lies in the prestine bandgap of TiO_2-NS, a consequence of the hybridisation between graphene oxide and TiO_2 [115].

Effendi *et al.* [116] studied the graphene layer and ZnO nanosheets (Gr-ZnO) nanocomposite semiconductor film fabricated by electrodeposition process for DSSCs application. In this study, graphene was used as a capping agent to enhance the surface area of ZnO nanosheets [116]. Investigated effect on photocurrent enhancement signified efficient DSSCs operation when graphene is incorporated into ZnO nanosheets. Acquired results further highlighted that graphene serves as a catalyst on ZnO nanosheets capturing and transportation of electrons injected before recombination process, in order to suppress

electron transfer process [116].

Satish *et al.* investigated the effect of a few layers of graphene incorporated into the SnO_2 photoanode of the SnO_2 based DSSCs [117]. The Weight percentage of the layers was varied from 1.0 to 3.0 wt%. The results showed that by increasing the content of layered graphene, the power conversion efficiency increases. Layered graphene formation works to obstruct charge recombination whilst also enhancing power conversion efficiency of DSSCs. However, for higher weight percentages, beyond optimal value, efficiency of the DSSCs decreases due to light shielding [117].

References

[1] A. Hagfeldt and M. Gratzel, Light-Induced redox reactions in nanocrystalline system, Chemical Reviews, 95, 49, 1995.

[2] D. Wei, Dye sensitized solar cells, International Journal of Molecular Sciences, 11, 1103, 2010.

[3] D. O'Regan and M. Gratzel, A low-cost, high-efficiency solar cell based on dye-sensitized colloidal TiO_2 films, Nature, 353, 737, 1991.

[4] S. P. Sukhatme, J. K. Nayak, Solar energy: Principles of thermal collection and storage, Tata McGraw Hill Education, 2008.

[5] Y. Chiba, A. Islam, Y. Watanabe, R. Komiya, N. Koide and L. Y. Han, Dye-sensitized solar cells with conversion efficiency of 11.1%, Japanese Journal of Applied Physics, 45, 638, 2006.

[6] C. Cavallo, D. Di Pascasio, A. Latini, M. Bonomo and D. Dini, Nanostructured semiconductor materials for dye-sensitized solar cells, Journal of Nanomaterials, 2017, 1, 2017.

[7] Jochen Winkler, Titanium Dioxide: Production, Properties and Effective Usage, Hanover: Vincentz Network, 2014.

[8] R. Asahi, Y. Taga, W. Mannstadt and A. J. Freeman, Electronics and optical properties of anatase TiO_2, Physical Review B, 61, 7459, 2000.

[9] J. Zhang, P. Zhou, J. Liu and J. Yu, New understanding of the difference of photocatalytic activity among anatase, rutile and brookite TiO_2, Physical Chemistry Chemical Physics, 16, 20382, 2014.

[10] K. Li, J. Xu, W. Shi, Y. Wang and T.Peng, Synthesis of size controllable and thermally stable rice-like brookite titania and its application as a scattering layer for nano-sized titania film-based dye-sensitized solar cells, Journal of Materials Chemistry A, 2, 1886, 2014.

[11] A. Mattsson and L Österiund, Adsorption and photoinduced decomposition of acetone and acetic acid on anatase, brookite, and rutile TiO_2 nanoparticles, Journal of Physical Chemistry C. 114, 14121, 2010.

[12] C. M. Teh and A. R. Mohamed, Roles of titanium dioxide and ion-doped titanium dioxide on photocatalytic degradation of organic pollutants (phenolic compounds and dyes) in aqueous solutions: A review, Journal of Alloys and Compounds, 509, 1648, 2011.

[13] H. Zhang and J. F. Banfield, Thermodynamic analysis of phase stability of nanocrystalline titania, Journal of Materials Chemistry, 8, 2073, 1998.

[14] A. A. Gribb and J. F. Banfield, Particle size effects on transformation kinetics and phase stability in nanocrystalline TiO_2, American Mineralogist, 82, 717, 1997.

[15] D. Y. C. Leung, X. Fu, C. Wang, M. Ni, M. K. H. Leung, X. Wang and X. Fu, Hydrogen production over titania-based photocatalysts, ChemSusChem, 3, 681, 2010.

[16] A. Fujishima, X. Zhang and D. A. Tryk, TiO_2 photocatalysis and related surface phenomena, Surface Science Reports, 63, 515, 2008.

[17] A. Sclafani and J. M. Herrmann, Comparison of the photoelectronic and photocatalytic activities of various anatase and rutile forms of titania in pure liquid organic phases and in aqueous solutions, The Journal of Physical Chemistry, 100, 13655, 1996.

[18] A. Primo, A. Corma and H. Garcia, Titania supported gold nanoparticles as photocatalyst, Physical Chemistry Chemical Physics, 13, 886, 2011.

[19] S. Gupta and M. Tripathi, A review of TiO_2 nanoparticles, Chinese Science Bulletin, 56, 1639, 2011.

[20] M. R. Hoffmann, S. T. Martin, W. Choi and D. W. Bahnemann, Environmental applications of semiconductor photocatalysis, Chemical Reviews, 95, 69, 1995.

[21] J. Jitputti, S. Pavasupree, Y. Suzuki and S. Yoshikawa, Synthesis and photocatalytic activity for water-splitting reaction of nanocrystalline mesoporous titania prepared by hydrothermal method, Journal of Solid State Chemistry, 180, 1743, 2007.

[22] G. L. Chiarello, E. Selli and L. Forni, Photocatalytic hydrogen production over flame spray pyrolysis-synthesised TiO_2 and Au/TiO_2, Applied Catalysis B: Environmental, 84, 332, 2008.

[23] K. Tanaka, T. Hisanaga and A. Rivera, Effect of crystal form of TiO_2 on the photocatalytic degradation of pollutants, Photocatalytic purification and treatment of water and air, 169, 1993.

[24] M. Gazquez, J. Bolivar, R. Tonario and F. Vaca, A review of the production cycle of titanium dioxide pigment, Material Science and Applications, 5, 441, 2014.

[25] K. I. Hadjiivanov and D. G. Klissurski, Surface chemistry of titania (anatase) and titania-supported catalysts, Chemical Society Reviews, 25, 61, 1996.

[26] M. Gratzel, Conversion of sunlight to electric power by nanocrystalline dye sensitized solar cells, Journal of Photochemistry and Photobiology A: Chemistry, 164, 3, 2004.

[27] M. Ni, M. Leung and K. Sumathy, A review and recent developments in photocatalytic water-splitting using TiO_2 for hydrogen production, Renewable and Sustainable Energy Reviews, 11, 401, 2007.

[28] G. Smestad, C. Bignozzi and R. Argazzi, Testing of dye sensitized TiO_2 solar cells I: Experimental photocurrent output and conversion efficiencies, Solar Energy Materials and Solar Cells, 32, 259, 1994.

[29] A. Hagfeldt and M. Gratzel, Molecular photovoltaics, Accounts of Chemical Research, 33, 269, 2000.

[30] Y. Cao, Y. Bai, Q. Yu, Y. Cheng, S. Liu, D Shi, F. Gao and P. Wang, Dye-sensitized solar cells with a high absorptivity ruthenium sensitizer featuring a 2- (hexylthio)thiophene conjugated bipyridine, The Journal of Physical Chemistry C, 113, 6290, 2009.

[31] L. Kavan, Electrochemistry of titanium dioxide: some aspects and highlights, Chem. Record, 12, 131, 2012.

[32] Z. Yang, D. Choi, S. Kerisit, K. M. Rosso, D. Wang, J. Zhang, G. Graff and J. Liu, Nanostructures and lithium electrochemical reactivity of lithium titanites and titanium oxides: A review, Journal of Power Sources, 192, 588, 2009.

[33] A. Fujishima and A. Zhang, Titanium dioxide photocatalysis: present situation and future approaches, Comptes Rendus Chimie, 9, 750, 2006.

[34] C. Trapalis, P. Keivanidis, G. Kordas, M. Zaharescu, M. Crisan, A. Szatvanyi and M. Gartner, Nanostructured thin films with antibacterial properties, Thin Solid Films, 433, 186, 2003.

[35] P. G. Smirniotis, A. P. Donovan and B. S. Uphade, Low-temperature selective catalytic reduction (SCR) of NO with NH_3 by using Mn, Cr, and Cu oxides supported on Hombikat TiO_2, Angewandte Chemie International Edition, 40, 2479, 2001.

[36] H. Huang, R. Long and R. Yang, A highly sulfur resistant Pt-Rh/TiO/Al_2O_3 storage catalyst for NO_x reduction under leanrich cycles, Applied Catalysis B: Environmental, 33, 127, 2001.

[37] G. Busca, L. Lietti, G. Ramis and F. Berti, Chemical and mechanistic aspects of the selective catalytic reduction of NO_x by ammonia over oxide catalysts: A review, Applied Catalysis B: Environmental, 18, 1, 1998.

[38] J. P. Dunn, H. G. Stenger and I. E Wachs, Oxidation of sulfur dioxide over supported vanadia catalysts: molecular structure-reactivity relationships and reaction kinetics, Catalysis Today, 51, 301, 1999.

[39] J. Lai and I. E. Wachs, A perspective on the selective catalytic reduction (SCR) of NO with NH_3 by supported V_2O_5-WO_3/TiO_2 catalysts, ACS Catalysis, 8, 6537, 2018.

[40] T. Wang, H. Jiang, L Wan, Q. Zhao, T. Jiang, B. Wang and S. Wang, Potential application of functional porous TiO_2 nanoparticles in light-controlled drug release and targeted drug delivery, Acta Biomaterialia, 13, 354, 2015.

[41] Q. Wang, J. Huang, H. Li, Z. Chen, Z. Zhao, Y. Wang, K. Zhang, H. Sun, S. Al-Deyab and Y. Lai, TiO_2 nanotube platforms for smart drug delivery: a review, International Journal of Na nomedicine, 11, 4819, 2016.

[42] A. Mills and S. Le Hunte, An overview of semiconductor photocatalysis, Journal of Photochemistry and Photobiology A: Chemistry, 108, 1, 1997.

[43] A. Mills, C. Hill and P. K. J. Robertson, Overview of the current ISO tests for photocatalytic materials, Journal of Photochemistry and Photobiology A: Chemistry, 237, 7, 2012.

[44] V. K. Gupta, R. Jain, A. Nayak, S. Agarwal and M. Shrivastava, Removal of the hazardous dye-Tartrazine by photodegradation on titanium dioxide surface, Materials Science and Engineering: C, 31, 1062, 2011.

[45] K. Okamoto, Y. Yamamoto, H. Tanaka and A. Itaya, Kinetics of heterogeneous photocatalytic decomposition of phenol over anatase TiO_2 powder, Bulletin of the Chemical Society of Japan, 58, 2023, 1985.

[46] K. Okamoto, Y. Yamamoto, H. Tanaka, M. Tanaka and A. Itaya, Heterogeneous photocatalytic decomposition of phenol over TiO_2 powder, Bulletin of the Chemical Society of Japan, 58, 2015, 1985.

[47] S. Sakthivel, B. Neppolian, B. Arabindoo, M. Palanichamy and V. Murugesan, TiO_2 catalysed photodegradation of leather dye, Acid Green 16, Journal of Scientific & Industrial Research, 59, 556, 2000.

[48] V. Augugliaro, L. Palmisano, A. Sclafani, C. Minero and E. Pelizzetti, Photocatalytic degradation of phenol in aqueous titanium dioxide dispersions, Toxicological & Environmental Chemistry, 16, 89, 1988.

[49] C.H. Wu, Comparison of azo dye degradation efficiency using UV/single semiconductor and UV/coupled semiconductor systems, Chemosphere, 57, 601, 2004.

[50] M. Pelaez, N. T. Nolan, S. C. Pillai, M. K. Seery, P. Falaras, A. G. Kontos, P. S. M. Dunlop, J. W. J. Hamilton, J. A. Byrne, K. O'Shea, M. H. Entezari and D. D. Dionysiou, A review on the visible light active titanium dioxide photcatalysts for environmental applications, Applied Catalysis B: Environmental, 125, 331, 2012.

[51] N. Serpone and A. V. Emeline, Semiconductor photocatalysis - Past, present, and future outlook, The Journal of Physical Chemistry Letters, 3, 673, 2012.

[52] F. Amano, O.O. Prieto-Mahaney, Y. Terada, T. Yasumoto, T. Shibayama and B. Ohtani, Decahedral single-crystalline particles of anatase titanium(IV) oxide with high photocatalytic activity, Chemistry of Materials, 21, 2601, 2009.

[53] Y. Wu, H. Liu, J. Zhang and F. Chen, Enhanced photocatalytic activity of nitrogen- doped titania by deposited with gold, The Journal of Physical Chemistry C, 113, 14689, 2009.

[54] S. Ahmed, M. G. Rasul, W. Martens, R. Brown and M. A. Hashib, Advances in heterogeneous photocatalytic degradation of phenols and dyes in wastewater: A Review, Water Air Soil Pollut, 215, 3, 2011.

[55] Papi, Sanja, N. Koprivanac, Bo, A. Lon, ari, Vujevi, Dinko, Dragi, evi, S. Ku, ar, Ku, Hrvoje and I. Peternel, Advanced oxidation processes in azo dye wastewater treatment, Water Environment Research, 78, 572, 2006.

[56] M. V. Dozzi, L. Prati, P. Canton and E. Selli, Effects of gold nanoparticles deposition on the photocatalytic activity of titanium dioxide under visible light, Physical Chemistry Chemical Physics, 11, 7171, 2009.

[57] A. Di Paola, M. Bellardita and L. Palmisano, Brookite, the least known TiO_2 photocatalyst, Catalysts, 3, 36, 2013.

[58] L. Pauling and J. H. Sturdivant, The crystal structure of brookite, Zeitschrift fur Kristallographie, 68, 239, 1928.

[59] X. Bokhimi, A. Morales, M. Aguilar, J. A. Toledo-Antonio and F. Pedraza, Local order in titania polymorphs, International Journal of Hydrogen Energy, 26, 1279, 2001.

[60] M. Gratzel and F. P. Rotzinger, The influence of the crystal lattice structure on the conduction band energy of oxides of titanium(IV), Chemical Physics Letters, 118, 474, 1985.

[61] S. D. Mo,and W. Y. Ching, Electronic and optical properties of three phases of titanium dioxide: Rutile, anatase and brookite, Physical Review B, 51, 13023, 1995.

[62] J. Y. Park, C. Lee, K. W. Jung and D. Jung, Structure related photocatalytic properties of TiO_2. Bulletin of Korean Chemical Society, 30, 402, 2009.

[63] M. Landmann, E. Rauls and W. G. Schmidt, The electronic structure and optical response of rutile, anatase and brookite TiO_2, Journal of Physics, 24, 2012.

[64] R. Asahi, T. Morikawa, T. Ohwaki, K. Aoki and Y. Taga, Visible-light photocatalysis in nitrogen-doped titanium oxides, Science, 293, 269, 2001.

[65] P. R. Wallace, The band theory of graphite, Physical Review, 71, 622, 1947.

[66] J. W. McClure, Diamagnetism of graphite, Physical Review, 104, 666, 1956.

[67] J. C. Slonczewski and P. R. Weiss, Band structure of graphite, Physical Review, 109, 272, 1958.

[68] G. W. Semenoff, Condensed-matter simulation of a three-dimensional anomaly, Physical Review Letters, 53, 2449, 1984.

[69] E. Fradkin, Critical behavior of disordered degenerate semiconductors, Physical Review B, 33, 3263, 1986.

[70] F. D. M. Haldane, Model for a quantum Hall effect without Landau levels: Condensed-matter realization of the "parity anomaly", Physical Review Letters, 61, 2015, 1988.

[71] A. K. Geim and K. S. Novoselov, The rise of graphene, Nature Materials, 6, 183, 2007.

[72] K. S. Novoselov, A. K. Geim, S. V. Morozov, D. Jiang, Y. Zhang, S. V. Dubonos, I. V. Grigorieva and A. A. Firsov, Electric field effect in atomically thin carbon films, Science, 306, 666, 2004.

[73] D. Jiang, F. Schedin, T. J. Booth, V. V. Khotkevich, S. V. Morozov and A. K. Geim, Two-dimensional atomic crystals, Proceedings of the National Academy of Sciences of the United States of America, 102, 10451, 2005.

[74] K. S. Novoselov, A. K. Geim, S. V. Morozov, D. Jiang, M. I. Katsnelson, I. V. Grigorieva, S. V. Dubonos and A. A. Firsov, Two-dimensional gas of massless Dirac fermions in graphene, Nature, 438, 197, 2005.

[75] Y. Zhang, J. W. Tan, H. L. Stormer and P. Kim, Experimental observation of the quantum Hall effect and Berry's phase in graphene, Nature, 438, 201, 2005.

[76] G. Brumfiel, Andre Geim: In Praise of Graphene, October 7, doi:10.1038/news.2010.525 (2010). http://www.nature.com/news/2010/101007/full/news.2010.525.html.

[77] Associated Press, Graphene Pioneers Earn Nobel Prize in Physics, October 5, 2010. http://www.foxnews.com/scitech/2010/10/05/uk-nobel-prize-physics-graphene/.

[78] CNN Wire Staff, Research into Graphene Wins Nobel Prize, October 5, 2010. http://www.cnn.com/2010/LIVING/10/05/sweden.nobel.physics/index.html.

[79] B. Partoens and F. M. Peeters, From graphene to graphite: Electronic structure around the K point, Physical Review B, 74, 075404, 2006.

[80] R. Nair, P. Blake, A. Grigorenko, K. Novoselov, T. Booth, T. Stauber, N. Peres and A. Gein, Fine structure constant defines visual transparency of graphene, Science, 320, 1308, 2008.

[81] M. Ortila, C. Faugeras, P. Plochocka, P. Neugebauer, G. Martinez, D. K. Maude, A. L. Barra, M. Sprinkle, C. Berger, W. A. de Heer and M. Potemski, Approaching the Dirac point in high mobilty multilayer epitaxial graphene, Physical Review Letter, 101, 267601, 2008.

[82] Y. Zhu, S. Murali, W. Cai, X. Li, J. W. Suk, J. R. Potts and R. S. Ruof, Graphene and Graphene Oxide: Synthesis, Properties and Applications, Advanced Materials, 22, 3906, 2010.

[83] C. M. Weber, D. M. Eisele, J. P. Rabe, Y. Liang, X. Feng, L. Zhi, K. Mullen, J.L. Lyon, R. Williams, D. A. V. Bout and K. J. Stevenson, Small, 6, 184, 2011.

[84] A. A. Balandin, S. Ghosh, W. Bao, I. Calizo, D. Teweldebrhan, F. Miao and C. N. Lau, Superior thermal conductivity of single-layer graphene, Nano Letter, 8, 902, 2008.

[85] X. Du, I. Skachko, A. Barker and E. Y. Andrei, Approaching ballistic transport in suspended graphene, Nature Nanotechnology, 3, 491, 2008.

[86] C. Lee, X. Wei, J. W. Kysar and J. Hone, Measurement of the elastic properties and intrinsic strength of monolayer graphene, Science, 321, 385, 2008.

[87] S. Pang, Y. Hernandez, X. Feng and K. Mullen, Graphene as Transparent Electrode Material for Organic Electronics, Advanced. Materials, 23, 2779, 2011.

[88] X. Li, L. Tao, Z. Chen, H. Fang, X. Li, X. Wang, J. Xu and H. Zhu, Graphene and related two-dimensional materials: Structure-property relationships for electronics and optoelectronics, Applied Physics Review, 4, 021306, 2017.

[89] A. H. Castro Neto, N. M. R. Peres, K. S. Novoselov and A. K. Geim, The electronic properties of graphene, Reviews of Morden Physics, 81, 1, 2009.

[90] J. D. L. Fuente, Graphene properties. 2014 [cited 2015 April]; Available from: http://www.graphenea.com/pages/graphene-properties#.VUoKxEfF-55.

[91] S. K. Tiwari, S. Sahoo, N. Wang and A. Huczko, Graphene research and their outputs: Status and prospect, Journal of Science: Advanced Materials and Devices, 5, 10, 2020.

[92] S. He, Y. Qian, K. Liu, C. W. Macosko and A. Stein, Modified-graphene-oxidecontaining styrene masterbatches for thermosets, Industrial and Engineering Chemistry Research, 56 (40) 11443, 2017.

[93] P. Goli, H. Ning, X. Li, C. Y. Lu, K. S. Novoselov and A. A. Balandin, Thermal properties of graphene-copper-graphene heterogeneous films, Nano Letters, 14 (3), 1497, 2014.

[94] D. Cohen-Tanugi and J. C. Grossman, Mechanical strength of nanoporous graphene as a desalination membrane, Nano Letters, 14 (11), 6171, 2014.

[95] Y. Zhao, X. G. Li, X. Zhou and Y. N. Zhang, Review on the graphene based optical fiber chemical and biological sensors, Sensor. Actuator. B Chemical, 231, 324, 2016.

[96] J. Song, Z. Yu, M. L. Gordin and D. Wang, Advanced sulfur cathode enabled by highly crumpled nitrogen-doped graphene sheets for high-energy-density lithiumesulfur batteries, Nano Letters, 16 (2), 864, 2016.

[97] G. Qu, J. Cheng, X. Li, L. Huang, W. Ni, Z. Wang and B. Wang, Graphene-enveloped poly (N-vinylcarbazole)/Sulfur composites with improved performances for lithiumesulfur batteries by A simple vibrating-emulsification method, ACS Applied Material Interfaces, 7 (30), 16668, 2015.

[98] G. Anagnostopoulos, P. N. Pappas, Z. Li, I. A. Kinloch, R. J. Young, K. S. Novoselov, C. Y. Lu, N. Pugno, J. Parthenios, C. Galiotis and K. Papagelis, Mechanical stability of flexible graphene-based displays, ACS Applied Material Interfaces, 8 (34), 22605, 2016.

[99] T. H. Han, H. Kim, S. J. Kwon and T. W. Lee, Graphene-based flexible electronic devices, Materials Science and Engineering R: Reports, 118, 1, 2017.

[100] G. Mittal, V. Dhand, K. Y. Rhee, S. J. Park and W. R. Lee, A review on carbon nanotubes and graphene as fillers in reinforced polymer nanocomposites, Journal of Industrial and Engineering Chemestry, 21, 11, 2015.

[101] V. Mittal, Functional polymer nanocomposites with graphene: a review, Macromolecular Materials and Engineering, 299 (8), 906, 2014.

[102] C. M. Wu, S. S. Cheong and T. H. Chang, Rheological properties of graphene/nylon 6 nanocomposites prepared by masterbatch melt mixing, Journal of Polymer Research, 23 (12), 242, 2016.

[103] X. Zhou, J. Qiao, L. Yang and J. Zhang, A review of graphene-based nanostructural materials for both catalyst supports and metal-free catalysts in PEM fuel cell oxygen reduction reactions, Advanced Energy Materials, 4 (8), 1301523, 2014.

[104] L. T. Soo, K. S. Loh, A. B. Mohamad, W. R. W. Daud and W. Y. Wong, An overview of the electrochemical performance of modified graphene used as an electron catalyst and as a catalyst support in fuel cells, Apllied Catalysis A: General, 497, 198, 2015.

[105] K. Hu, D. D. Kulkarni, I. Choi and V. V. Tsukruk, Graphene-polymer nanocomposites for structural and functional applications, Progress in Polymer Science, 39 (11), 1934, 2014.

[106] E. Antolini, Nitrogen-doped carbons by sustainable N-and C-containing natural resources as nonprecious catalysts and catalyst supports for low temperature fuel cells, Renewable and Sustainable Energy Reviews, 58, 34, 2016.

[107] A. Eshaghi and A. A. Aghaei, Effect of TiO_2-graphene nanocomposite photoanode on dye-sensitized solar cell performance, Bulleting of Materials Science, 38 (5), 1177, 2015.

[108] Y. B. Tang, C. S. Lee, J. Xu, Z. T. Liu, Z. H. Chen, Z. He, Y. L. Cao, G. Yuan, H. Song, L. Chen, L. Luo, H. M. Cheng, W. J. Zhang, I. Bello and S. T. Lee, Incorporation of graphenes in nanostructured TiO_2 films via molecular grafting for dye-sensitized solar cell application, ACS Nano, 4, 3482, 2010.

[109] S. Sun, L. Gao and Y. Liu, Enhanced dye-sensitized solar cell using graphene-TiO_2 photoanode prepared by heterogeneous coagulation, Applied Physics Letter, 96, 083113, 2010.

[110] L. Chen, Y. Zhou, W. Tu, Z. Li, C. Bao, H. Dai, T. Yu, J. Liu and Z. Zou, Enhanced photovoltaic performance of a dye-sensitized solar cell using graphene-TiO_2 photoanode prepared by a novel in situ simultaneous reduction-hydrolysis technique, Nanoscale, 5, 3481, 2013.

[111] S. R. Kim, M. K. Parvez and M. Chhowall, UV-reduction of graphene oxide and its application as an interfacial layer to reduce the back-transport reactions in dye-sensitized solar cells, Chemical Physics Letter, 483, 124, 2009.

[112] X. Fang, M. Li, K. Guo, X. Liu, Y. Zhu, B. Sebo and X. Zhao, Graphene-compositing optimization of the properties of dye-sensitized solar cells, Solar Energy, 101, 176, 2014.

[113] J. Fan, S. Liu and J. Yu, Enhanced photovoltaic performance of dye-sensitized solar cells based on TiO_2 nanosheets/graphene composite films, Journal of Materials Chemistry, 22, 17027, 2012.

[114] S. Satapathi, H. S. Gill, S. Das, L. Li, L. Samuelson, M. J. Green and J. Kumar, Performance enhancement of dye-sensitized solar cells by incorporating graphene sheets of various sizes, Applied Surface Science, 314, 638, 2014.

[115] Y. Masuda, G. Giorgi and k. Yamashita, DFT study of anatase-derived TiO_2 nanosheets/graphene hybrid materials, Physica Status Solidi B, 251 (8), 1471, 2014.

[116] N. A. S. Effendi, N. S. Samsi, S. A. Zawawi, O. H. Hassan, R. Zakaria, M. Z. A. Yahya and A. M. M Ali, Studies on Graphene Zinc-Oxide Nanocomposites Photoanodes for High-Efficient Dye-Sensitized Solar Cells, AIP Conference Proceedings, 1877, 090005, 2017.

[117] S. Bykkam, K. V. Rao and C. S. Chakra, Enhanced photovoltaic efficiency of dye sensitized solar cell by few layered graphene sheet decked with SnO_2 nanopartilces as a photoanode, Journal of Nanoscience and Technology, 2(2), 144, 2016.

Chapter 3

Methodology

3.1 Density functional theory

3.1.1 Schrödinger equation

To understand how atoms interact with each other to form molecules and crystals, one needs to understand the structure of electrons and nuclei and their motion that compromises each atom. In describing the properties of systems of atoms, the first step is to find the ground state. When two atoms' bond, they do it in a way that lowers the energy of the electrons. The minimal energy is achieved when electrons are at their correct orbitals and nuclei at their correct locations [1]. The challenging task is finding this energy. Once found it allows other physical properties to be derived. The density functional theory used in this work describes the energy of electrons starting from the simplest quantum mechanics' approach.

Quantum mechanics provides a reliable approach to calculating what the electrons and atomic nuclei do in any situation. The behaviour of electrons in particular governs most of the properties of materials. This is true for a single atom or assemblies of atoms in a condensed matter, because quantum mechanics describes and explains the chemical bond. Therefore, the properties of any material can be understood from first principle that is based on physical laws and without using free parameters by solving the Schrödinger equation of an electron in the material [2]. In quantum mechanics, a sys-

tem of M nuclei and N electrons is described respectively by the coordinates $R \equiv R_1,,R_M$ and $r \equiv r_1,,r_N$. All the information is contained in the wavefunction (r, R) solution of a time-independent Schrödinger's equation,

$$H\psi(r, R) = E\psi(r, R). \tag{3.1}$$

The Hamiltonian (H) of the system representing the total sum of energy (E) in a conservative system, is given by:

$$H = T_N + T_e + V_{ee}(r) + V_{eN}(r, R) + V_{NN}(R) \tag{3.2}$$

where T_N and T_e are the nuclear and electron kinetic energy operators respectively, $V_{ee}(r)$, $V_{eN}(r, R)$ and $V_{NN}(R)$ are the electron-electron, electron-nuclear and nuclear-nuclear interaction potential operators, respectively. ψ is the wavefunction of a system, representing the quantum state of the electrons in the system and E is the ground state energy of the system. The Hamiltonian in Equation (3.2) is universal, and if it is solvable, one can recover the stationary states and energies of the system. However, the problem of interacting electron in condensed matter physics is a tall order and hence it is important to solve Equation (3.2) exactly, and it requires a series of approximations and tricks, of which some are briefly described in the next subsections.

3.1.2 Born-Openheimer approximation

The Born-Openheimer approximation is one method that reduces the degree of freedom, it states: the electron wavefunction depends upon the nuclear positions but not upon their velocities, i.e, the nuclear motion is so much slower than the electron motion that they can be considered to be fixed. Within this approximation, the nuclear kinetic energy, T_N can be neglected in Equation (3.2) and the interaction V_{NN} can be considered to be constant. Now, the terms remaining in Equation (3.2) form what we call the electronic Hamiltonian [3],

$$H_{el}(r, R) = T_e + V_{ee}(r) + V_{eN}(r, R) \ , \tag{3.3}$$

and the solution to the Schrödingers equation for the electronic Hamiltonian,

$$H_{el}(r,R)\psi_n(r,R) = \varepsilon_n(R)\psi_n(r,R) \ , \tag{3.4}$$

are the electronic wavefunction, as the electronic energies, only parametrically on the nuclear positions. As the nuclei move much slower than the electrons, the electronic coordinates in Equation (3.2) can be replaced by the values averaged over the electronic wavefunction $\psi_n(r,R)$. This gives a Hamiltonian, describing the nuclei motion in the average field of the electrons [3],

$$H_N(R) \equiv T_N + V_{NN}(R) + \varepsilon_n(R) \ . \tag{3.5}$$

Equation (3.5) shows that the nuclei move in potential energy surface $V_{NN} + \varepsilon_n(R)$ set up by the electrons, known as Born-Openheimer surfaces. Thus, the many-electron problem defined by Equation (3.4) is of utmost importance in quantum chemistry.

3.1.3 One-electron methods

The solution of the Schrödinger equation for a system of N interacting electrons in a field created by M nuclei is an exceedingly difficult problem, which makes necessary to simplify Equation (3.4). The first approximation, proposed by Hartree, postulated that the electronic wavefunction could be written as the product of one-electron wavefunctions [4]. Each of them satisfies a single-particle Schrödinger equation with an effective potential that takes into account the interaction with the nuclei and the other electrons in a mean field way. The Hartree approximation can be improved by introducing the Pauli Exclusion Principle, which demands that the many electron wavefunction be antisymmetric with respect to interchange of any two electron coordinates. This can be achieved using an antisymmetrised wavefunction resulting from a Slater determinant, within the Hartree-Fock (HF) approximation [5]. The single-particle HF equations are derived from minimization of the total energy with respect to the HF orbitals. They include an integral involving only orbitals of the same spin, the so-called exchange term operator, which adds a lot of complexity to the problem. Although many-body

correlations are completely neglected, HF is used as a starting point for more accurate approaches where the electronic wavefunction is given by a linear combination of Slater determinants [6].

3.1.4 Hohenberg-Kohn theorems

In 1964, Hohenberg and Kohn proved two theorems [7]:

1. The ground state electron density $n_o(r)$ uniquely determines the external potential $V_{ext}(r)$ (to within an additive constant) that is due to the nuclei, felt by an arbitrary number of electrons N in a large box.

2. For a given $V_{ext}(r)$, an energy functional can be defined in terms of the density:

$$E[n] = \int V_{ext}(r)n(r)dr + F[n] + E_{NN} \ , \tag{3.6}$$

where $F[n]$ includes the kinetic energy $T[n]$ and the interaction energy of the electrons $E_{int}[n]$.

$F[n]$ is a universal functional (i.e., it does not depend on the external potential which represents the particular system of interest) which if its form was known, the problem of determining the ground state energy and density would be easily solved by minimising $E[n]$.

3.1.5 Kohn-Sham scheme

A year later after the Hohenberg-Kohn theorems, Kohn and Sham simplified the HK-theorems to the major physical interactions in the system [8]. In the Kohn and Sham scheme, the many-electron problem is replaced with a set of self-consistence and single particle equations. The kinetic energy functional here is made up of non-interacting electrons, taken from single electron orbitals. The energy functional is then expressed as:

$$E_{KS}[n] = T_s[n] + \int n(r)V_{ext}(r)dr + E_H[n] + E_{XC}[n] + E_{NN} \ , \tag{3.7}$$

where T_S represents the kinetic energy of the non-interacting electrons and E_H represents the Coulombic interactions between electrons. E_{xc} is an error correction called exchange-correlation energy. This functional arises from the simplifications to the kinetic energy and electron-electron interactions. E_{xc} is the only term that cannot be evaluated exactly. Kohn and Sham substituted the new energy functional into the wave equation and reached to the following Kohn-Sham equations:

$$\Big[-\frac{1}{2} \bigtriangledown^2 + V_{ext}(r) + \int \frac{n(r')}{|r - r'|} dr' + V_{xc}(r) \Big] \phi_i(r) = \varepsilon_i \phi_i(r) \tag{3.8}$$

and

$$V_{xc}(r) = \frac{\delta E_{xc}[n]}{\delta n} \ . \tag{3.9}$$

In the brackets (that is the Hamiltonian operator), the first term represents the kinetic energy of the electron, second term is the external potential on the electron, third term is the sum of all Coulombic interactions on the electron due to every other electron and the fourth term is the exchange correlation. The second equation tells us that the exchange correlation operator is the derivative of the exchange correlation functional with respect to the electron density. Now finding the exchange correlation energy is a tall order task. If the exchange correlation energy were known, the K-S would perfectly describe the exact ground state energy of the interacting system. Unfortunately, that is not the case, and hence further approximations needed to be done to approximate the exchange correlation energy.

3.1.6 Approximations for E_{xc}

To further their approxiations, Kohn and Sham proposed the local density approximations (LDA). LDA approximates the exchange correlation energy at each point, r with density, $n(r)$ to that of uniform electron gas with the same density, $\varepsilon_{xc}(n)$. Now the exchange correlation energy is simply given by [1]:

$$E_{xc}^{LDA}[n] = \int n(r) \varepsilon_{xc}(n) dr = \int n(r) \{ \varepsilon_x(n) + \varepsilon_c(n) \} dr \ , \tag{3.10}$$

where ε_x is the exchange term and ε_c is the correlation term. A significant improvement of the LDA was achieved by considering the gradient of the electron density and making E_{xc} a functional of the density. This approach is called the generalised gradient approximations (GGA) and is represented as:

$$E_{xc}^{GGA}[n] = E_{xc}[n(r), \bigtriangledown n(r)] \tag{3.11}$$

GGA only incorporates the first derivatives of the density in its calculations (plus the condition that the Fermi and Coulomb holes integrate to the required values). Depending on the form of $E_{xc}[n(r), \bigtriangledown n(r)]$, there are different parameterizations of GGA. The most commonly used is the Perdew-Burke-Ernzerhof (PBE) [9]. The exchange-correlation functional that is activated by default is the GGA-PBE. In terms of providing a better description of the electronic subsystem, the GGA excels beyond that of the LDA functionals.

Hybrid density functionals combine a part of the exchange energy derived from the density functional calculation for electron gas (i.e. GGAs or the LDA) with the exchange energy derived from the Hartree-Fock calculation [10]. One of the most well-known examples of a gradient-corrected exchange functional is the one that was introduced by Becke in 1988 [11]. The LYP functional developed by Lee, Yang, and Parr is a well-known example of a gradient-corrected correlation functional [12]. B-LYP is the abbreviation for the combination of the two functionals, Becke for the exchange component and LYP for the correlation component. Becke represents the exchange component. One of Becke's three-parameter formulations that is employed the most often is the B3LYP, which is a hybrid functional. The mathematical form of the B3LYP functional has three semi-empirical parameters, which are denoted by the letters a, b, and c. The values of these parameters let one to duplicate the exchange-correlation energy of 31 different pre-selected molecular species, expressed analytically as:

$$E_{xc}^{B3YLP} = (1-a)E_x^{LDA} + aE_x^{HF} + b\Delta E_x^{BECKY} + cE_c^{LYP} + (1-c)a_cE_c^{VWN} \tag{3.12}$$

where E_x^{HF} is the exchange energy from a Hartree-Fock calculation, E_x^{BECKY} is the gradient correction to the LDA exchange, E_c^{LYP} is the gradient corrected correlation energy and E_c^{VWN} is the LDA correlation energy. The values for the mixing parameters are as follows: a = 0.2, b = 0.72, and c = 0.81 [13]. When it comes to studying the electrical structure of moderate to large systems, the density functional theory is often the technique of choice. This preference is a reflection of the effectiveness of DFT in comparison to correlated wavefunction theories such as coupled cluster theory [11, 13].

3.2 Software

The study of graphene/metal oxides was conducted using Material Studio computing software. Material Studio is a software for simulation and modeling materials, developed and distributed by Accelrys [14, 15]. It is used for studying various materials such as ceramics, metals, polymers, and so on. Inside Material Studio there is a package called Cambridge Serial Total Energy Package (CASTEP) programme [14, 15]. The CASTEP programme performs electronic structure calculations using the density functional theory. It is used to simulate a wide range of materials including crystalline solids, surfaces, molecules, liquids and amorphous materials [2, 14]. The physical properties of materials that can be calculated using CASTEP include: total energies, electronic structure, geometry optimisation, molecular dynamics, transition states, phonons, electric field response and exchange and correlation [14].

Researchers are able to investigate the nature and origin of the electronic, optical, and structural properties of a system through the use of first principle calculations. These calculations do not require any experimental input from the researcher. When empirical models and experimental data are not available, Materials Studio CASTEP is the ideal simulation method for researching problems in solid state physics, materials science, chemistry, and chemical engineering. Researchers can save a significant amount of time and money off the cost of their experiments with the assistance of CASTEP.

It is possible to compute a wide variety of electronic, optical, and physical properties using CASTEP code. To be more specific, it is able to predict the electronic properties such as band gaps, density of states, and Schottky barriers; the optical properties such as reflectivity, absorption, IR spectra, and dielectric functions; or the physical properties such as elastic constants and the like. The Materials Studio CASTEP utilised a method known as total energy plane wave pseudopotential. Effective potentials, which only act on the valence electrons in the system, have been substituted for core electrons in order to simplify the calculation process and cut down on its level of complexity. To calculate the interaction, exchange, and correlation effects of electrons in the system, the electronic wavefunctions were expanded through a plane-wave basis set, and either the local density or generalised gradient approximations were used. Efficiency in optimising the geometric properties of molecules, solids, surfaces, and interfaces is achieved through the application of pseudopotentials and plane wave basis sets [15].

3.3 Simulation method

3.3.1 Building graphene

Building graphene structure in Material Studio was done by initially importing the graphite structure from File≫Import ≫Structures ≫Ceramics ≫graphite.msi. Figure 3.1 shows the imported graphite structure from Material Studio.

Few adjustments on the graphite structure were made in order to transform it into a graphene sheet. To start, we made use of Build≫Symmetry≫Make P1. After that, we removed one of the two layers (the two layers can be seen in Figure 3.1). In this step, the symmetry of these two layers was broken so that we could delete one layer without deleting the other layer; this allowed us to construct a single layer of graphite or graphene. Thereafter, we had to add back the symmetry by utilising: Build≫symmetry≫find Symmetry ≫Impose symmetry

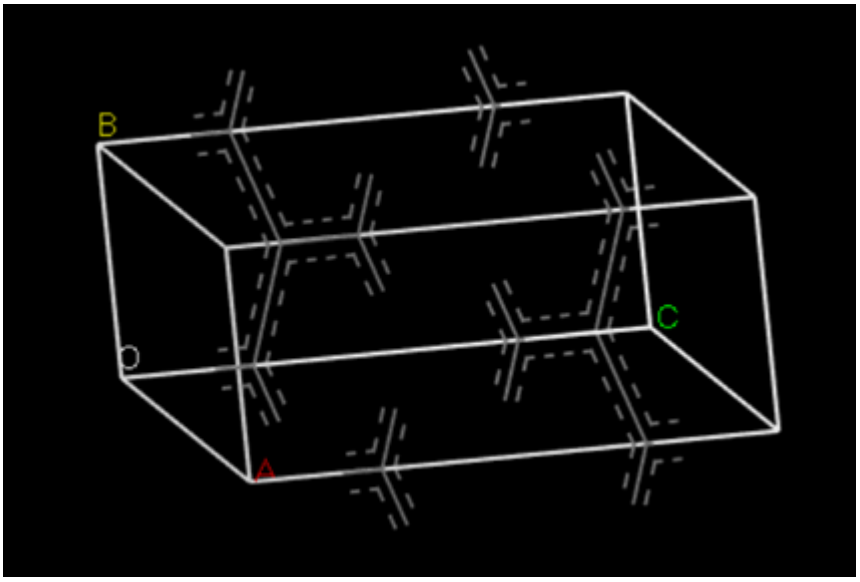

Figure 3.1: Graphite structure

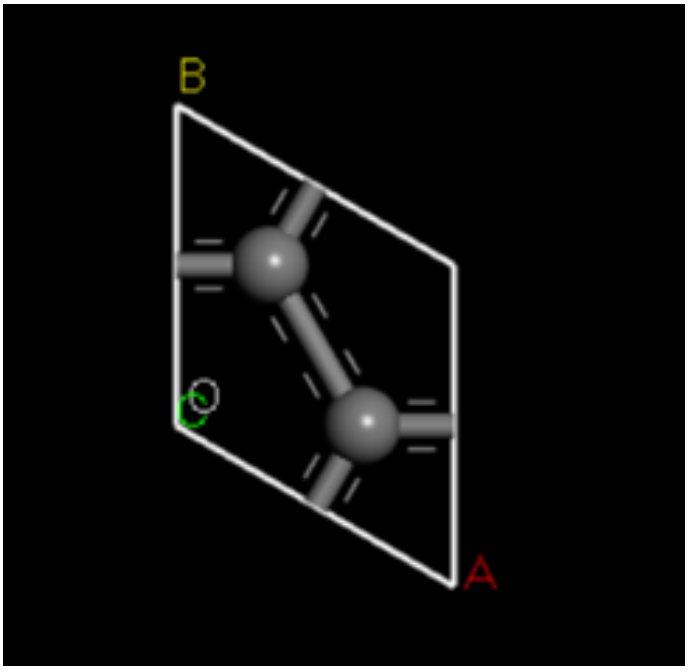

Figure 3.2: A single layer graphene created from graphite.

In order to construct the orthogonal graphene sheet, we first created a 2x2 primitive cell by means of Build≫Symmetry≫Supercell.

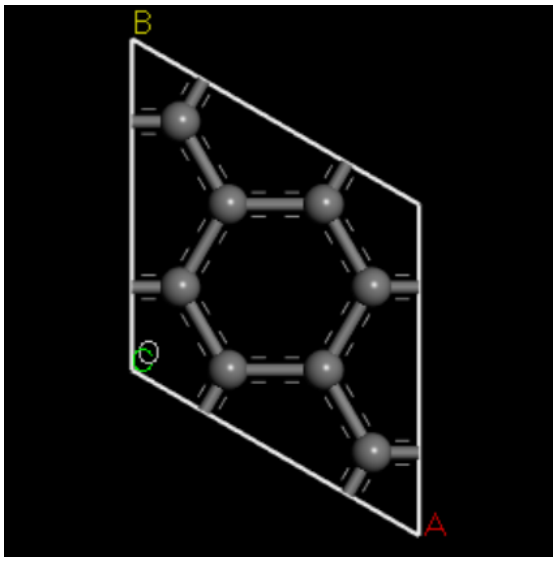

Figure 3.3: A 2x2 orthogonal graphene sheet.

Later, we made the adjustments to the lattice parameters as Build≫Crystals≫Rebuild Crystal≫lattice parameters≫ a = 4.26, b = 2.46, c = 25, $\alpha = \beta = \gamma$ = 90≫ Rebuild

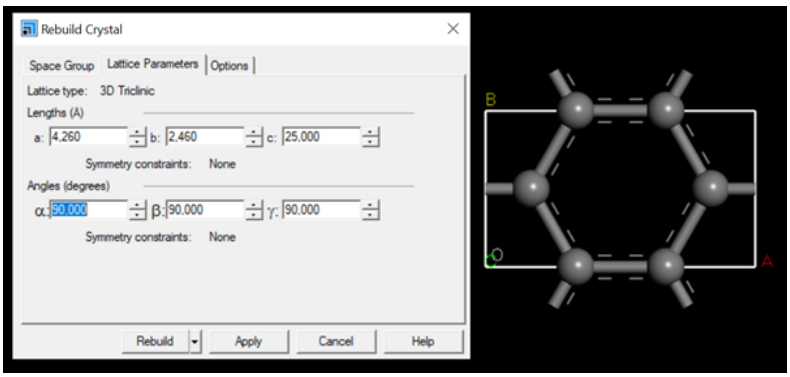

Figure 3.4: Adjustment of graphene lattice parameters.

The computational details on optimizing and calculating the properties are discussed in the next two chapters.

References

[1] R. G. Parr and W. Yang, Density-Functional Theory of Atoms and Molecules, Oxford University Press, New York, 1989.

[2] M. D. Segall, P. J. D. Lindan, M. J. Probert, C. J. Pickard, P. J. Hasnip, S. J. Clark and M. C. Payne, First-principles simulation: ideas, illustrations and the CASTEP code Journal of Physics: Condensed Matter, 14, 2717, 2002.

[3] M. Born and J. R. Oppenheimer, On the quantum theory of molecule, Annalen der Physik, 389 (20), 457, 1927.

[4] D. R Hartree, The wave mechanics of an atom with a non-Coulomb central field. Part I. Theory and methods. In Mathematical Proceedings of the Cambridge Philosophical Society , Cambridge University Press, 24, 89, 1928.

[5] V. Fork, Approximate method for solution of quantum many body problem, Zeitschrift fur Physik, 61 (1), 126, 1930.

[6] R. M. Martin, Electronic Structure: Basic Theory and Practical Methods, Cambridge University Press, 2004.

[7] P. Hohenberg and W. Kohn, Inhomogeneous electron gas, Physical Review, 136(3B), B864, 1964.

[8] W. Kohn and L. J. Sham, Self-consistent equations including exchange and correlation effects, Physical Review, 140(4A), A1133, 1965.

[9] J. P. Perdew, K. Burke, and M. Ernzerhof, Generalized gradient approximation made simple, Physical Review Letters, 77(18), 3865, 1996.

[10] A. D. Becke, Density-functional thermochemistry. III. The role of exact exchange. Journal of Chemical Physics, 98, 5648, 1992.

[11] A. D. Becke, Density-functional exchange-energy approximation with correct asymptotic behaviour, Physical Reviews A, 38, 3098, 1988.

[12] C. Lee, W. Yang and R. G. Parr, development of the Colle-Salvetti correlation-energy formula into a functional of the electron density. Physics Reviews B, CondensedM Matter, 37, 785, 1988.

[13] S. K. Eugene, Density functional theory and molecular interactions: Dispersion interactions, Structural Bond, 150, 65-96, 2013.

[14] S. J. Clark, M. D. Segall, C. J. Pickard, P. J. Hasnip, M. J. Probert, K. Refson, J. R. Yates and M. C. Payne, First principle methods using CASTEP. Zeithchrift fuer Kristallographie, 220, 576, 2005.

[15] Accelrys. CASTEP-DATASHEET. 2014 [cited 2015 April]; Available from: http://accelrys.com/products/datasheets/castep.pdf.

Chapter 4

Electronic and Optical Properties of Graphene Using DFT Calculations

4.1 Introduction

Graphene has sparked great interest in recent decades due to its remarkable electrical and optical capabilities, as demonstrated by a ground-breaking experiment in graphene research in 2004 [1]. Graphene is a honeycomb-shaped 2-dimensional sheet crystalline structure of atomically thick sp^2 hybridized carbon (each carbon fortifies covalently with three other carbon atoms) [2–5]. It serves as a building block for various carbon dimensionalities, such as 0-dimensional buckyball, 1-dimensional nanotube, and 3-dimensional graphite [2]. A pristine graphene has zero band gap because its conduction and valence bands meet at a single location at the Dirac points [6–12]. Graphene is considerably stable due to the tight packing of carbon atoms and hybridization of sp^2, but only when the graphene size is smaller than 20 nm, otherwise it is thermodynamically unstable [13, 14]. The classification of graphene as a metal, non-metal, or semimetal is still up for discussion [13].

The properties of graphene depend on the number of graphene layers. A pristine graphene, for example, has a theoretical surface area of 2630 m^2g^{-1}, which is more than the surface area of carbon nanotubes (100-1000 m^2g^{-1}) [15,

16]. Furthermore, as compared to graphene with a few layers, a single-layer graphene has a higher surface area [14]. According to numerous studies, graphene has a high charge-carrier mobility of 250 000 $cm^2v^{-2}s^{-1}$ at room temperature [5, 17, 18]. Furthermore, each layer of graphene absorbs up to 2.3% of the incident light with a reflectance of less than 0.1% [5]. As a result, it has a very high optical transparency of 97.7% as well as a high degree of flexibility [6, 19]. At room temperature, a single-layer graphene has a high thermal conductivity of 3000-5000 Wm^{-1} K^{-1} [20]. Other properties includes an electrical conductivity of 6000 S cm^{-1} [21] and a Young's modulus of 1.0 TPa [22].

Graphene offers potential application in areas such as high-speed electronics, data storage, liquid crystal display (LCD) smart windows, organic light emitting diode (OLED), supercapacitors, solar cells and electrochemical sensing [19, 23]. The combination of high electrical conductivity, chemical and thermal stability, and outstanding stretchability provides significant benefits for employing graphene as a transparent conductor in organic electronic devices. It is mostly used as a hybrid with other materials to enhance the properties of other materials making them stronger, valuable, and light weight [24,26–28,43]. Studies have shown that the number of graphene layers, defects in graphene layers, various concentrations of graphene and different sizes of graphene have impact on properties of graphene [28–32]. Graphene has been modified in various ways to broaden its application in a variety of fields. One method to modify graphene is to introduce foreign elements into it to tempt its electronic properties. Mukherjee and Kaloni investigated the effect of boron and nitrogen doping on graphene [33]. Their calculations showed that N-doped graphene had a Dirac point shift below the Fermi level and B-doped graphene had a Dirac point shift above the Fermi level, resulting in a band gap opening. The opening of the band gap appears at the Fermi level for co-doped graphene [33]. Sara Varghese *et al.* investigated the structural, energetic, and electronic properties of graphene doped with boron and nitrogen atoms at different doping concentrations [34]. They observed that doping increases the band gap and decreases the energetic stability [34].

Olaniyan *et al.* conducted a systematic study of the stability, electronic, and optical properties of mono- and co-doped graphene with beryllium and nitrogen [35]. Be-N was found to be more stable than Be-doped graphene. The study also shows that when graphene is doped with Be and N, it transforms from being semi-metal to being semi-conductor [35]. Despite the substantial amount of work that has been put into the theory and experimentation of doped graphene, there are still a great many applications that have not been fulfilled. As a result, research into doped graphene systems with superior performance continues to be pushed forward.

4.2 Computational details

Geometry optimizations for the electronic and optical properties were performed by the first principle calculations based on DFT implemented in the Material Studio CASTEP code [36, 37], using the generalised gradient approximation of Perdew-Burke-Ernzerhof (PBE), norm-conserving pseudopotential, periodic boundary conditions and space group of P6/mmm [38]. The k-points mesh was set at $6 \times 6 \times 1$ with a cut-off energy of 350 eV and energy tolerance of 1.0×10^{-6} eV. The force tolerance was set at 0.03 eV, the displacement tolerance 0.0001 Å and convergence threshold of 1.0×10^{-6} eV/atoms.

4.3 Results and Discussion

4.3.1 Structural properties of Graphene Supercells

A graphene unit cell of two carbons was constructed with a 1.42 Å C-C bond lengths, 120° bond angles, and the lattice parameters a = b = 2.46 Å and c = 6.8 Å (see Figure 4.1(a)). The unit cell was then extended to construct $n \times n$ supercells (where n is an integer number). A total of seven graphene supercells were constructed. A 4×4 supercell is shown in Figure 4.1(b). A space group of P6/mmm was used for all the supercells. The constructed supercells are listed in Table 5.1.

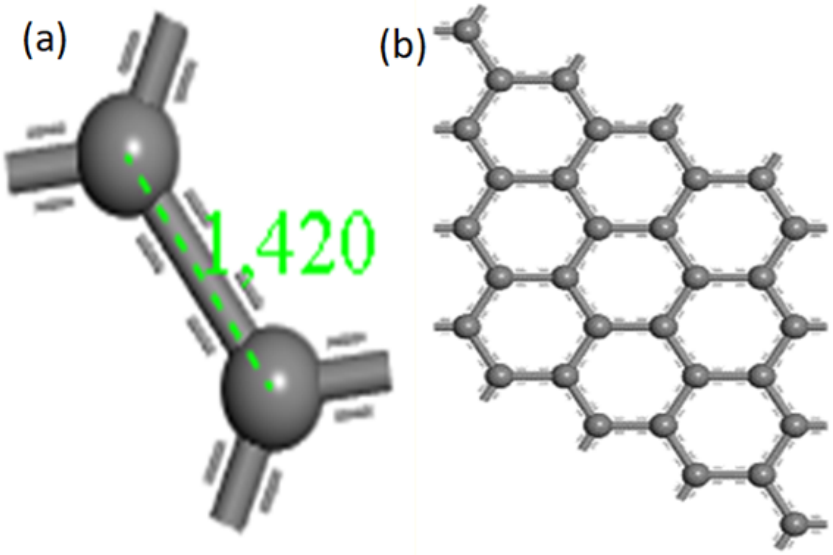

Figure 4.1: A 2-atoms unit cell and 4×4 supercell of graphene.

Table 4.1: Different constructed graphene supercells.

Supercell $(n \times n)$	Number of carbons
Unit cell	2 (C2)
2×2	8 (C8)
3×3	18 (C18)
4×4	32 (C32)
5×5	50 (C50)
6×6	72 (C72)
7×7	98 (C98)

4.3.2 Electronic properties of graphene supercells

Table 1 shows all the possible combinations of $n \times n$ graphene supercells constructed in this work along with the number of carbons of that supercell. We use C# to denote the number of carbons of an $n \times n$ supercell, where # is an integer number representing the number of carbons. The calculated band

structures are shown in Figures 4.2 and 4.3. The Fermi level was set at zero energy (0 eV) and is indicated by the red horizontal dashed lines. The band

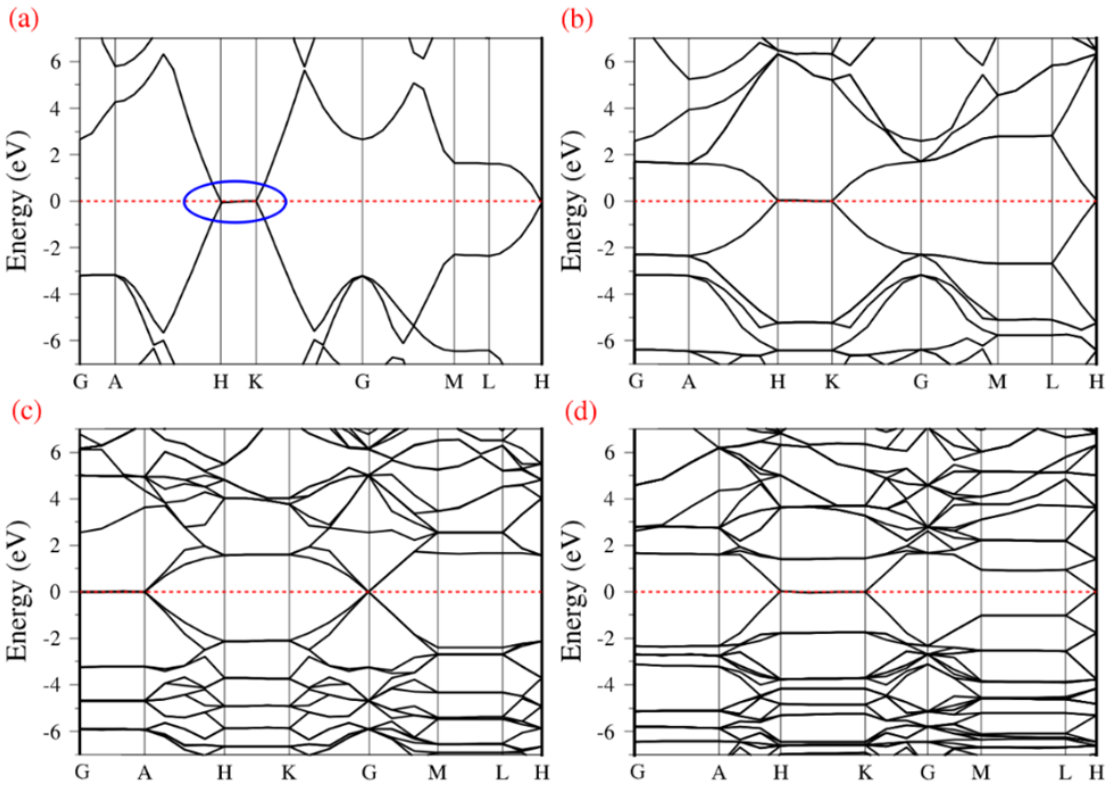

Figure 4.2: Calculated band structures of (a) C2, (b) C8, (c) C18 and (d) C32.

structures of the supercells studied show Fermi levels at the Dirac points, with a zero band gap, which agrees with other literature studies [6-12]. It is observed that the band gap energy of graphene is not affected when the size of the supercells is changed.

To investigate the nature of the states that comprise the conduction and valence band edges, we calculated the contributions of all atomic orbitals in the TDOS and the unique atomic shells in the PDOS band edges. Figures 4.4 and 4.5 show the density of states, which describes the number of states per

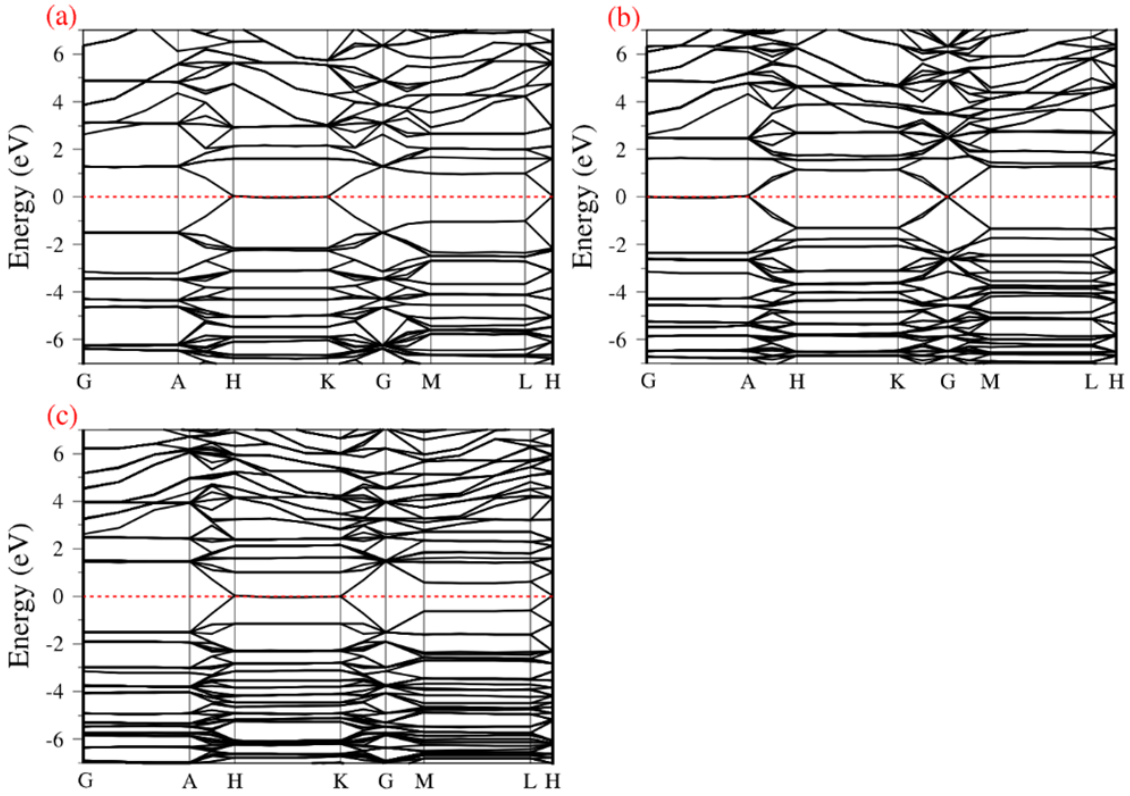

Figure 4.3: Calculated band structures of (a) C50, (b) C72 and (c) C98.

energy interval. The DOS agrees with the calculated band structure. At the Fermi level, the DOS are extremely low, which is consistent with the calculated band structure. It was found that the electron distribution in graphene is due to the contribution of the s and p atomic shells, which are responsible for the energy transfer in graphene. The results show that the s and p states are dominant in both the conduction and valence bands. However, at the Fermi level or near the Fermi level, only the p state is dominant.

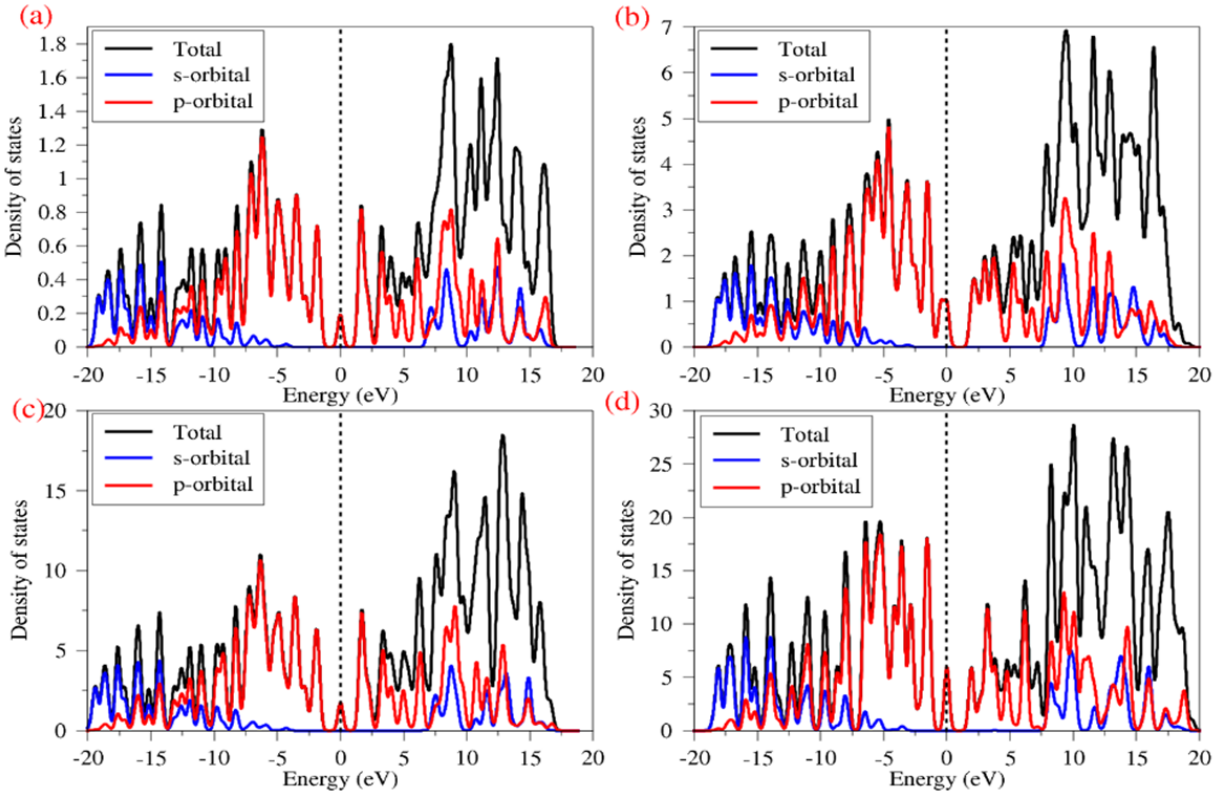

Figure 4.4: TDOS and PDOS for the (a) C2, (b) C8, (c) C18 and (d) C32 graphene supercells.

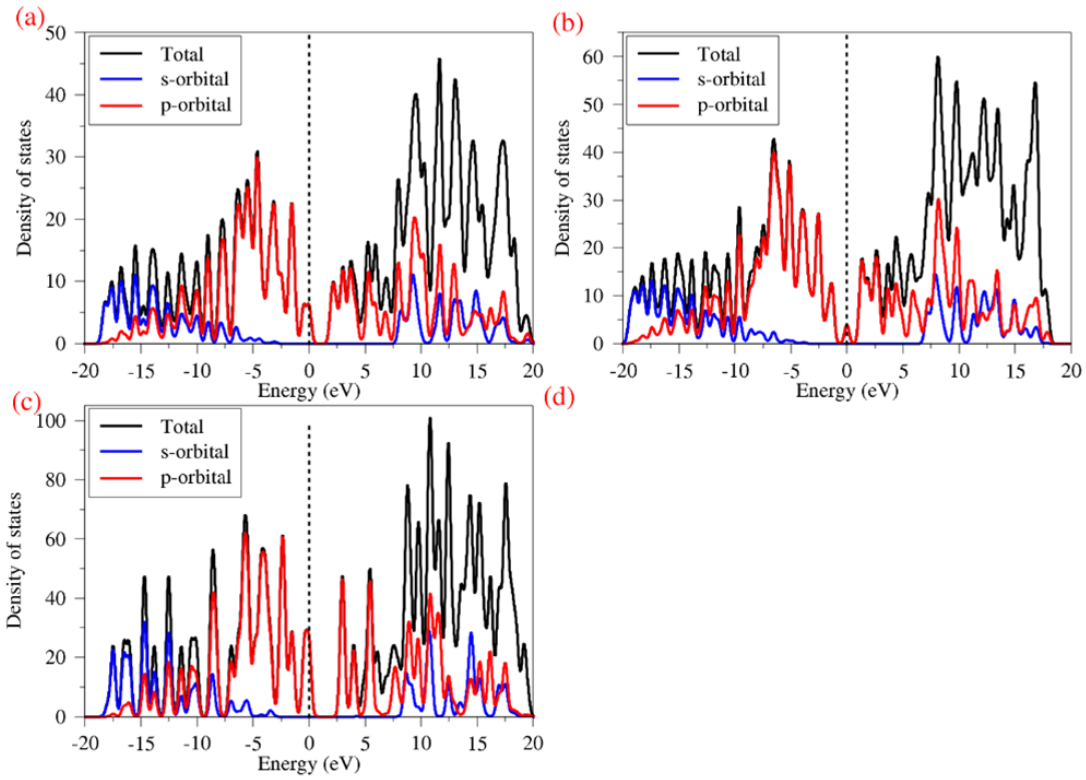

Figure 4.5: TDOS and PDOS for the (a) C50, (b) C72 and (c) C98 graphene supercells.

4.3.3 Optical properties of graphene supercells

To investigate the optical response of graphene, we calculated its absorption, dielectric function, and refractive index. Figure 4.6 illustrates the optical absorption calculations for different supercells. It can be observed that C8, C32, and C50 supercells exhibit strong absorption in the ultraviolet-visible range that extends into the infrared. The C2, C18 supercells absorb more light in the UV area and dissipate in the visible region around the wavelength of 600 nm. C98 enhances the absorption activity to 700 nm, while C72 enhances it to 900 nm.

Dielectric materials tend to become polarized when exposed to an exter-

nal electric field. The term "dielectric function" refers to the property of a substance that determines its polarization. The dielectric function is defined as follows:

$$\varepsilon = \varepsilon_1(\omega) + \varepsilon_2(\omega) \tag{4.1}$$

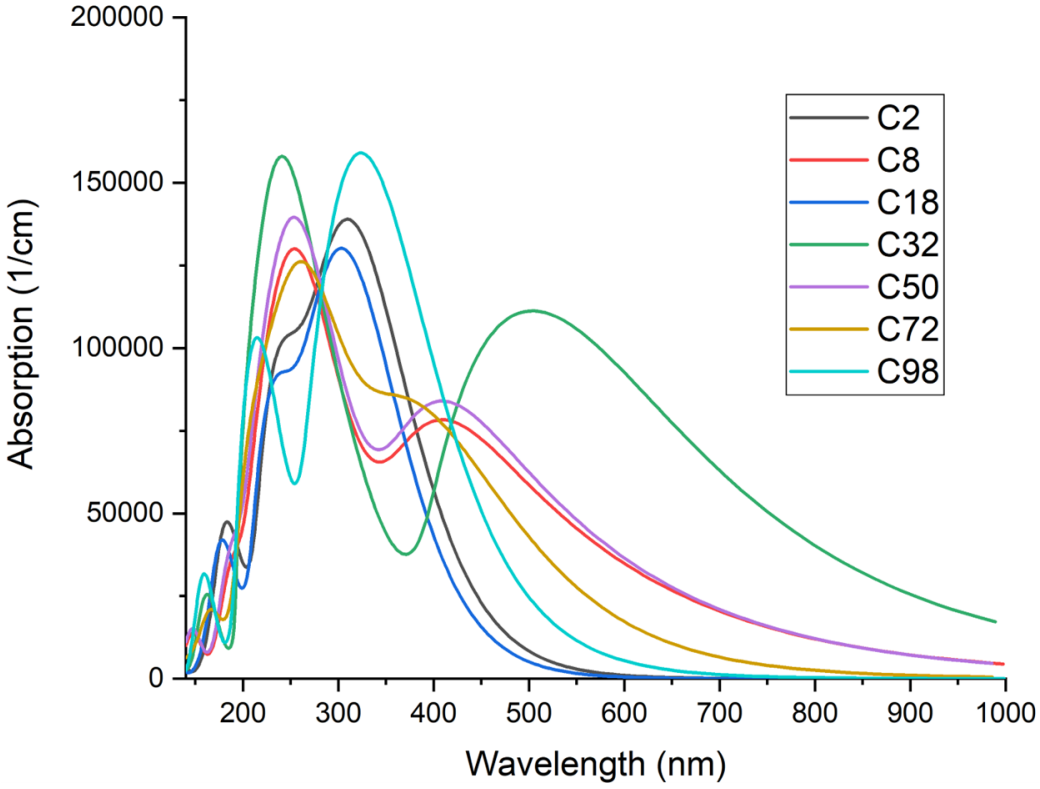

Figure 4.6: Calculated absorption properties of the graphene supercells.

where $\varepsilon_1(\omega)$ and $\varepsilon_2(\omega)$ are the real and imaginary parts of the dielectric function. The real part of the dielectric function is connected to the material's polarization, whereas the imaginary part is related to the electronic absorption. Figure 4.7 shows the calculated dielectric function of the seven graphene supercells up to a photon energy of 10 eV. In the limit of zero photon energy, the findings showed dielectric constant ε_0 values of 4.97, 6.82, 4.23, 11.92, 7. 44, 6.07 and 6. 03 for the supercells C2, C8, C18, C32, C50,

C72 and C98, respectively. The dielectric constant is proportional to the electric displacement, which is proportional to the polarization of the material. The imaginary part of the dielectric function shows that the low-frequency peaks are located at 1.93 to 3.62 eV.

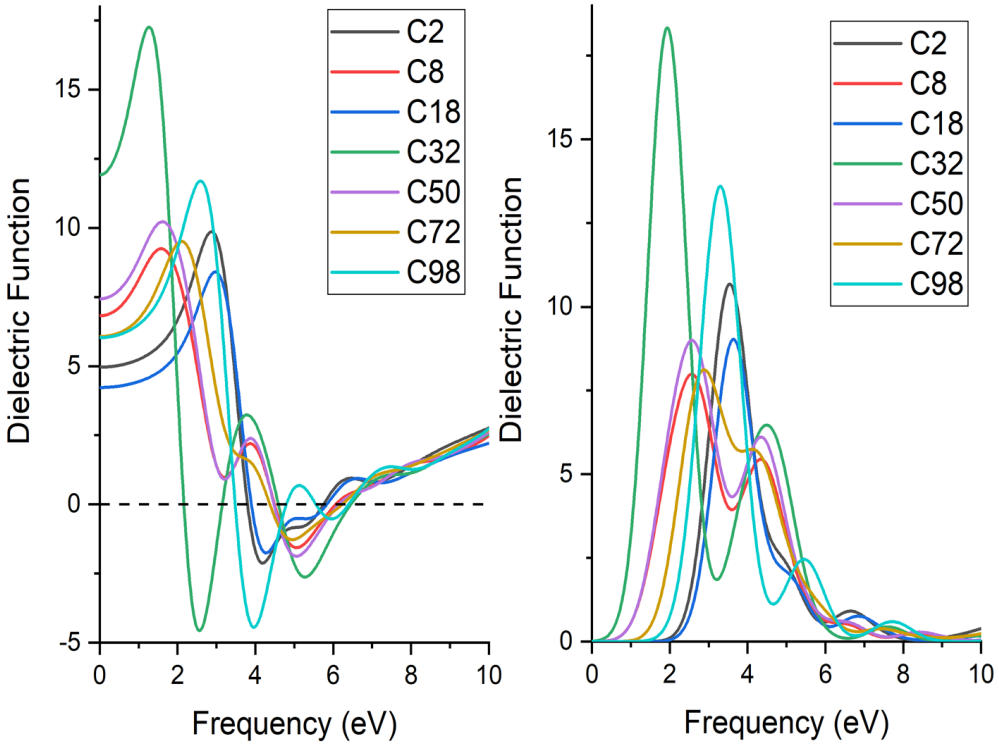

Figure 4.7: Calculated dielectric function properties of the graphene supercells. (a) real dielectric function versus frequesncy, (b) imaginary dielectric function versus frequency.

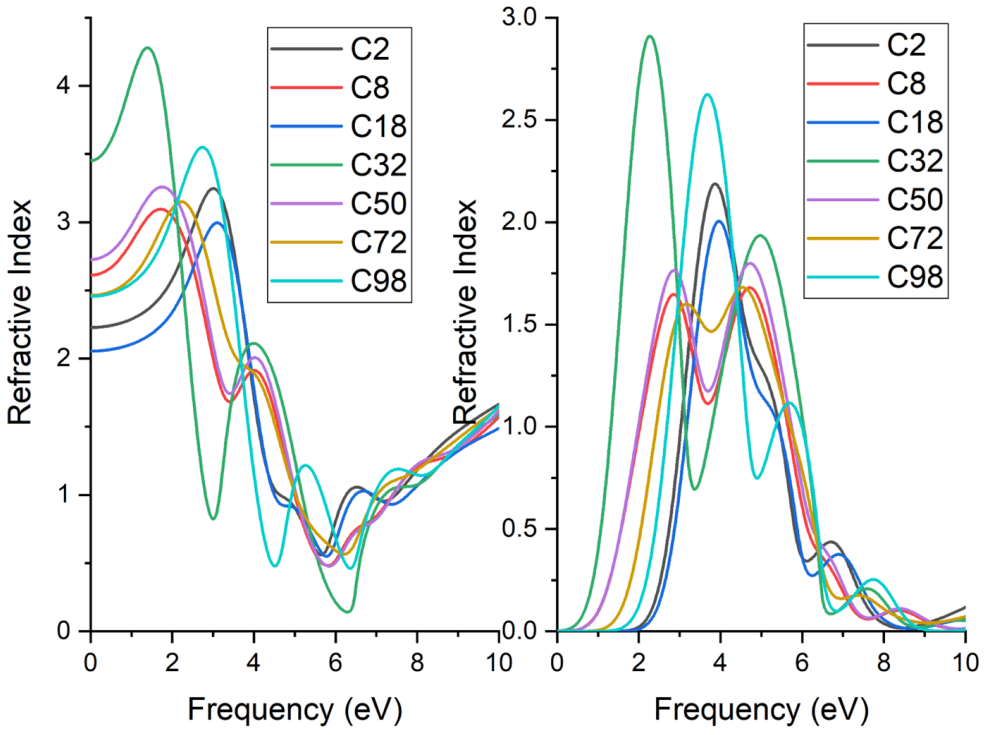

Figure 4.8: Calculated refractive index properties of the graphene supercells.c(a) real extinction coefficient (n) versus frequency, (b) imaginary extinction coefficient (k) versus frequency.

The real part $n(\omega)$ and imaginary part $k(\omega)$ (extinction coefficient) of the refractive index are determined by the dielectric function using the Kramers-Kronig transformation and are defined as

$$n(\omega) = \left(\frac{|\varepsilon(\omega)| + \varepsilon_1(\omega)}{2}\right)^{\frac{1}{2}} \tag{4.2}$$

$$k(\omega) = \left(\frac{|\varepsilon(\omega)| - \varepsilon_1(\omega)}{2}\right)^{\frac{1}{2}} \tag{4.3}$$

The extinction coefficient is relative to the amount of light absorbed. Figure 4.8 shows the calculated refractive index of graphene supercells. The refractive index n_0 is equals to the $\sqrt{\varepsilon_0}$ in the limit of zero photon energy. The findings reveal refractive index n_0 values of 2.23, 2.61, 2.06, 3.45, 2.73, 2.46,

and 2.46 for supercells C2, C8, C18, C32, C50, C72, and C98, respectively. The extinction coefficient has low-frequency peaks located from 2.28 to 3.97 eV.

4.3.4 Electronic properties of doped graphene supercells

According to the findings of research conducted on the optical properties of various graphene supercells in Section 4.3.3, the 4×4 graphene supercell demonstrates a superior optical response compared to other graphene supercells. These results contributed to the decision of considering the 4×4 graphene supercell for doping studies. In this regard, 4×4 graphene supercell was doped with titanium (Ti) and ruthenium (Ru) for further electronic and optical property studies. In the case of mono-doped graphene, the doping was accomplished by exchanging one of the graphene's carbon atoms for either titanium or ruthenium as shown in Figure 4.9(a). On the other hand, in the case of co-doped graphene, two carbon atoms were exchanged for titanium and ruthenium, as illustrated in Figure 4.9(b).

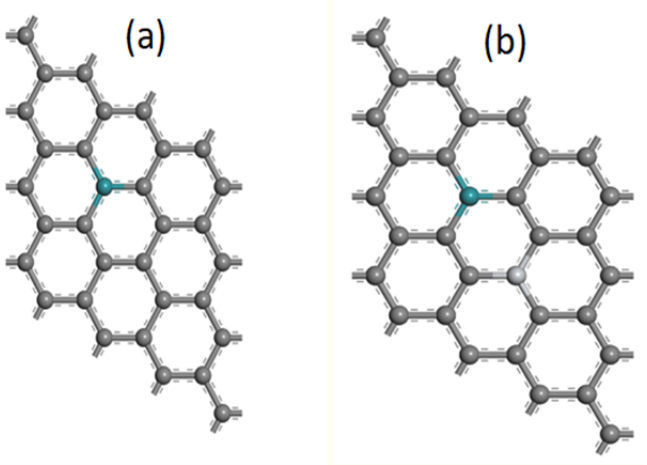

Figure 4.9: Structures of doped graphene: (a) mono-doped and (b) co-doped.

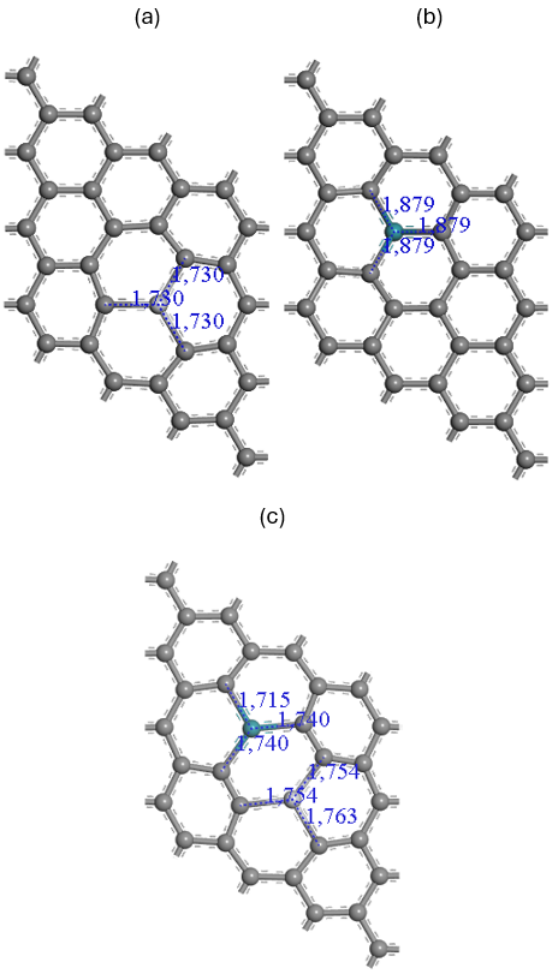

Figure 4.10: Optimized structures of doped graphene: (a) Ti doped, (b) Ru doped, and (c) Ti-Ru co-doped.

It is stated in Section 4.3.1 that the C-C bond is 1.420 Å, now upon doping with Ti and Ru atoms, the C-X (X being either Ti or Ru) bond lengths get modified as shown in Figurev4.10. The calculated C-X bond lengths for Ti and Ru mono-doped graphene are 1.730 and 1.879 Å. The C-X bond lengths for the co-doped optimized structure are 1.715, 1.740, 1.754 and 1.763 Å. The increase in bond lengths is due to the larger radius of Ti and Ru compared to C and this increase suggest greater reactivity in doped graphene.

Figure 4.11 presents an illustration of the band structure that was computed for the doped graphene 4×4 super cell. The results show that doping graphene causes an increase in the band gap, which can be seen near the Fermi level in Figure 4.11. While the energy of the band gap of Ti-doped graphene is 0.555 eV, the energy of the band gap of Ru-doped graphene is 0.786 eV, and the

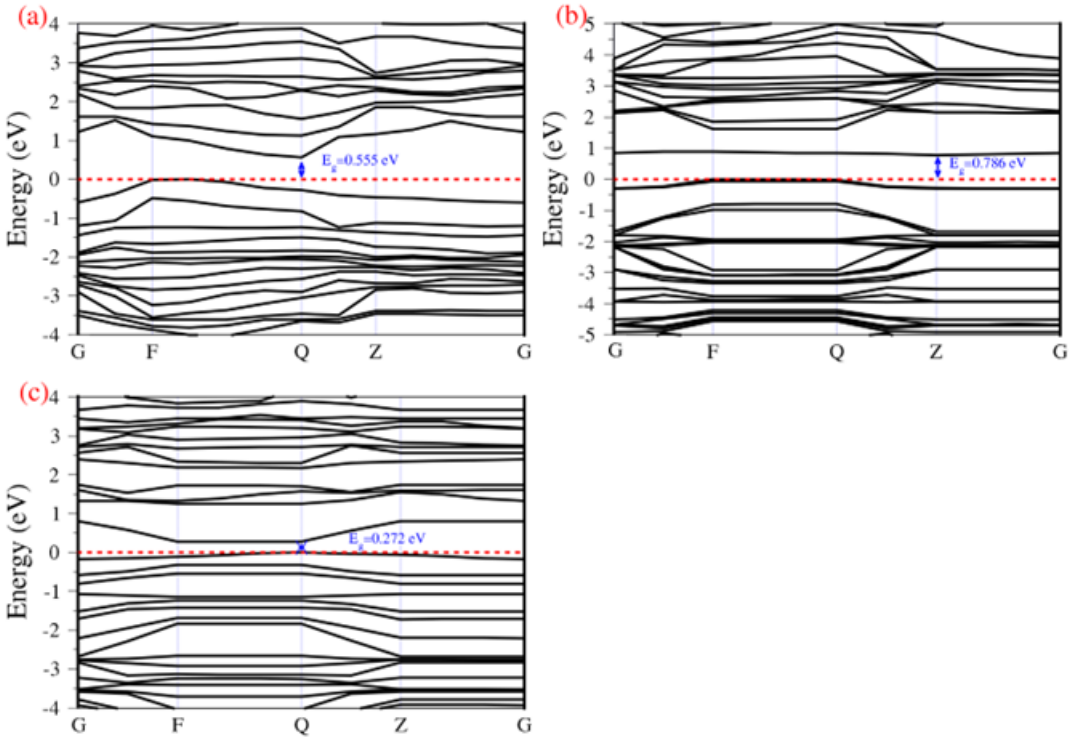

Figure 4.11: Calculated band structures of (a) Ti doped, (b) Ru doped, and (c) Ti and Ru co-doped graphene supercells.

energy of the band gap of co-doped graphene is 0.272 eV. As a result of these properties, graphene can now be categorized as a material that falls into the category of semiconductor. The band structures shown in Figure 4.11 (a) and Figure 4.11 (b) both exhibit an indirect band gap, whereas the

band gap shown in Figure 4.11 (c) exhibits a direct band gap.

Figure 4.12 shows the contribution made by doping graphene to the atomic shells. Doping graphene with the selected elements results in the introduction of numerous minor state density peaks, which can be clearly seen in the Fermi level region, as shown in Figure 4.12. This can be clearly observed by comparing Figure 4.12 with the density of states of the 4x4 graphene supercell shown in Figure 4.4(d). Ru is a transition metal having a 4d electron configuration, whereas Ti has a 3d electron configuration. The 3d contribution from Ti is highlighted by the cyan color in Figure 4.12 (a), and the 4d contribution from Ru is highlighted by the cyan color in Figure 4.12 (b). Both of these contributions are in the energy range of -6 eV to 6 eV. In the vicinity of the Fermi level, the 3d state density has a modest peak, whereas the 4d state density has obvious peaks.

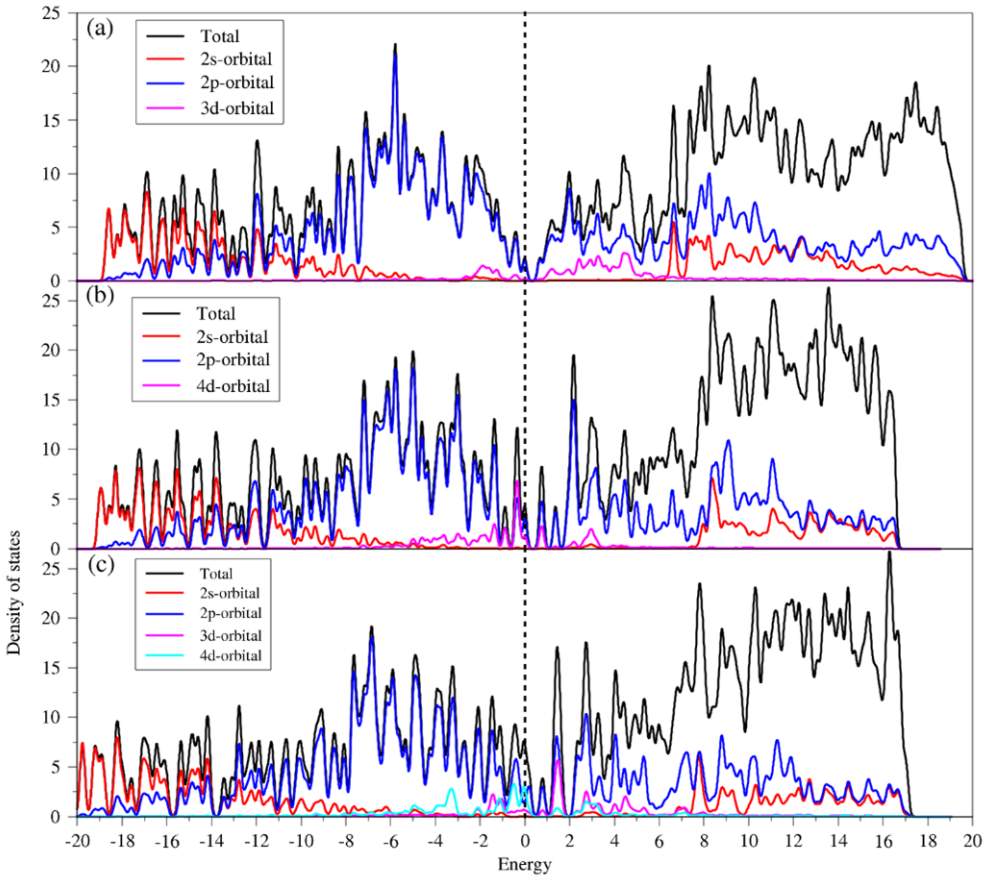

Figure 4.12: TDOS and PDOS of the (a) Ti doped, (b) Ru doped, and (c) Ti and Ru co-doped graphene supercells.

4.3.5 Optical absorption of mono and co-doped graphene supercells

The calculated results of the optical absorbance of the doped graphene are illustrated in Figure 4.13. When Ti and Ru are added to graphene, the results reveal a blue shift in the visible region of the absorption spectra. The blue shif is seen for both mono-doped and co-doped graphene. This results agree with the previous result by Abdelazeez *et al.* where their study reveals that that the absorption wavelength of Si and Si-P co-doped graphene systems had a greater shift to a lower range compared to pristine graphene [39].

Ru-doped graphene exhibits the smallest light absorption coefficient among others. Because of the dopants that were introduced into graphene, there is a red shift that occurs in the infrared region, which is located above 800 nm.

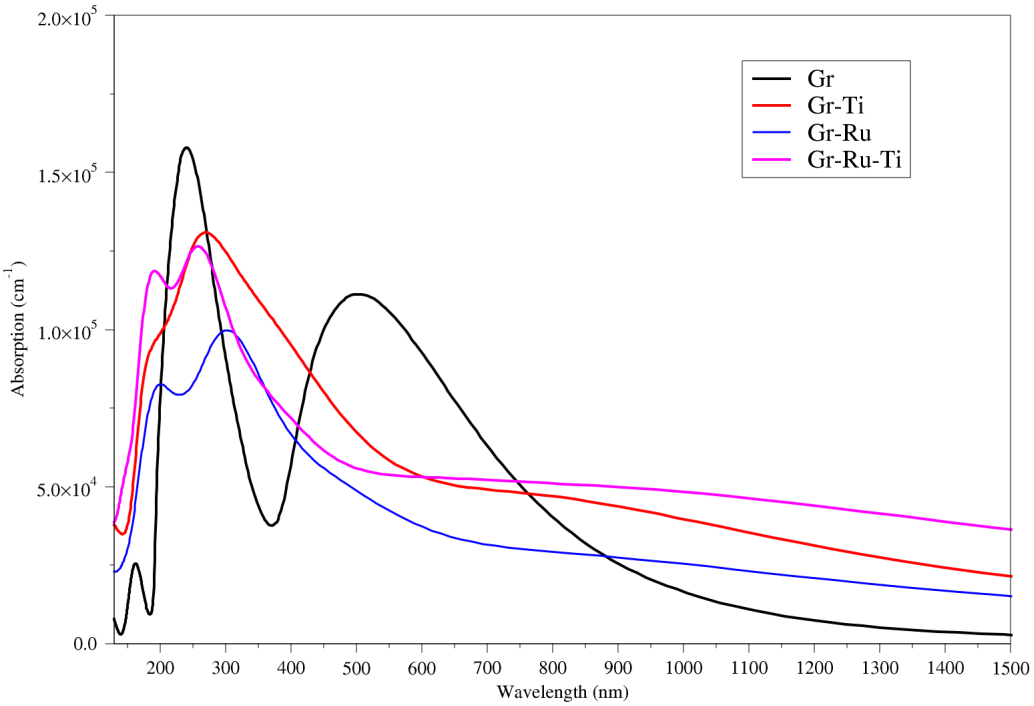

Figure 4.13: Calculated absorption properties for pristine and doped graphene.

4.4 Conclusion

Geometry optimizations for the electronic and optical properties were performed by first-principles calculations based on density functional theory. Various supercells of graphene were modeled and optimized, and their properties were calculated. The results show that different graphene supercells

have different electronic and optical properties. On doping graphene, the calculations show an increase in C-X bond length. The increased bond lengths induce greater reactivity in graphene, which can be used for various future applications. The energy bandgap of pure graphene is zero, and after doping with Ti and Ru it increases to 0.550 eV, and 0.786 eV, respectively. The co-doped graphene bandgap is 0.272 eV. The calculated optical properties showed that doping graphene with Ti and Ru shifts the absorption from the visible to the near-infrared region, and these results open possibilities of using doped graphene as a semiconductor material.

References

[1] K. S. Novoselov, A. K. Geim, S. V. Morozov, .D Jiang, Y. Zhang, S. V. Dubonos, I. V. Grigorieva and A. A Firsov, Electric field effect in atomically thin carbon films, Science, 306, 666, 2004.

[2] A. K. Geim and K. S. Novoselov, The rise of graphene, Nature Materials, 6, 183, 2007.

[3] C. N. Rao, A. K. Sood, K. S. Subrahmanyam and A. Govindaraj, Graphene: The new two-dimensional nanomaterial, Angewandte Chemie International Edition, 48, 7752, 2009.

[4] M. J. Allen, V. C. Tung and R. B. Kaner, Honeycomb carbon: a review of graphene, Chemical Review, 110, 132, 2009.

[5] C. Soldano, A. Mahmood and E. Dujardin, Production, properties and potential of graphene, Carbon, 48, 2127, 2010.

[6] R. Nair, P. Blake, A. Grigorenko, K. Novoselov, T. Booth, T. Stauber, N. Peres and A. Gein, Fine structure constant defines visual transparency of graphene, Science, 320, 1308, 2008.

[7] S. K. Tiwari, V. Kumar, A. Huczko, R. Oraon, A. D. Adhikari and G. Nayak, Magical allotropes of carbon: prospects and applications, Critical Reviews in Solid State and Materials Sciences, 41(4), 257, 2016.

[8] C. K Chua and M. Pumera, Chemical reduction of graphene oxide: a synthetic chemistry viewpoint, Chemical Society Reviews, 43(1), 291, 2014.

[9] Y. Su, V. Kravets, S. Wong, J. Waters, A. Geim and R. Nair, Impermeable barrier films and protective coating based on reduced graphene oxide, Nature Communications, 5, 4843, 2014.

[10] S. Y. Toh, K. S. Loh, S. K. Kamarudin and W. R. W. Daud, Graphene production via electrochemical reduction of graphene oxide: synthesis and characterisation, Chemical Engineering Journal, 251, 422, 2014.

[11] J. Poon, C. Batchelor-McAuley, K. Tschulic and R. G. Compton, Single graphene nanoplacelets: capacitance, potential of zero charge and diffusion coefficient, Chemical Science, 6(5), 2869, 2015.

[12] M. Bacon, S. J. Bradley and T. Nann, Graphene quantum dots, Particle and Particle Systems Charactierization, 31(4), 415, 2014.

[13] S. K. Tiwari, R. K. Mishra, S. K. Ha and A. Huczko, Evolution of graphene oxide and graphene: From imagination to industrialisation, Chemistry of Nanomaterials, 4(7), 598, 2018.

[14] S. K. Tiwari, S. Sahoo, N. Wang and A. Huczko, Graphene research and their outputs: Status and prospect, Journal of Science: Advanced Materials and Devices, 5, 10-29, 2020.

[15] Y. Zhu, S. Murali, W. Cai, X. Li, J. W Suk, J. R. Potts and R. S. Ruof, Graphene and graphene oxide: Synthesis, properties and applications, Advanced Materials, 22, 3906, 2010.

[16] C. M. Weber, D. M. Eisele, J. P. Rabe, Y. Liang, X. Feng, L. Zhi, K. Müllen, J. L. Lyon, R. Williams, D. V. A. Bout and K. J. Stevenson, Graphene-based optically transparent electrodes for spectroelectrochemistry in the UV-Vis region, Small, 6, 184, 2010.

[17] M. Ortila, C. Faugeras, P. Plochocka, P. Neugebauer, G. Martinez, D. K. Maude, A. L. Barra, M. Sprinkle, C. Berger, W. A. De Heer and M. Potemski, Approaching the Dirac point in high mobility multilayer epitaxial graphene, Physical Review Letters, 101, 267601, 2008.

[18] L. Liao, H. Peng and Z. Liu, Chemistry makes graphene beyond graphene, Journal of the American Chemical Society, 136(35), 12194, 2014.

[19] S. Pang, Y. Hernandez, X. Feng and K. Müllen, Graphene as transparent electrode material for organic electronics, Advanced Materials, 23, 2779, 2011.

[20] A. A. Balandin, S. Ghosh, W. Bao, I. Calizo, D. Teweldebrhan, F. Miao and C. N. Lau, Superior thermal conductivity of single-layer graphene, Nano Letters, 8, 902, 2008.

[21] X. Du, I. Skachko, A. Barker and E. Y Andrei, Approaching ballistic transport in suspended graphene, Nature Nanotechonology, 3, 491, 2008.

[22] C. Lee, X. Wei, J. W. Kysar and J. Hone, Measurements of the elastic properties and intrinsic strength of monolayer graphene, Science, 321, 385, 2008.

[23] E. P. Randviir, D. A. C. Brownson and C. E. Banks, A decade of graphene research: production, applications and outlook, Materials Today, 17(9), 426, 2014.

[24] P. K. Dubey, P. Tripathi, R. S. Tiwari, A. S. K. Sinha and O. N. Srivastava, Synthesis of reduced graphene oxide-TiO_2 nanoparticle composite systems and its application in hydrogen production, International Journal of Hydrogen Energy, 39, 16282, 2014.

[25] P. Xu, Q. Tang and Z. Zhou, Structural and electronic properties of graphene-ZnO interfaces: dispersion-corrected density functional theory investigations, Nanotechnology, 24, 305401, 2013.

[26] P. M. Martins, C. G. Ferreira, A. R. Silva, B. Magalhaes, M. M. Alves, L. Pereira, P. A. A. P. Marques, M. Melle-Franco and S. Lanceros-Méndez, TiO_2/graphene and TiO_2/graphene oxide nanocomposites for photocatalytic applications: A computer modelling and experimental study, Composites Part B: Engineering, 145, 39, 2018.

[27] X. An and J. C. Yu, Graphene-based photocatalytic composites, RSC Advances, 1, 1426, 2011.

[28] X. Fang, M. Li, K. Guo, X. Liu, Y. Zhu, B. Sebo and X. Zhao, Graphene-compositing optimization of the properties of dye-sensitized solar cells, Solar Energy, 101, 176, 2014.

[29] A. C. Ferrari, J. C. Meyer, V. Scardaci, C. Casiraghi, M. Lazzeri, F. Mauri, S. Piscanec, D. Jiang, K. S. Novoselov, S. Roth and A. K. Geim, Raman Spectrum of Graphene and Graphene Layers, Physical Review Letters, 97, 187401, 2006.

[30] J. Nilsson, A. H. C. Neto, F. Guinea and N. M. R. Peres, Electronic properties of graphene multilayers, Physical Review Letters, 97(26), 266801, 2006.

[31] X. Li, L. Tao, Z. Chen, H. Fang, X. Li, X. Wang, J. Xu and H. Zhu, Graphene and related two dimensional materials: Structure-property relationships for electronics and optoelectronics, Applied Physics Reviews, 4, 021306, 2017.

[32] J. Fan, S. Liu and J. Yu, Enhanced photovoltaic performance of dye-sensitized solar cells based on TiO2 nanosheets/graphene composite films, Journal of Materials Chemistry, 22, 17027, 2012.

[33] S. Mukherjee and T.P. Kaloni, Electronic properties of boron- and nitrogen-doped graphene: a first principles study, Journal of Nanoparticle Research, 14, 1059, 2012.

[34] S. S. Varghese, S. Swaminathan, K. K. Singh and V. Mittal, Energetic stabilities, structural and electronic properties of monolayer fraphene doped with boron and nitrogen atoms. Electronics, 5, 91, 2016.

[35] O. Olaniyan, R. E. Maphasha, M. J. Madito, A. A. Khaleed, E. Igumbor and M. Manyala, A systematic study of the stability, electronic and optical properties of beryllium and nitrogen co-doped graphene, Carbon, 129, 207, 2018.

[36] G. Kresse and J. Furthmuller, Efficiency of ab-initio total energy calculations for metals and semiconductors using a plane-wave basis set, Computational Materials Science, 6, 15, 1996.

[37] G. Kresse and J. Furthmuller, Efficient iterative schemes for ab initio total-energy calculations using a plane-wave basis set, Physical Review B, 54 11169, 1996.

[38] J. P. Perdew, K. Burke and M. Ernzerhof, Generalized gradient approximation made simple, Physical Review Letters, 77, 3865, 1996.

[39] A. A. Abdelazeez, A. B. Trabelsi, F. H. Alkallas, S. AlFaify, M. Shkir, T. A. Alrebdi, K. S. Almugren, F. V. Kusmatsev and M. Rabia, Tuning the Structural, Electronic, and Optical Properties of Monolayer Graphene through Heteroatom Doping: A First-Principles Study with Future Light Sensing Applications, Photonics, 10, 838, 2023.

Chapter 5

DFT Calculations of Brookite TiO_2/graphene Hybrid Materials for Dye Sensitized Solar Cells Application

5.1 Introduction

The continuous reliance on fossil fuels has been much of a global concern in the recent past, particularly with issues concerning global warming and carbon dioxide emissions. These concerns have led researchers searching for alternative sources of energy that are renewable and environmentally friendly. The current global market of renewable energy is dominated by the first-generation solar cells commonly known as silicon solar cells. However, the excessive cost of silicon solar cells remains a challenge, hence a concerted effort on improving the efficiency of newer low-cost alternatives such as dye sensitized solar cells (DSSCs) and perovskites solar cells [1-4]. Despite the low cost, the DSSCs still suffer a low efficiency that is measured to be approximately 12% [5, 6]. One of the key areas in the optimisation of DSSCs is the preparation of the TiO_2 semiconductor, since it has a major impact on dye molecules, transfer of electrons and separation of charge carriers [7].

Experimental and computational studies have shown that TiO_2 is a good

material for solar cells and photocatalytic applications [5]. However, the TiO_2 polymorphs have limited absorption edges in the visible region due to the wide band gap of the polymorphs [8]. The most common polymorphs of TiO_2 are the rutile, anatase and brookite with the band gaps of 3.0, 3.2, and 3.4 eV, respectively [8, 9]. A number of band gap modification techniques such as elemental doping [10-15], semiconductor composite formation [16, 17], quantum dot sensitization [18, 19] and structural modification [20-22] have been shown to be effective in improving the absorption of TiO_2 in the range covering the ultraviolet (UV) to visible light wavelength. Several doping schemes have been proposed, including transition metal doping and non-metal doping; and a combination of the two schemes to reduce the recombination rate of photo-generated carriers.

Based on the preceding chapter, graphene has already demonstrated that it is a one-of-a-kind material that possesses the potential for a wide variety of uses. Recent experimental work has demonstrated that photocatalytic TiO_2 nanoclusters can interact with graphene in a number of diverse ways. According to these findings, the catalytic characteristics of the graphene/TiO_2 material are much superior to those of pure TiO_2 nanoclusters. According to one theory, graphene makes it possible for electrons and holes in photoexcited TiO_2 to go through the graphene sheet, which helps to reduce the amount of recombination that occurs between the electrons and holes. At this point, there is a lack of a solid understanding regarding the specific effects that graphene has on brookite TiO_2. Recent studies have been conducted on oxidized graphene sheets, which are a byproduct of graphene synthesis and an intermediary step in the process. It has also been demonstrated that these sheets interact with TiO_2 to influence the photocatalytic capabilities of the latter. This chapter used density functional theory for better understanding of the reasons why graphene has been found to improve the photo catalytic capabilities of TiO_2 (brookite in this case), as well as the ways in which these features can be better leveraged to further improve their performance.

5.2 Computational details

All the calculations were performed using Material Studio of BIOVIA. The surface structure of brookite (210) was created by cleaving the optimized brookite bulk structure. The geometry optimizations for the electronic and optical properties were performed using first principles calculations based on DFT implemented in the CASTEP code [23, 24], using the generalized gradient approximation of Perdew-Burke-Ernzerhof with ultrasoft pseudopotential [25]. The electron wave functions were expanded on a plane-waves basis with the cut-off energy set up of 620 eV for brookite bulk structure, and brookite (210) surfaces. The Monkhorst-Pack scheme k-point grid sampling of the Brillouin zone was set at $3 \times 5 \times 5$ for brookite bulk structure and $1 \times 4 \times 5$ for the surfaces.

5.3 Results and Discussion

5.3.1 Structural properties

Figure 5.1 shows the optimised brookite TiO_2 bulk structure containing eight titanium and sixteen oxygen atoms. The lattice parameters of the optimized structure are listed in Table 5.1 and are compared to the experimental and previous theoretical results. The calculated lattice parameters are consistent with the experimental and theoretical literature results within percentage errors of 0.196, 0.202 and 0.195% for a, b, and c lattice parameters, respectively. Gong and Selloni conducted a first principle calculations of various brookite surfaces and found that while the brookite TiO_2 (210) surface's structure is similar to that of the most stable anatase TiO_2 (101) surface, the former has a higher degree of chemical reactivity [26]. This led to the selection of the brookite TiO_2 (210) surface for this study. The brookite TiO_2 (210) surface is shown in Figure 5.2. Figures 5.3 and 5.4 show the top and side view of TiO_2/graphene structure, respectively. Having the 4×4 graphene supercell as the optimum graphene supercell from Chapter 4, it was selected and incorporated on brookite TiO_2 (210) surface.

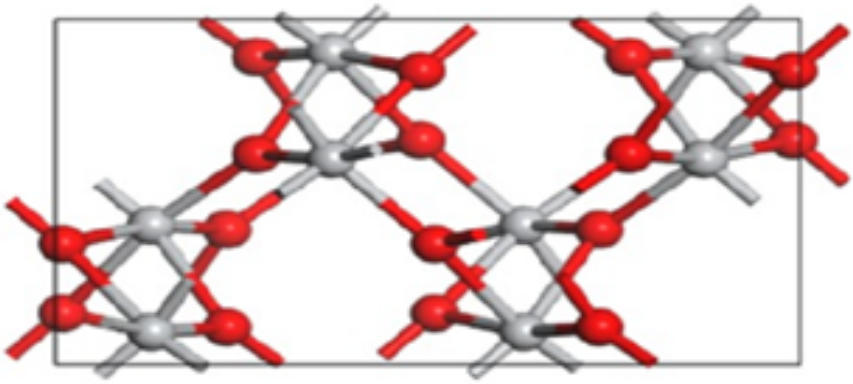

Figure 5.1: Theoretical model of TiO_2 brookite bulk structure.

Table 5.1: Calculated lattice parameters of brookite TiO_2 compared with experiments [27] and other calculations [28].

Parameters	This work	Experimental [27]	Literature [28]
a (Å)	9.166	9.184	9.157
b (Å)	5.436	5.447	5.430
c (Å)	5.135	5.145	5.122

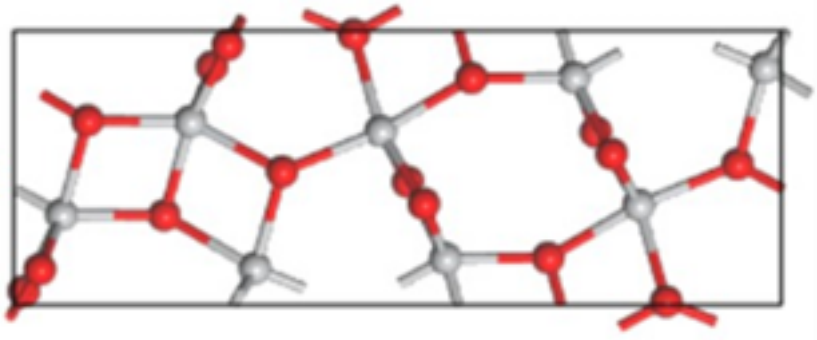

Figure 5.2: Theoretical model of TiO_2 brookite (210) surface structure.

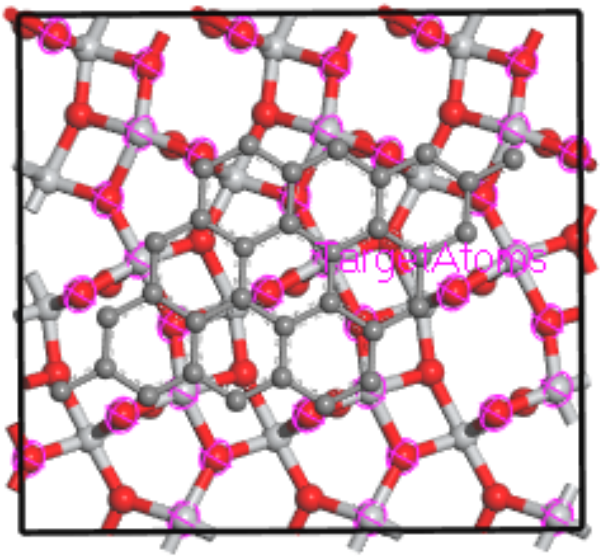

Figure 5.3: Top view theoretical model of brookite TiO_2/graphene interface.

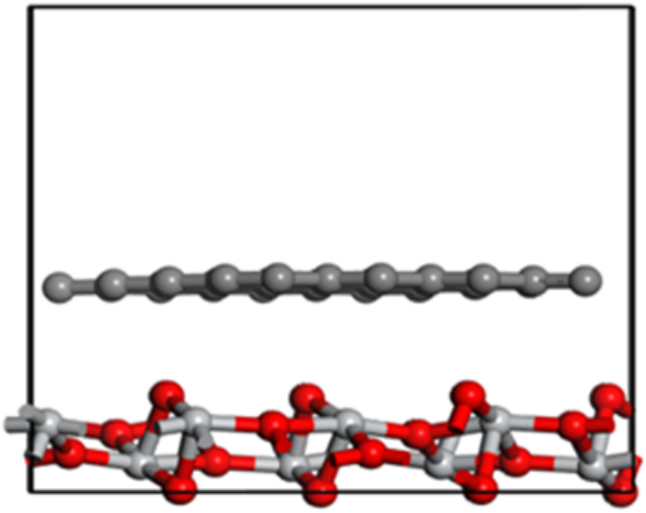

Figure 5.4: view theoretical model of brookite TiO_2/graphene interface.

5.3.2 Electronic properties

Figure 5.5 shows the band structures of pure brookite TiO_2 structure. The calculated band gap energy in this study is 2.358 eV. This is lower than the experimentally obtained value of 3.400 eV, yet comparable with other GGA calculated value of 2.485 eV [29]. Such a disparity in experiments and calculations is always expected since it is in the GGA's nature to underestimate the value of the energy gap in semiconductors [30]. To compensate for the underestimation of the band gap, the scissor operation of 1.042 eV was used in this study. The scissors scheme aligns the theoretical valence band energy (VBE) and conduction band energy (CBE) with the experimental equivalents by stretching the theoretical gap states over the experimental gap using a "scissors" process.

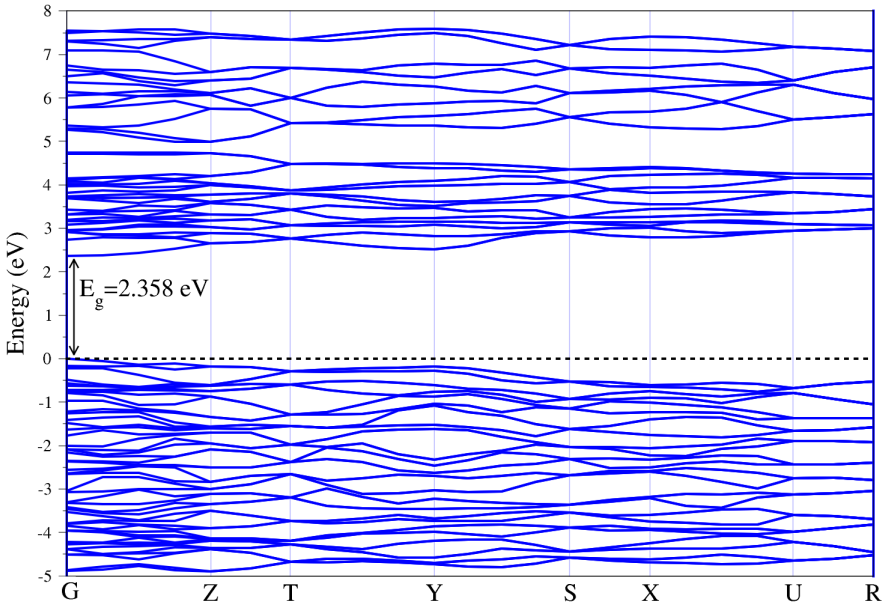

Figure 5.5: Energy band structures of pure brookite TiO_2 bulk.

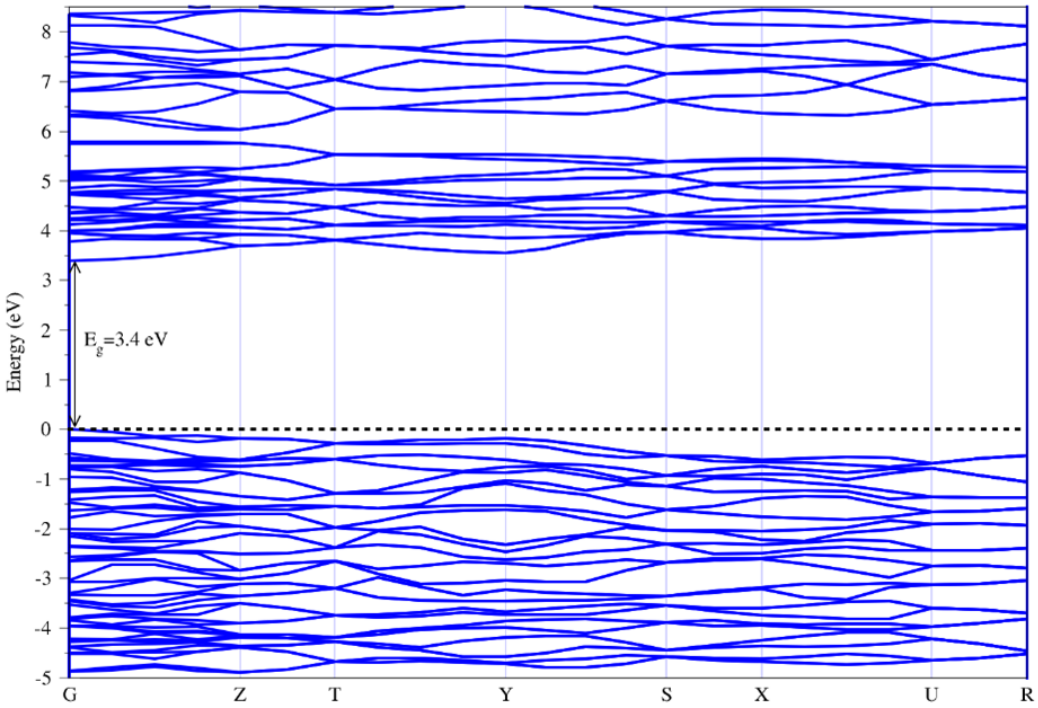

Figure 5.6: Energy band structures of pure brookite TiO_2 bulk with scissor scheme.

The band gap value after the scissor operation is 3.4 eV, as shown in Figure 5.6. Additionally, the conduction band minimum (CBM) and valence band maximum (VBM) are observed to be both located at G; this shows that pure brookite TiO_2 can be regarded as a direct band gap semiconductor.

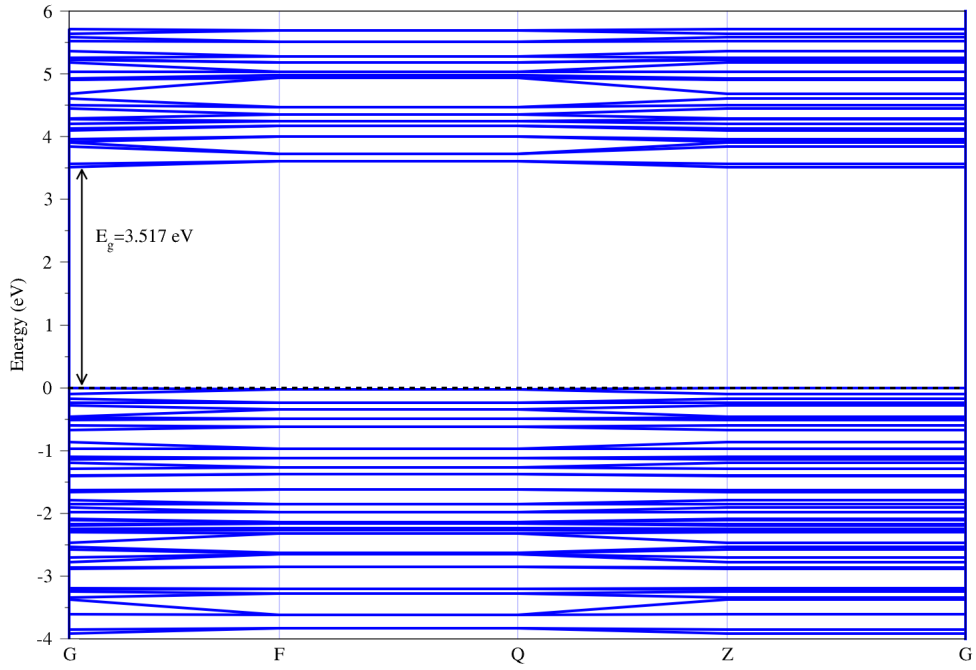

Figure 5.7: Energy band structures of 1x1 brookite TiO_2 (210) surface.

Before creating the supercell structure, brookite TiO_2 (210) surface produced a band gap value of 3.517 eV as shown in Figure 5.7. Creating a supercell had the impact of altering the band structure of the brookite value of (210) surface, as evidenced by the calculations which demonstrate a narrowing of the band gap of the 3x1 supercell surface to 3.297 eV as shown in Figure 5.8.

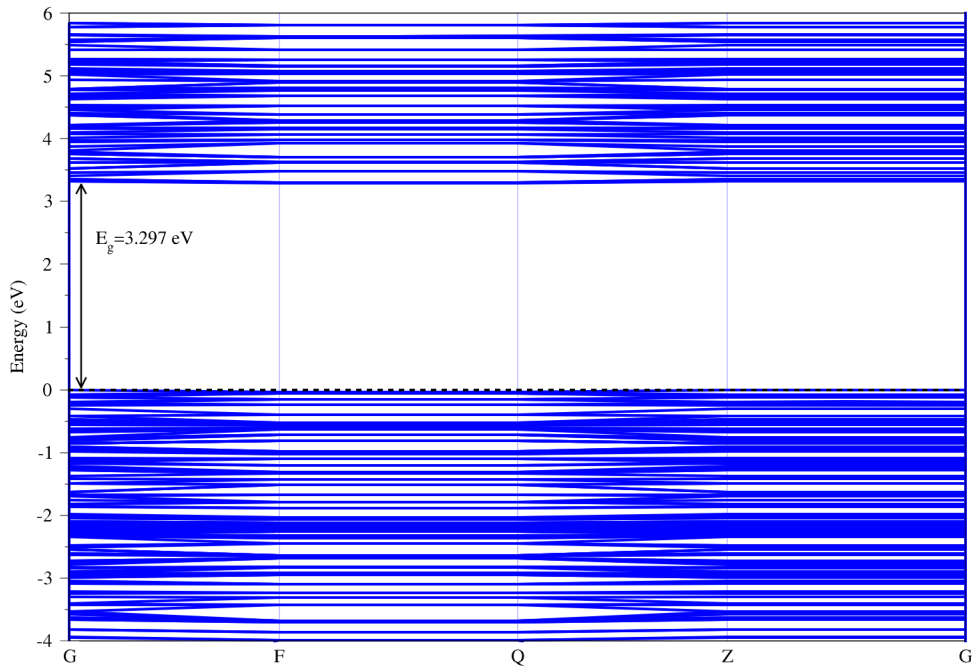

Figure 5.8: Energy band structures of 3x1 brookite TiO_2 (210) surface.

Figure 5.9 shows the band structure of the brookite TiO_2/graphene hybrid system. The calculated energy gap of this brookite TiO_2/graphene system is 1.091 eV. These findings demonstrate that new energy levels have been generated, such can be traced at the top of the valence band and at the bottom of the conduction band. These new energy levels make it simpler for electrons transition from the valence band to the conduction band.

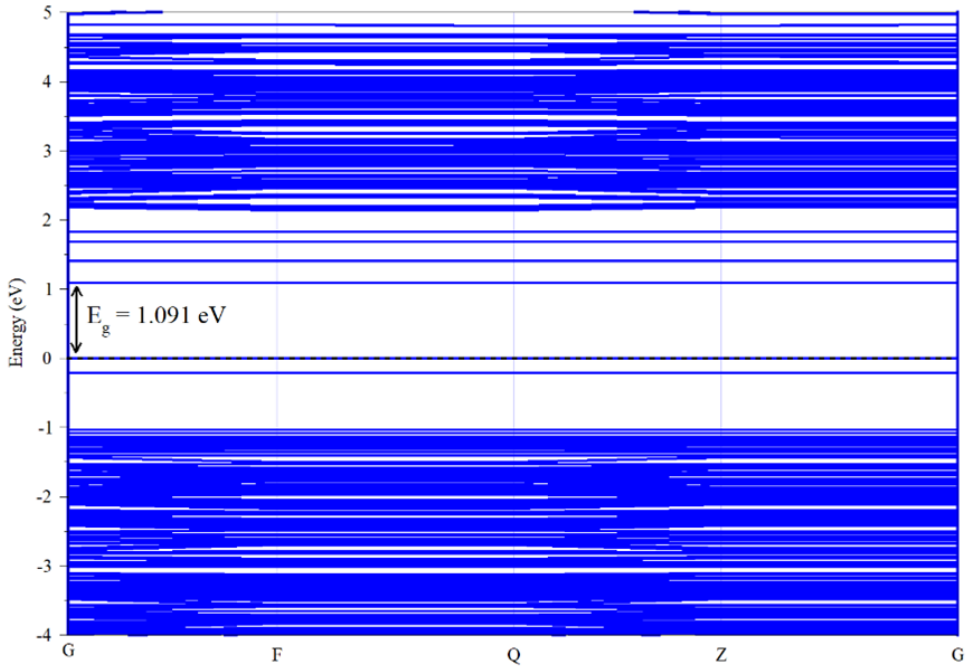

Figure 5.9: Energy band structure of graphene/TiO_2.

Calculating the total density of states (TDOS) and the partial density of states (PDOS) allows researchers to investigate the nature of the states that are responsible for the formation of the valence and conduction band edges. Figure 5.10 shows both the total atomic orbitals and the individual atomic shells that may be found at the band edges of the bulk brookite TiO_2. Conduction band (CB) was found to be dominated by the Ti 3d states with only a little amount of O 2p states, whereas the valence band (VB) was found to be dominated by the O 2p states with only a small amount of Ti 3d states. Figure 5.11 illustrates the contribution of the states for the pure 3x1 brookite TiO_2 (210) surface as well as brookite TiO_2/graphene hybrid system. The findings point to an exceedingly small contribution from the 2s

states in both the conduction and the valence bands. Both bands exhibit evidence of contribution from the 2p states. As a result of the contribution of the 2p states to the Fermi level, new energy levels have been produced in the band structure of brookite TiO_2/graphene hybrid system. These new energy levels may be seen as the source of the small band gap energy in the brookite TiO_2/graphene hybrid system.

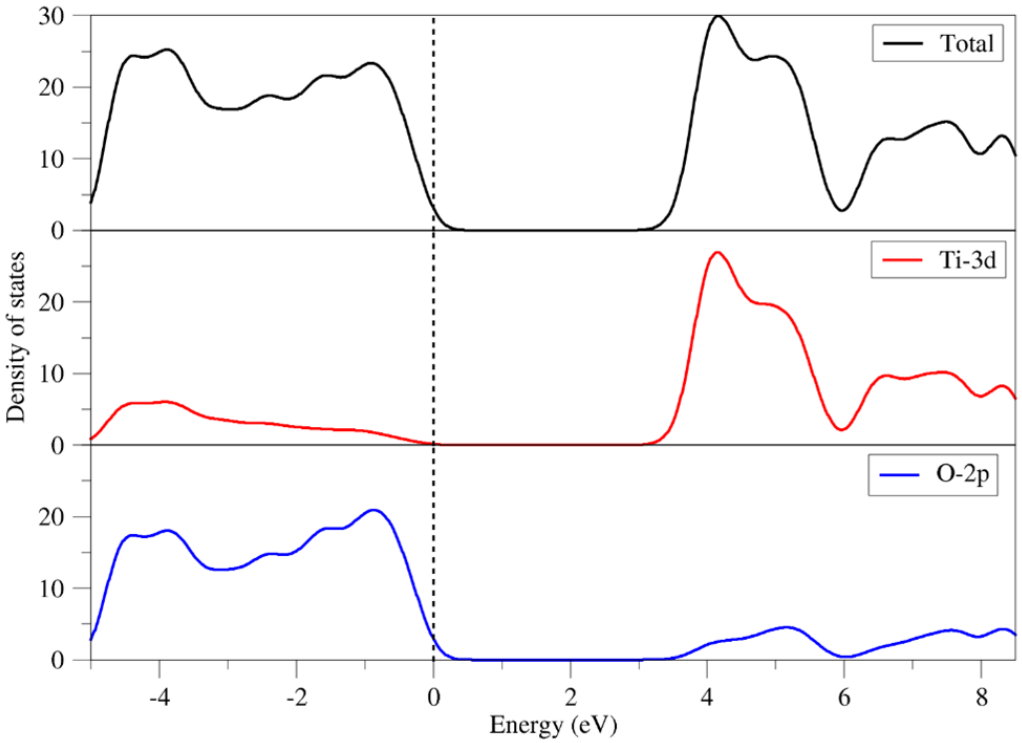

Figure 5.10: TDOS and PDOS of brookite TiO_2 bulk structure.

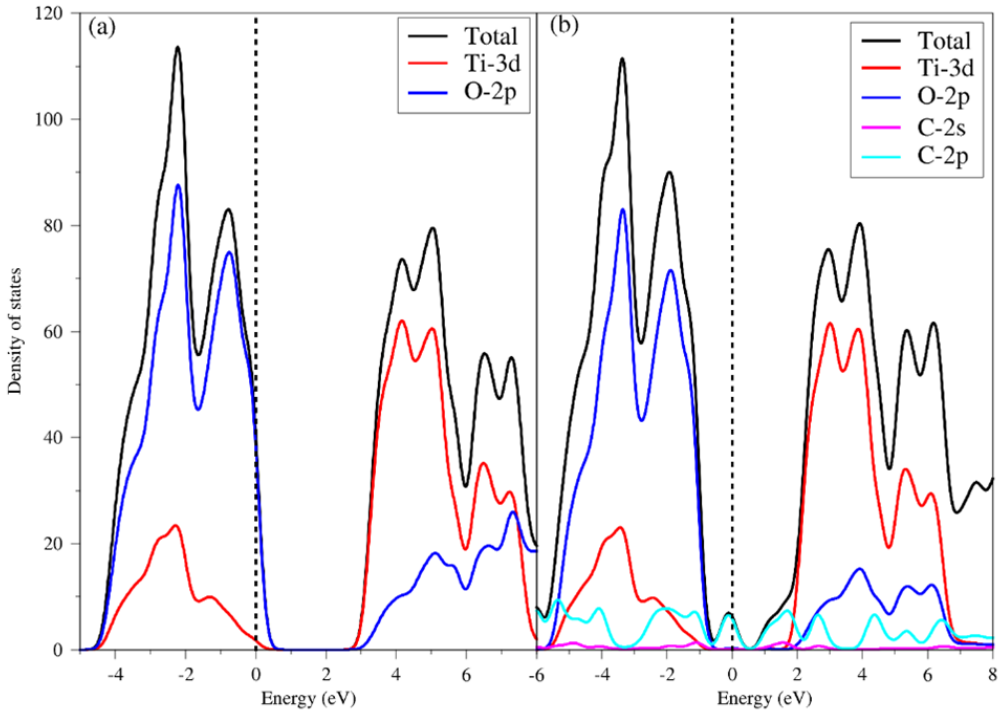

Figure 5.11: TDOS and PDOS of (a) 3×1 brookite TiO_2 (210) surface (b) brookite TiO_2/graphene hybrid system.

5.3.3 Optical properties

Calculations of the optical properties were done in order to investigate the possible use of brookite TiO_2/graphene hybrid composite in photocatalysis. Dielectric function, conductivity, refractive index, absorption, reflectivity, and loss function variables are all accounted for in material's optical properties calculations. The dielectric function is a complex quantity that is related with the band structure of a material. It is used to characterise the dielectric response of the a material, defined by a summation of a real $\varepsilon_1(\omega)$ and

imaginary $\varepsilon_2(\omega)$ parts as shown in Equation 5.1.

$$\varepsilon = \varepsilon_1(\omega) + \varepsilon_2(\omega) \tag{5.1}$$

The real and imaginary parts are correlated to the electronic polarizability and electronic absorption of the material, respectively. Calculated real and imaginary components of dielectric function of brookite TiO_2 (210) surface and its associated graphene hybrid are presented in Figure 5.12. Represented in Figure 5.12 (a) and (b) are the real and imaginary parts of dielectric function, respectively.

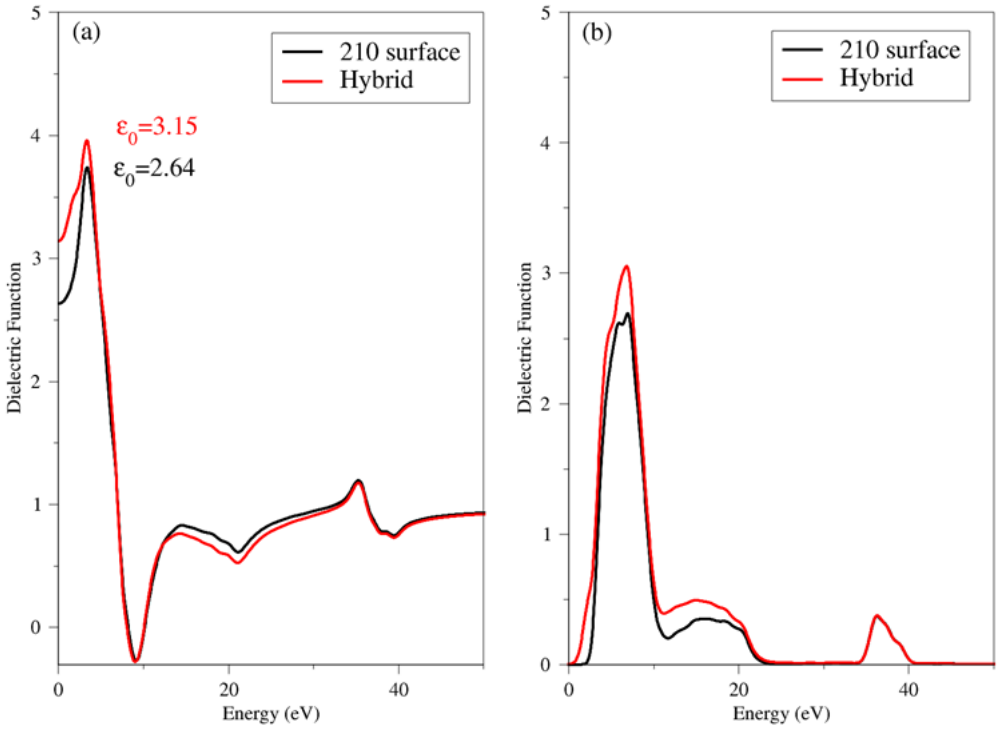

Figure 5.12: Calculated dielectric function of 3x1 brookite TiO_2 (210) surface (black curve) and brookite TiO_2/graphene hybrid system (red curve). (a) real part of dielectric function and (b) imaginary part of dielectric function.

Obtained results show dielectric constant of 2.64 for the brookite TiO_2 (210) surface and 3.15 for the corresponding brookite TiO_2/graphene hybrid

system. This shows that the hybrid system has high polarizability as compared to brookite TiO_2 (210) surface. For the imaginary part, the hybrid shows high intensity than brookite TiO_2 (210) surface supercell in two regions: 3.83 to 7.42 eV as well as 10.27 to 20.71 eV regions. It was observed that the dielectric curve has shifted from 1.97 to 0.31 eV. This is due to the new 2p states of C, as seen from the density of states result. It was also observed that for the imaginary part, the dielectric function is zero between 23 and 34 eV and region above 40 eV. From the dielectric function, Kramers-Kronig transformation is used to obtain the real $n(\omega)$ and imaginary parts $k(\omega)$ (extinction coefficient) of refractive index as [51]:

$$n(\omega) = \left(\frac{|\varepsilon(\omega)| + \varepsilon_1(\omega)}{2}\right)^{\frac{1}{2}} \tag{5.2}$$

$$k(\omega) = \left(\frac{|\varepsilon(\omega)| - \varepsilon_1(\omega)}{2}\right)^{\frac{1}{2}} \tag{5.3}$$

There is a correlation between the light absorption and the imaginary component of the refractive index.

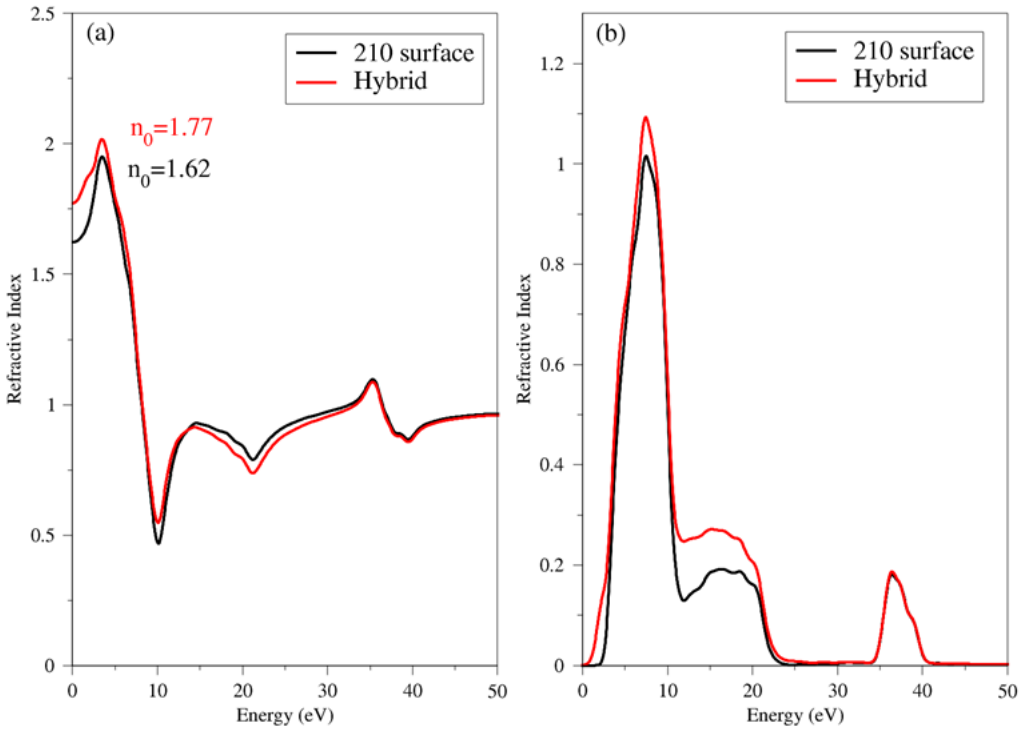

Figure 5.13: Calculated refractive index of 3x1 brookite TiO_2 (210) surface (black curve) and brookite TiO_2/graphene hybrid system (red curve). (a) real part of refractive index and (b) imaginary part of refractive index.

It can be seen in Figure 5.13 that the dielectric function and refractive index have a direct relation, with the complex refractive index of the medium N defined as:

$$N = \sqrt{\varepsilon} = n + ik \tag{5.4}$$

The absorption $\alpha(\omega)$, reflectivity $R(\omega)$ and loss function $L(\omega)$ can also be derived from the dielectric function:

$$\alpha(\omega) = \frac{2k\omega}{c} \tag{5.5}$$

The calculated results of the absorption are presented in Figure 5.14.

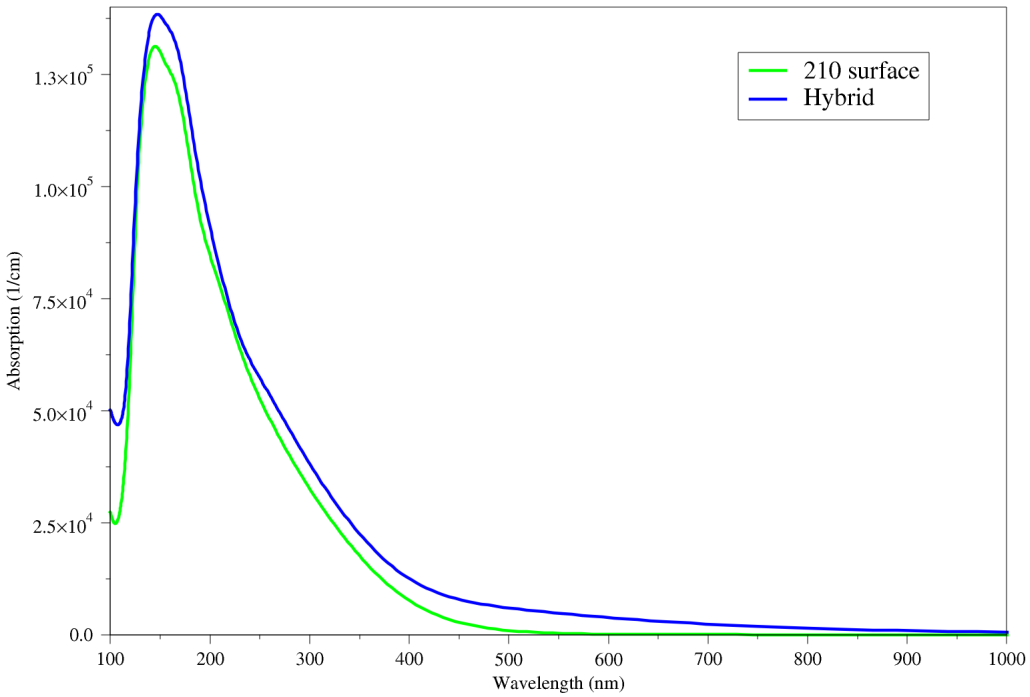

Figure 5.14: Calculated optical absorption behavior of 3x1 brookite TiO_2 (210) surface (green curve) and brookite TiO_2/graphene hybrid system (blue curve).

As expected, pure brookite TiO_2 bulk structure shows extremely high absorbance in the ultraviolet spectrum and less absorption in the visible region. For the associated graphene hybrid, the composite effectively increased the absorbance in the visible region. It can be observed that brookite TiO_2/graphene hybrid composite has higher absorbance than 3x1 brookite TiO_2 (210) surface in the wavelength region of 350 - 800 nm.

5.4 Conclusion

In summary, our first-principles DFT calculations to study the structural, electronic and optical properties of pure brookite TiO_2 bulk structure as well as brookite TiO_2/graphene hybrid composite, have revealed significant changes in the properties. The calculated structural properties of pure brookite TiO_2 bulk structure were found to be in good agreement with the experimental and theoretical results. While the DFT underestimated the band gap value of pure brookite TiO_2 bulk structure, the scissor operator was used to get the band gap of 3.4 eV. After the incoropating graphene on brookite TiO_2, the band structure shows that new energy levels were induced, allowing the band gap to reduce. The calculated optical properties shows that incoropating graphene on brookite TiO_2 increases the electronic polarizability of the structure. On the optical absorption, there was an increase in the range of the visible region, which agrees with the calculated electronic properties.

References

[1] S. Rehman, R. Ullah, A. M. Butt and N. D. Gohar, Strategies of making TiO_2 and ZnO visible light active, Journal of Hazardous Materials, 170, 560, 2009.

[2] N. Rawal, A. G. Vaishaly, H. Sharma and B. B. Mathew, Dye sensitized solar cells: the emerging technology, Energy and Power Engineering Science, 2, 46, 2015.

[3] C. Magne, S. Cassaignon, G. Lancel and T. Pauport, Brookite TiO_2 nanoparticle films for dye-sensitized solar cells, Physical Chemistry Chemical Physics, 12, 2461, 2011.

[4] A. Sasani, A. Baktash, K. Mirabbaszadeh and B. Khoshnevisan, Structural and electronic properties of Mg and Mg-Nb co-doped TiO_2 (101) anatase surface, Applied Surface Science, 384, 298, 2016.

[5] B. O'Regan and M. Grätzel, A low-cost, high efficiency solar cell based on dye-sensitized colloidal TiO_2 films, Nature, 353, 737, 1991.

[6] M. Grätzel, Recent advances ins sensitized mesoscopic solar cells, Accounts of Chemical Research, 42, 1788, 2009.

[7] Y. Chiba, A. Islam, Y. Watanabe, R. Komiya, N. Koide and L. Y. Han, Dye-sensitized solar cells with conversion efficiency of 11.1%, Japanese Journal of Applied Physics, 45, L638, 2006.

[8] A. Mattsson and L. Osterlund, Adsorption and photoinduced decomposition of acetone and acetic acid on anatase, brookite, and rutile TiO2 nanoparticles, Journal of Physical Chemistry C, 114, 14121, 2010.

[9] S. Muhammady, F. G. Setiawan, I. M. Sutjahja, T. Winata and Y. Darma, Studi Ab Initio dengan metode GGA dan GGA + U terpolarisasi spin untuk mengkaji sifat elektronik dan magnetik kristal TiO_2 pada fasa rutile, anatase, dan brookite, Jurnal Matematika and Sains, 19, 3, 2014.

[10] R. Asahi, T. Morikawa, T. Ohwaki, K. Aoki and Y. Taga, Visible-light photocatalysis in nitrogen-doped titanium oxides, Science, 293, 269, 2001.

[11] H. Tada, T. Kiyonaga and S. Naya, Rational design and applications of highly efficient reaction systems photocatalyzed by noble metal nanoparticle-loaded titanium (IV) dioxide, Chemical Society Reviews, 38, 1849, 2009.

[12] H. Irie, Y. Watanabe and K. Watanabe, Nitrogen-concentration dependence on photocatalytic activity of $TiO_{2-x}N_x$ powders, Journal of Physical Chemistry B, 107, 5483, 2003.

[13] S. U. M. Khan, M. Al-Shahry and W. B. Ingler, Efficient photochemical water splitting by a chemically modified n-TiO_2, Science, 297, 2243, 2002.

[14] T. L. Thompson and J. T. Yates, Surface science studies of the photoactivation of TiO_2 new photochemical processes, Chemical Reviews, 106, 4428, 2006.

[15] X. Qiu and C. Burda, Chemically synthesized nitrogen-doped metal oxide nanoparticles, Chemical Physics, 3391, 1, 2007.

[16] R. Jin, W. Gao, J. Chen, H. Zeng, F. Zhang, Z. Liu and N. Guan, Photocatalytic reduction of nitrate ion in drinking water by using metal-loaded $MgTiO_3$-TiO_2 composite semiconductor catalyst, Journal of Photochemistry and Photobiology A: Chemistry, 162, 585, 2004.

[17] A. B. C. Silva, V. C. Costa, J. D. Ardisson, F. Magalhaes, R. M. Lago and M. T. C. Sansiviero, Decomposition of the molecular precursor $Bu_4Sn_6S_6$ on the surface of TiO_2 to prepare semiconductor composite photocatalysts Materials Research Bulletin, 45, 174, 2010.

[18] S. Sarkar, A. Makhal, K. Lakshman, T. Bora, J. Dutta and S. K. Pal, Dual-sensitization via electron and energy harvesting in CdTe quantum dots decorated ZnO nanorod-based dye-sensitized solar cells, Journal Physical Chemistry C, 116, 14248, 2012.

[19] G. Vercelli, G. Zotti, A. Berlin, M. Pasini, C. Botta, R. Gerbasi, T. L. Nelson and R. D. McCullough, Oligo(poly)thiophene sensitization of CdSe nanocrystal and TiO_2 polycrystalline electrodes: A photoelectrochemical investigation, Physical Chemistry C, 116, 2033, 2012.

[20] B. Neppolian, Q. Wang, H. Jung and H. Choi, Ultrasonic-assisted sol-gel method of preparation of TiO_2 nano-particles: Characterization, properties and 4-chlorophenol removal application, Ultrasonics Sonochemistry, 15, 649, 2008.

[21] W. T. Sun, Y. Yu, H. Y. Pan, X. F. Gao, Q. Chen and L. M. Peng, CdS quantum dots sensitized TiO_2 nanotube-array photoelectrodes, Journal of the American Chemical Society, 130, 1124, 2008.

[22] J. Lu, F. Su, Z. Huang, C. Zhang, Y. Liu, X. Ma and J. Gong, N-doped Ag/TiO_2 hollow spheres for highly efficient photocatalysis under visible-light irradiation, RSC Advances, 3, 720, 2013.

[23] G. Kresse and J. Furthmuller, Efficiency of ab-initio total energy calculations for metals and semiconductors using a plane-wave basis set, Computational Materials Science, 6, 15, 1996.

[24] G. Kresse and J. Furthmuller, Efficient iterative schemes for ab initio total-energy calculations using a plane-wave basis set, Physical Review B, 54 11169, 1996.

[25] J. P. Perdew, K. Burke and M. Ernzerhof, Generalized gradient approximation made simple, Physical Review Letters, 77, 3865, 1996.

[26] W. K. Li, X. Q. Gong, G. Lu and A. Selloni, Different reactivities of TiO_2 polymorphs: comparative DFT calculations of water and formic acid

adsorption at anatase and brookite TiO_2 surfaces, Journal of Physical Chemistry C, 112, 6594, 2008.

[27] E. P. Meagher and G. A. Lager, Polyhedral thermal expansion in the TiO_2 polymorphs; refinement of the crystal structures of rutile and brookite at high temperature, Canadian Mineralogist, 17, 77, 1979.

[28] A. Beltran, L. Gracia and J. Andres, Density functional theory study of the brookite surfaces and phase transitions between natural titania polymorphs, Journal of Physical Chemistry B, 110 23417, 2006.

[29] M. H. Samat, M. F. M. Taib, O. H. Hassan, M. Z. A. Yahya and A. M. M. Ali, Structural, electronic and optical properties of brookite phase titanium dioxide, Materials Research Express, 4, 044003, 2017.

[30] N. E. Malute, R. S. Dima, H. Nemudzivhadi, R. R. Maphanga and Sankaran, Computational study of dye adsorption onto Brookite TiO_2 surfaces for the applications in dye sensitized solar cells, Journal of Physics: Conference Series, 905, 012034, 2017.

Chapter 6

Conclusion

Using density functional theory as embodied in the CASTEP's Material Studio software, a number of electrical and optical properties of graphene, brookite TiO_2 and brookite TiO_2/graphene hybrid composite were successfully explored. Different models of graphene were generated in order to find the optimum graphene supercell. The results of our research indicate that the electronic structure of different graphene supercells is the same. The band structure computations showed that the Fermi level in all graphene supercells is located at the Dirac point, which indicates that there is no band gap energy. This agrees with previous studies that stated that a pristine graphene has a zero-band gap energy. According to the results of the density of states experiment, the s and p orbitals predominated in the valence band as well as the conduction band. According to the findings of the absorption, certain graphene supercells have minimal activity in the visible region, but other graphene structures have high absorbance in the visible area reaching all the way to the infrared sector of the spectrum. The findings suggest that graphene has a high dielectric constant, which qualifies it as an excellent candidate for application in various electronic devices. The optical properties results show that the optimum graphene supercell is the 4×4 configuration. To explore the use of graphene in many applications, the 4×4 graphene supercell was doped, and the electronic and optical properties of the doped structure were calculated. When graphene is mono-doped with either titanium or ruthenium or co-doped with both, band gap is generated. These

results demonstrate a change from semi-metallic to semi-conducting behavior. This paves the way for the exploration of novel applications for graphene as a semiconductor.

The electronic and optical properties of brookite TiO_2 structure and brookite TiO_2 (210) surface/graphene hybrid composite were also successfully investigated using density functional theory. The band structure of brookite TiO_2 bulk structure shows a direct band gap, as expected. The brookite TiO_2 (210) surface/graphene hybrid results suggest formation of energy levels in the conduction band of the hybrid structure, resulting in narrowing the band gap. With the creation of extra energy levels, electrons move from the VB to CB with less probability of charge recombination. Brookite TiO_2 (210) surface/graphene hybrid exhibit good visible light absorption due to the narrowed band gap caused by the carbon 2p states below the conduction band minimum. When the surface of brookite TiO_2 (210) is interfaced with a graphene sheet, absorption calculations show a red shift in the visible region. These calculations could provide a basis for challenging synthesis and exploration of undiscovered properties of the composite of titanium dioxide with graphene and extend the knowledge for developing better photocatalysts for application in DSSCs.